Title
Acid Strength and Solvation in Catalysis by Solid Acids

Author
Jones, Andrew J.

Publication Date
2014

Peer reviewed|Thesis/dissertation

Acid Strength and Solvation in Catalysis by Solid Acids

By

Andrew James Jones

A dissertation submitted in partial satisfaction of the

requirements for the degree of

Doctor of Philosophy

in

Chemical and Biomolecular Engineering

in the

Graduate Division

of the

University of California, Berkeley

Committee in charge:

Professor Enrique Iglesia, Chair
Professor Alexander Katz
Professor Robert G. Bergman

Fall 2014

Acid Strength and Solvation in Catalysis by Solid Acids

by

Andrew James Jones

Abstract

Acid Strength and Solvation in Catalysis by Solid Acids

by

Andrew James Jones

Doctor of Philosophy in Chemical and Biomolecular Engineering

University of California, Berkeley

Professor Enrique Iglesia, Chair

The influence of composition and structure on the reactivity of solid Brønsted acids is not well understood, in part, because of difficulties in separating contributions of acid strength and solvation by van der Waals interactions to the stability of transition states and reactive intermediates. This study examines the diversity of acid strength and solvation across solid acids and their consequences for the rates of methanol dehydration turnovers to form dimethyl ether (DME). The results form a framework based on fundamental principles for understanding the catalytically relevant differences of solid acids and their impact on the rate and selectivity of Brønsted acid catalyzed turnovers. A methodology is presented and assessed for the prediction of reactivity from the estimation of van der Waals interactions of transition states at all acid site locations in zeolites.

The acid strength of a Brønsted acid is defined as the deprotonation energy (DPE) required to heterolytically cleave the O-H bond. DPE values are not accessible to experiment on solids, but can be calculated from DFT. Methanol dehydration rate constants, which reflect the free energy differences between bimolecular DME formation transition states and either methanol monomers (first-order) or dimers (zero-order), decreased exponentially with increasing DFT-derived DPE values (decreasing acid strength) of MFI zeolites with different heteroatoms (Al, Ga, Fe and B). These results demonstrate that weaker acids decrease the reactivity of zeolites because more free energy is required to break the Brønsted O-H bond and form the necessary ion-pair transition state. The free energy differences between transition states and reactive intermediates are proportional to DPE values on zeolites *and* polyoxometalate clusters, indicating the ubiquitous influence of acid strength regardless of acid composition or structure.

The unique reactivity of zeolites compared with other solid acids is often attributed, non-rigorously and inappropriately, to differences in the acid strength of different structures. Methanol dehydration rate constants, however, are similar on MFI zeolites with different densities of Al heteroatoms and increase monotonically with van der Waals interaction energies of transition state surrogates on zeolites with a wide range of void sizes (FAU, SFH, BEA, MOR, MFI, MTT). Combined with the large influence of DPE on rate constants, these results indicate that the acid strength differences of aluminosilicates are negligible for catalysis and that the remarkable catalytic diversity of aluminosilicates instead reflects differences in the size and

shape of voids that confine and stabilize transition states and reactive intermediates through van der Waals interactions.

The misconceptions surrounding the acid strength of zeolites are due, in part, to differences in DFT-derived DPE values in different zeolite frameworks or acid site locations. In particular, DPE values calculated (Periodic-DFT; RPBE/PAW) on zeolites (MFI, BEA, MOR, CHA, FAU, FER) for protons at all crystallographically unique O-sites differ markedly (up to 47 kJ mol^{-1}) depending on the location of protons and Al-atoms in their structures. DPE values appropriately averaged over all O-atoms at an Al location, however, are similar (within 13 kJ mol^{-1}) and reflect the negligible differences in acid strength for catalysis. These calculations demonstrate the pitfalls of DFT-derived DPE values and clarify their relationship to catalysis at temperatures above 0 K.

Deprotonation energies, appropriately averaged above 0 K, and van der Waals interaction surrogates, provide a general framework for understanding the reactivity differences of solid acids. van der Waals interaction energies of transition state surrogates at all crystallographically unique proton binding sites calculated from force-fields correlate with methanol dehydration rate constants on zeolites (FAU, SFH, BEA, MOR, MFI, MTT) and demonstrate that these calculations provide a useful method to narrow the selection of zeolites with enhanced reactivity or selectivity. Ray histograms, presented here for the first time, provide a representation of the shape and size of zeolite voids as a distribution of ray lengths and allow for the rapid comparison and selection of zeolites with voids of a certain shape/size. These findings open new opportunities for the rational design and selection of zeolites with enhanced reactivity and selectivity.

TABLE OF CONTENTS

ACKNOWLEDGEMENTS

First and foremost, I thank Professor Enrique Iglesia for his guidance, wisdom, and patience. His genuine curiosity for all things scientific and his fundamental molecular perspective have positively shaped my experience and methodology for conducting scientific research. I am particularly grateful for his flexibility, which has allowed me to involve myself in a multitude of research projects.

I also acknowledge Dr. Stacey Zones, who has been an instrumental resource and mentor throughout my time at UC Berkeley. The many discussions we have had helped to shape my research and continue to help guide my decisions. Next, I thank Raj Gounder for teaching me everything I now take for granted about zeolites. Raj was, and continues to be, a truly outstanding scientist, mentor and friend.

Next, I would like to acknowledge Rob Carr, David Hibbitts, Will Knaeble, Michele Sarazen and Prof. Matthew Neurock for many useful and stimulating discussions that have helped organize my thoughts and in the completion of this work. Specific acknowledgments for technical and intellectual contributions are given at the end of each chapter, where appropriate.

The constituents of the Laboratory for the Science and Applications of Catalysis (LSAC), both past and present (and their significant others) are also gratefully acknowledged. These include, but are not limited to: Brett and Alexandra Loveless, Gina Noh, Will and Steph Knaeble, Brian Weiss, Dante Simonetti, Dave Flaherty, Sebastian Kunz, Stan Herrmann, Allie Landry. Team ‘Zeolites’ and team ‘POM’ are also acknowledged – I hope the legacy continues. I am so thankful to have been surrounded by such wonderful, intelligent and ambitious people. Hutomo Prayogo, an undergraduate researcher, Maciek Haranczyk (LBNL) and Christopher Ostrouchov are also acknowledged for their help with this research.

I also acknowledge, with thanks, the financial support of Chevron Energy Technology Company and the National Science Foundation for a graduate research fellowship.

Finally, I thank all my friends and family for their continued support and encouragement. Kristen Jones, my wife and better half, thank you for your support, sacrifices, patience and understanding through it all; I would not be here without you.

CHAPTER ONE

Introduction to Acid Strength and Solvation in Solid Acids

Solid acids are the most used industrial heterogeneous catalysts, in part, because their wide variety of structures and compositions give way to a unique range of reactivities and selectivities [1, 2]. Zeolites, in particular, are crystalline silicates with ordered pores of molecular dimensions (0.4-1.3 nm) that are used frequently in adsorption and catalysis where they replace corrosive and environmentally-harmful liquid acids [3]. The thermal stability, acid strength and the ability to control acid site density and void size/shape have contributed to the success of almost 20 zeolite frameworks in industry involving isomerization, cracking, alkylation, dehydration and carbonylation reactions. The future success of zeolites for catalysis depends on our ability to select and synthesize structures from the large number of unique zeolite frameworks (>200 [4]) and, eventually, from databases of frameworks that have not yet been synthesized but are thermodynamically feasible (>500,000 [5]). This directed synthesis approach will require robust structure-function relations that allow for the selection of zeolites with enhanced reactivity and selectivity from fundamental principles.

The ingress and egress of molecules through zeolite pores has dominated the discourse surrounding the unique reactivity of zeolites over the last few decades because void size constraints control the access of reactant molecules to active sites within voids and the diffusion of the resulting products [6, 7]. The largest included and free sphere diameters [8] and other zeolite size representations [9, 10] have vastly improved the ability to predict the accessibility of molecules in zeolite pores. The synthesis of hierarchical zeolites that contain mesopores in addition to micropores have been proposed and pursued by many to increase the accessibility of molecules to active sites within zeolite pores [2, 11]. Yet, these size exclusion metrics focus inherently on mass transfer limitations and not on intrinsic reactivity differences of the zeolite. Research that focuses on elucidating the factors that control the reactivity of zeolite structures have been limited because of the difficulties involved with the separation of mass transfer contributions from rates, the extrication of acid strength contributions to reactivity from other non-local interactions, and the limited knowledge about the location of acid sites in zeolites pores.

The reactivity of Brønsted acids depend on the strength of their acid sites, defined rigorously as the deprotonation energy (DPE), or the energy required to heterolytically cleave the O-H bond and remove the proton to non-interacting distances, because stronger acids (smaller DPE) require less energy to separate charge and form ion-pair transition states [12-14]. DPE values are not directly accessible from experiment, but they can be calculated with density functional theory (DFT) [15, 16]. Acidity functions of liquid acids (e.g. Hammett scales) fail in the context of solid acids because of the absence of a liquid solvation sphere and the inhomogeneity of dispersive stabilizations of basic probes from different void sizes and shapes in solids [17, 18]. In particular, NH_3 adsorption enthalpies measured calorimetrically are similar on Al-MFI and Fe-MFI structures (-145 ± 5 kJ mol^{-1}), but these structures differ markedly in their n-hexane cracking turnover rates ($1.3 \cdot 10^{-3}$ vs. $0.048 \cdot 10^{-3}$ n-$C_6H_{14} \cdot (H^+ \cdot s)^{-1}$, 700 K) [19]; yet, NH_3 adsorption enthalpies depend strongly on the sample, Al-density and measurement method on Al-MFI samples (-104 to -150 kJ mol^{-1})[15]. The van der Waals interactions that stabilize basic probes

also stabilize alkane cracking transition states confined within pores of molecular dimensions [18, 20-23], but it is not clear to what extent acid strength and solvation by van der Waals interactions contribute to reactivity, in general. Here, kinetic, spectroscopic and theoretical tools are used to assess the acid strength differences in zeolites and the consequences of acid strength and confinement on reactivity.

The individual effects of acid strength and confinement on reactivity are accessible to a mechanistic interpretation of rate constants and their values. Methanol dehydrates over Brønsted acid sites of varying acid strength to form dimethyl ether and water [12]. The small molecules involved easily diffuse into zeolite pores, thus minimizing mass transfer limitations to rates, and the low temperatures (433 K) of these reactions minimize entropy contributions to measured free energies and rate constants [23]. In Chapter 2, methanol dehydration reactions in MFI are assessed to determine the prevalent mechanism of dehydration and the thermodynamic meaning of rate constants. Low temperatures favor larger bimolecular dehydration transition states over smaller monomolecular ones, because enthalpic gains of adsorption have larger contributions to free energies than entropy losses at these temperatures. Higher temperatures, on the other hand, give way to methoxy-mediated routes that are important in the synthesis of hydrocarbons and fuels from methanol.

The two apparent rate constants for the dehydration of methanol to dimethyl ether at 433 K reflect the energy of the bimolecular dehydration transition state relative to two reactive intermediates. In Chapter 3, these rate constants are measured on MFI zeolites with different heteroatoms (Al, Ga, Fe, B) and heteroatom density to determine the influence of composition on acid strength. The rate constants decrease exponentially with DFT-derived DPE values on MFI zeolites with different heteroatoms and W-based Keggin polyoxometalates with different central atoms. Al-atom density, however, does not influence rate constant values, indicating acid strength is independent of the location of Al within the framework. At high Al-densities, the preferential increase in only one rate constant reveals that protons begin to distribute in more confining voids, presumably the channels and not their intersections in MFI. The negligible differences in acid strength with Al-density are compared with DFT-derived DPE values in Chapter 4. Periodic DFT calculations indicate that DPE values are different depending on the specific Al-O(H)-Si locations within the MFI framework, but the average of these DPE values at a given Al location are similar to those averages at other Al locations. This temperature dependence of acid strength fundamentally describes the observed reactivity of zeolites and rectifies contradictions between experiment and theory in zeolites.

The influence of the local environment on the stabilization of transition states and reactive intermediates depends on van der Waals and H-bonding interactions. Methanol dehydration rate constants measured on a range of zeolites (FAU, SFH, BEA, MOR, MFI, MTT) are presented in Chapter 5 to assess the influence of structural changes on reactivity. The exponential increase of rate constants with smaller voids are correlated with surrogates for the dispersion of dimethyl ether transition states, which include n-hexane adsorption enthalpies and van der Waals interactions of dimethyl ether from DFT and Lennard-Jones potentials. The dominant role of van der Waals interactions in controlling the stability of transition states presented here indicates that the catalytic diversity of zeolites is the result of subtle changes in the shape and size of zeolite

pores and the locations of protons within them, and not on changes in acid strength as eluded to previously in many studies.

These results show that van der Waals interactions are predominantly responsible for the extraordinary catalytic diversity of zeolites. The reactivity of zeolites can, therefore, be predicted from approximations to these interactions using quantum mechanics, force-fields or simple size metrics because these interactions depend sensitively on the shapes and sizes of voids and molecules within them. Spherical and cylindrical representations of void spaces neglect the intricacies of pore networks because the van der Waals radii of atoms in zeolites create undulations that are not captured by smooth shapes. The distribution of rays in a pore network presented in Chapter 6, however, provides a concise representation of the shape, size and distribution of pores. Ray histograms provide a fingerprint for a zeolite pore network and allow for the selection of zeolites with similar pore features from large databases of structures. These histograms are extended in Chapter 6 to study the diversity of pore structures from hypothetical zeolite databases. Novel zeolite structures are proposed to replace zeolites in practice and potentially enhance their reactivity and selectivity for industrially relevant reactions.

References

[1] A. Corma, Chem. Rev. 95 (1995) 559-614.
[2] J. Čejka, G. Centi, J. Perez-Pariente, and W.J. Roth, Catal. Today 179 (2012) 2-15.
[3] A. Corma, Current Opinion in Solid State & Materials Science 2 (1997) 63-75.
[4] C. Baerlocher, and L.B. McCusker. Database of Zeolite Structures.
[5] E. Haldoupis, S. Nair, and D.S. Sholl, PCCP 13 (2011) 5053-5060.
[6] T.F. Degnan, J. Catal. 216 (2003) 32-46.
[7] W.O. Haag, R.M. Lago, and P.B. Weisz, Faraday Discuss. 72 (1981) 317-330.
[8] M.D. Foster, I. Rivin, M.M.J. Treacy, and O.D. Friedrichs, Micropor. Mesopor. Mater. 90 (2006) 32-38.
[9] E.L. First, C.E. Gounaris, J. Wei, and C.A. Floudas, PCCP 13 (2011) 17339-17358.
[10] A.J. Jones, C. Ostrouchov, M. Haranczyk, and E. Iglesia, Micropor. Mesopor. Mater. 181 (2013) 208-216.
[11] J. Čejka, A. Corma, and S. Zones, Zeolites and Catalysis: Synthesis, Reactions and Applications. John Wiley & Sons, 2010.
[12] R.T. Carr, M. Neurock, and E. Iglesia, J. Catal. 278 (2011) 78-93.
[13] M.J. Janik, J. Macht, E. Iglesia, and M. Neurock, The Journal of Physical Chemistry C 113 (2009) 1872-1885.
[14] J. Macht, R.T. Carr, and E. Iglesia, J. Catal. 264 (2009) 54-66.
[15] M. Brandle, and J. Sauer, J. Am. Chem. Soc. 120 (1998) 1556-1570.
[16] U. Eichler, M. Brandle, and J. Sauer, J. Phys. Chem. B 101 (1997) 10035-10050.
[17] R.J. Gorte, Catal. Lett. 62 (1999) 1-13.
[18] R. Gounder, and E. Iglesia, Chem. Commun. 49 (2013) 3491-3509.
[19] D.J. Parrillo, C. Lee, R.J. Gorte, D. White, and W.E. Farneth, The Journal of Physical Chemistry 99 (1995) 8745-8749.
[20] E.G. Derouane, J. Catal. 100 (1986) 541-544.
[21] R. Gounder, and E. Iglesia, J. Am. Chem. Soc. 131 (2009) 1958-1971.
[22] R. Gounder, and E. Iglesia, Angew. Chem. Int. Ed. 49 (2010) 808-811.
[23] R. Gounder, and E. Iglesia, Acc. Chem. Res. 45 (2012) 229-238.

CHAPTER TWO

Kinetic, Spectroscopic and Theoretical Assessment of Associative and Dissociative Methanol Dehydration Routes in Zeolites

Rates of chemical reactions depend on free energy differences between transition states and their precursors. The functional form of Gibbs free energies favors enthalpic over entropic stabilization of transition states at modest temperatures.[1] These enthalpy-entropy trade-offs are evident, as shown here, in causing methanol dehydration to dimethyl ether (DME) to proceed via direct (associative) instead of sequential (dissociative) routes at the low temperatures of its customary practice. Higher temperatures, relevant to the synthesis of hydrocarbons from methanol,[2] favor dissociative routes mediated by transition states with higher entropies but also higher enthalpies than for direct routes.

Two plausible catalytic CH_3OH dehydration sequences diverge after the quasi-equilibrated formation of H-bonded CH_3OH monomers at acidic OH ((II), Scheme 1).[3-6] In associative routes, monomers react with CH_3OH(g) to form protonated CH_3OH dimers (Step D2, Scheme 1), which rotate to form the transition state (TS) for kinetically-relevant DME formation steps (D4). In dissociative routes, CH_3OH dehydrates instead to form methoxides in the kinetically-relevant step (S2, Scheme 1); methoxides then react with a CH_3OH(g) to form DME. The assumptions of pseudo-steady-state for adsorbed species and quasi-equilibrated monomers and dimers as the most abundant adsorbed intermediates (infrared evidence presented later) give rate equations for associative routes,

$$\frac{r_{DME,D}}{\left[H^+\right]} = \frac{k_{D4}K_{D3}K_{D2}K_M\left[CH_3OH\right]^2}{K_M\left[CH_3OH\right]+K_{D2}K_M\left[CH_3OH\right]^2} = \frac{k_{D4}K_{D3}K_{D2}\left[CH_3OH\right]}{1+K_{D2}\left[CH_3OH\right]}\ , \tag{1}$$

and for their dissociate counterparts,

$$\frac{r_{DME,S}}{\left[H^+\right]} = \frac{k_{S2}K_M\left[CH_3OH\right]}{K_M\left[CH_3OH\right]+K_{D2}K_M\left[CH_3OH\right]^2} = \frac{k_{S2}}{1+K_{D2}\left[CH_3OH\right]}\ , \tag{2}$$

with rate and equilibrium parameters defined in Scheme 1 (details in SI). Kinetically-relevant steps are confirmed by density functional theory (DFT) below and elsewhere.[3-5] TS theory formalisms give the ratio of these two rates (pressure units are those for free energy standard states for gaseous species):

$$\frac{r_{DME,D}}{r_{DME,S}} = \exp\left(\frac{-\left(\Delta G_D^{\ddagger}-\Delta G_S^{\ddagger}\right)}{k_BT}\right)\frac{\left[CH_3OH\right]}{1\ bar} = \chi\ . \tag{3}$$

These free energies represent those for the transition states involved in dissociative (direct, $\Delta G_D^{\ddagger}$) and associative (sequential, $\Delta G_S^{\ddagger}$) routes relative to gaseous reactants and the free Brønsted acid. Equation (3) accounts for the relative contributions of associative and dissociative routes at each

temperature and CH_3OH pressure. These Gibbs free energies can be expressed in terms of the enthalpies and entropies of transition states relative to gaseous reactants and an unperturbed proton:

$$\Delta G_D^{\ddagger} - \Delta G_S^{\ddagger} = \left(\Delta H_D^{\ddagger} - \Delta H_S^{\ddagger}\right) - T\left(\Delta S_D^{\ddagger} - \Delta S_S^{\ddagger}\right). \quad (4)$$

DFT and statistical mechanics treatments have shown that associative (direct) dehydration routes prevail on W-based polyoxometalates (POM) at 400-500 K and 0.01-1 kPa CH_3OH pressures.[3] Turnover rates on H-MFI increased linearly with CH_3OH pressure at low CH_3OH pressures,[7] consistent with Eq. (1) (but not with Eq. (2)) when H-bonded CH_3OH monomers are the predominant surface species, as shown by the prevalence of their infrared bands on H-MFI at sub-stoichiometric coverages (<1 CH_3OH per H^+)[8]; such infrared spectra were measured at (ambient) temperatures where dehydration is not detectable. Removing gaseous CH_3OH or DME leads to the detection of methoxides by their infrared[9, 10] and ^{13}C MAS NMR[11] spectra; they can react with CH_3OH to form DME at 433-473 K.[12, 13] These stoichiometric cycles are analogous to dissociative routes, but are limited to one turnover. An assessment of the contributions from dissociative and associative routes requires rate equations and infrared spectra at conditions of dehydration catalysis and theoretical treatments that rigorously account for the van der Waals interactions that stabilize transition states and intermediates within zeolite voids.

Here, CH_3OH dehydration turnover rates and infrared spectra are measured at relevant temperatures and CH_3OH pressures to assess the contributions of these two routes to DME formation rates. Functionals that describe van der Waals interactions[14] and period DFT methods are used here to assign infrared bands and to extend this assessment to temperatures inaccessible to experiments because of ubiquitous side reactions.

The detection of O-H infrared bands in zeolites and their perturbation or attenuation by H-bonded or protonated species, respectively, are rendered feasible by their sharp and isolated character (e.g. 3604 cm^{-1} in H-MFI; Figure 1). Their frequencies are those expected for ν(OH) stretches in Brønsted acids (3621 cm^{-1} from DFT; Al12-O20(H)-Si3 in H-MFI henceforth). Contact with CH_3OH at catalytic conditions (0.2 kPa; 433 K) led to a broad band at 2371 cm^{-1} (Figure 1), corresponding to O-H groups perturbed by strong H-bonds with CH_3OH (2383 cm^{-1}; DFT). A band at 3581 cm^{-1}, absent from H-MFI or CH_3OH(g) spectra (Figure 1), appears during CH_3OH reactions and corresponds to ν(OH) modes in CH_3OH species interacting with framework O-atoms (3552 cm^{-1}; DFT). The 2620 cm^{-1} band appears at CH_3OH pressures >0.5 kPa and becomes stronger with increasing pressure (Figure 2), consistent with higher coverages of protonated CH_3OH dimers (ν(OH) of dimers is 2608 cm^{-1} from DFT). Methyl deformation modes of methoxides (1458 cm^{-1}; DFT) were not detected (0.2-16 kPa CH_3OH, 433 K) during steady-state catalysis, but emerge upon removal of CH_3OH(g) by evacuation at higher temperatures (1457 cm^{-1}; MFI; 523 K).[10] Methoxides are not present during catalysis at 433 K and 0.2-16 kPa CH_3OH, because H-bonded monomers are scavenged by CH_3OH(g) to form dimers before they can dissociate to methoxides. Methoxides can form, however, when CH_3OH(g) is removed and dimers can no longer form; H-bonded CH_3OH then either desorbs or forms stranded methoxides and H_2O(g). These spectra show that H-bonded monomers and protonated dimers (but neither unperturbed OH groups nor methoxides) are the predominant

species present at low (0.2-0.5 kPa) and high (7.7 -16 kPa) CH_3OH pressures, respectively, and 433 K.

Dehydration turnover rates (per H^+, from pyridine titration[7]) increased linearly with pressure at low pressures and then more gradually (Figure 3), as also observed on polyoxometalates and on MFI with Al, Ga, Fe, or B framework heteroatoms.[3, 7, 15] Zero-order rate constants are similar on MFI samples with 0.05-10 μm crystals and 0.7-3.6 H^+ per unit cell (0.012-0.019 DME $(H^+ \cdot s)^{-1}$, 433 K);[7] thus, diffusional constraints did not influence measured rates, which reflect the intrinsic reactivity of Brønsted acid sites within MFI.[7] These pressure effects on turnover rates reflect the prevalence of monomers at low pressures and of dimers at higher pressures; they cannot be described by dissociative (sequential) routes, because these would lead to zero-order or negative-order reactions when monomers or dimers are predominant species, respectively (Eq. (2)). The concurrent increase in turnover rates and the intensity of the infrared band for dimers (normalized area of 2620 cm^{-1} band; Figure 3) is consistent with direct routes, because the rates of direct, but not sequential, routes are proportional to the number of such dimers (Scheme 1).

These results, taken together, demonstrate that associative routes (Scheme 1, left; Eq. (1)) prevail on MFI at typical conditions of dehydration catalysis and, by inference, in light of their similar kinetic behavior, on other zeolites (FAU, SFH, BEA, MTW, MOR, MFI, MTT).[15] Direct routes also prevail on the stronger acid sites of polyoxometalates (1080-1143 kJ mol^{-1} [3] vs. 1171-1205 kJ mol^{-1} on crystalline aluminosilicates[7, 16]), because changes in acid strength influence the two free energy terms in Eq. (3) to similar extents.[3]

Activation entropies and enthalpies measured from temperature effects on dehydration rate constants are shown in Table 1 (Arrhenius plots in SI). Enthalpy barriers for k_{first} ($k_{D4}K_{D3}K_{D2}$; $\Delta H^{\ddagger}_{first}$ = 42 ± 2 kJ mol^{-1}) are smaller than for k_{zero} ($k_{D4}K_{D3}$; $\Delta H^{\ddagger}_{zero}$ = 90 ± 2 kJ mol^{-1}), as expected from two effective barriers that reflect the enthalpy of the same TS but referenced to CH_3OH and CH_3OH(g) (for $\Delta H^{\ddagger}_{first}$) and to a more stable dimer (for $\Delta H^{\ddagger}_{zero}$). Activation entropies, in turn, are more negative for k_{first} ($\Delta S^{\ddagger}_{first}$ = -160 ± 10 J $(K \cdot mol)^{-1}$) than for k_{zero} ($\Delta S^{\ddagger}_{zero}$ = -75 ± 2 J $(K \cdot mol)^{-1}$) because the reference state for k_{first} has higher entropy. The corresponding enthalpies and entropies of activation for sequential routes cannot be measured accurately, because such routes become favored only at higher temperatures, which lead to diffusional corruptions, side reactions, rapid deactivation and near-equilibrium CH_3OH conversions.

TS enthalpies and entropies can be estimated using periodic DFT methods with vdW-DF2 functionals[14] that include distinct terms (separable from local interactions) to account for van der Waals forces and H-bonds. Reaction coordinate diagrams for direct and sequential routes are shown in Figure 4. TS enthalpies for methoxide formation (TS2; relative to monomers) are 83 kJ mol^{-1} larger than for bimolecular dehydration (TS1; relative to monomers and CH_3OH(g); Figure 4a), reflecting the more effective enthalpic stabilization of TS1 over TS2 within zeolite voids. The van der Waals stabilization part of TS enthalpies is more negative (by 48 kJ mol^{-1}) for TS1 than for TS2 (relative to the same reference state), indicating that dispersive interactions preferentially stabilize the larger transition states in associative (TS1) routes.

Measured enthalpies of formation of DME formation transition states from dimers ($\Delta H^{\ddagger}_{zero}$) are similar to those derived from DFT (90 and 84 kJ mol^{-1}, respectively; Table 1), while those for that TS, but referenced to monomers and CH_3OH(g) ($\Delta H^{\ddagger}_{first}$) are 30 kJ mol^{-1} larger than DFT estimates. The difference between $\Delta H^{\ddagger}_{first}$ and $\Delta H^{\ddagger}_{zero}$ reflects the enthalpy of dimer formation by reaction of CH_3OH(g) with monomers and measured values (-48 kJ mol^{-1}) are less negative than those derived from DFT (-74 kJ mol^{-1}), apparently because the functional used overestimates van der Waals interactions.[17]

Entropies of transition states and relevant intermediates were calculated from DFT-derived frequencies using the harmonic approximation, which underestimates entropies for loosely-bound species,[18, 19] but is accurate for strongly-bound species, such as the TS, monomers and dimers involved in CH_3OH dehydration.[5] Measured TS1 entropies ($\Delta S^{\ddagger}_{first}$; -150 J (K·mol)$^{-1}$, Table 1) are similar to DFT-derived values (-158 J (K·mol)$^{-1}$, Table 1), but $\Delta S^{\ddagger}_{zero}$ estimates (14 J (K·mol)$^{-1}$) are much less negative than measured values (-75 J (K·mol)$^{-1}$) because the full translational and rotational freedom of protonated dimers is not captured by the harmonic potential. Experimental rate constants and barriers avoid the inaccuracies of DFT, however, DFT comparisons of direct and sequential routes are informative about the qualitative contributions of enthalpy and entropy to free energies.

The difference in TS free energies between direct and sequential routes in Eq. (3) derived from DFT (vdW-DF2/PAW) enthalpies and entropies is -20 kJ mol^{-1} at 433 K (Figure 4b), which leads to direct-to-sequential rate ratios (χ, Eq. (3)) that increase from 0.5 to 40 at 433 K as pressure increases from 0.2 to 16 kPa and to detectable contributions from dissociative routes only at the lowest pressures, which are much lower than used in dehydration catalysis practice. These χ values, taken together with the lack of detectable contributions from dissociative routes inferred from rate and infrared data (even at 0.2 kPa), suggest that DFT methods may actually overestimate dissociative contributions. The DFT-derived (RPBE/PAW) TS free energy differences responsible for χ values (Eq. (3)) on TON zeolites at 433 K are 20 kJ mol^{-1},[3c] which lead to χ values of 0.0006 at 16 kPa; these calculations neglect dispersion forces, which account for 48 kJ mol^{-1} of the energy difference between TS1 and TS2 in MFI, and, when added, χ estimates from DFT become similar for TON and MFI.

DFT-derived CH_3OH dehydration rate constants for associative and dissociative routes are shown in Figure 5 as a function of temperature. Associative routes are preferred (χ>1) below 503 K at 0.1 bar CH_3OH and below 570 K at 1 bar CH_3OH (Figure 5). Dissociative route transition states (TS2) have more positive enthalpies and entropies than the TS1 that mediates associative routes, thus making the rate constants for the latter less sensitive to temperature than for dissociative routes (Figure 5). At the low-temperatures of CH_3OH dehydration catalysis, associative routes are favored, as shown by kinetic and infrared data shown here, while at higher temperatures typical of CH_3OH conversion to hydrocarbons (~600 K), CH_3OH-DME interconversions become equilibrated and dissociation may occur, leading to the plausible involvement of methoxides in methylation of alkenes at high temperatures.[2, 20]

The preferred DME formation routes depend on CH_3OH pressure, because the stabilization of H-bonded monomers via dimer formation precludes their dissociation, and on temperature,

because lower temperatures favor the more “complex” but lower enthalpy TS that mediates associative routes. We surmise also that solvation by confinement within voids similar in size to the associative TS may enhance their contribution to measured DME formation rates, while dissociative routes may become prevalent for voids too small to contain associative TS, but able to solvate those involved in methoxide formation (and still fit the TS for the subsequent CH_3OH-methoxide complex in dissociative routes). For larger voids, including mesoporous structures, associative routes predominate at conditions of practical methanol dehydration catalysis.

Experimental Section

H-MFI (Zeolyst, Si/Al = 43) and the experimental protocols for measuring turnover rates and H^+ density are discussed elsewhere.[7] Activation energies and pre-exponential factors were determined from rate constants measured as a function of temperature (414 - 475 K; SI). The experimental setup for infrared spectroscopy is described elsewhere;[7] liquid CH_3OH (99.8%, Sigma-Aldrich) was introduced to flowing He (333 cm^3 g^{-1} s^{-1}, 99.999%, Praxair) via a syringe pump (Cole-Palmer 780200C series) into heated stainless steel lines (373 K) that connect to a quartz cell with NaCl windows. Periodic plane-wave DFT calculations were performed with projector augmented-wave potentials,[21, 22] an energy cutoff of 396 eV and the vdW-DF2[14] functional implemented in the Vienna *ab initio* simulation package (SI).[23, 24] Wavefunctions were converged to within 10^{-6} eV. Structures were relaxed until the forces on all atoms were <0.05 eV A^{-1}. TS structures were obtained from the nudged elastic band[25] and dimer[26] methods.

Figures, Tables and Schemes

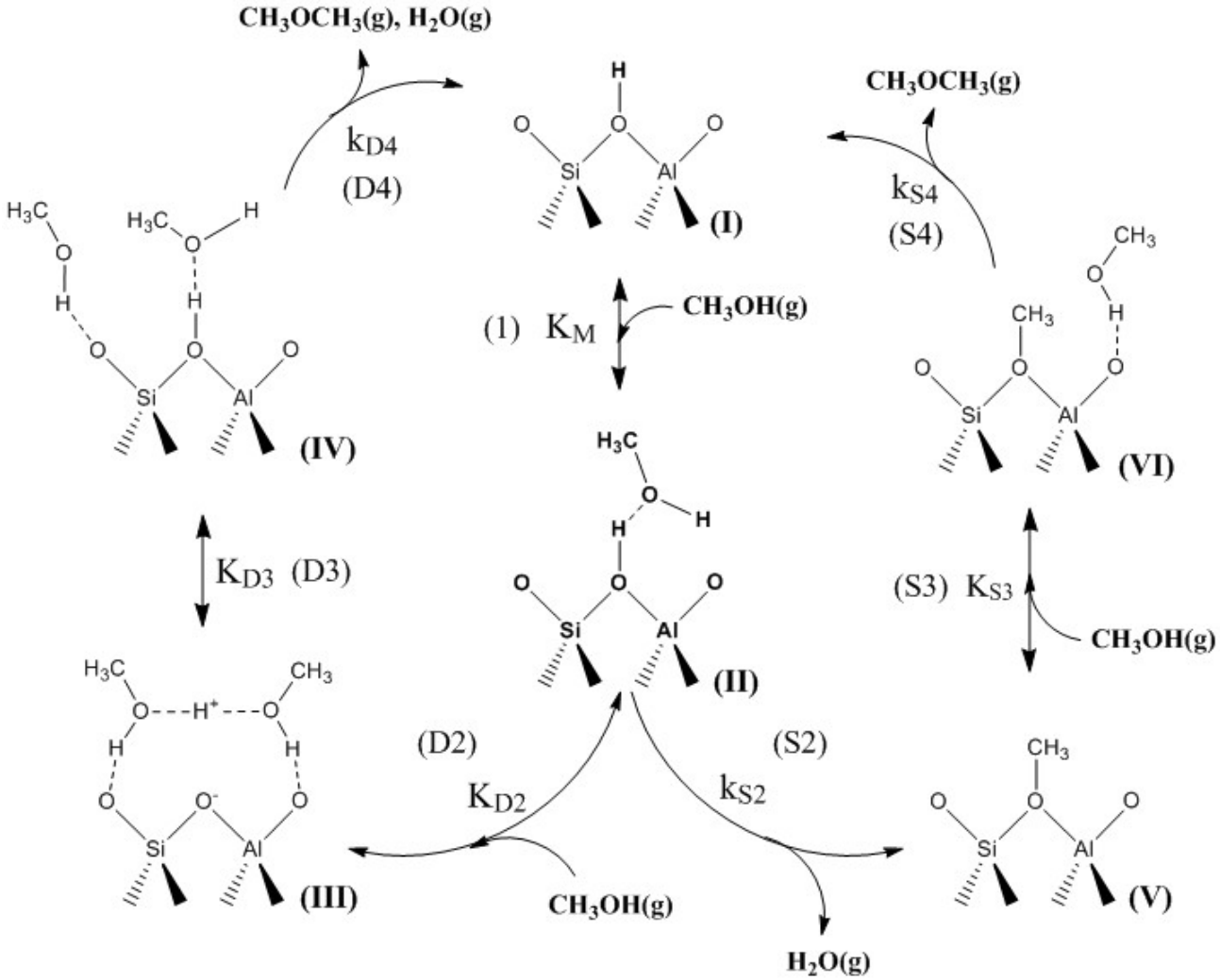

Scheme 1. Elementary steps for direct (associative; left cycle) and sequential (dissociative; right cycle) CH_3OH dehydration routes.

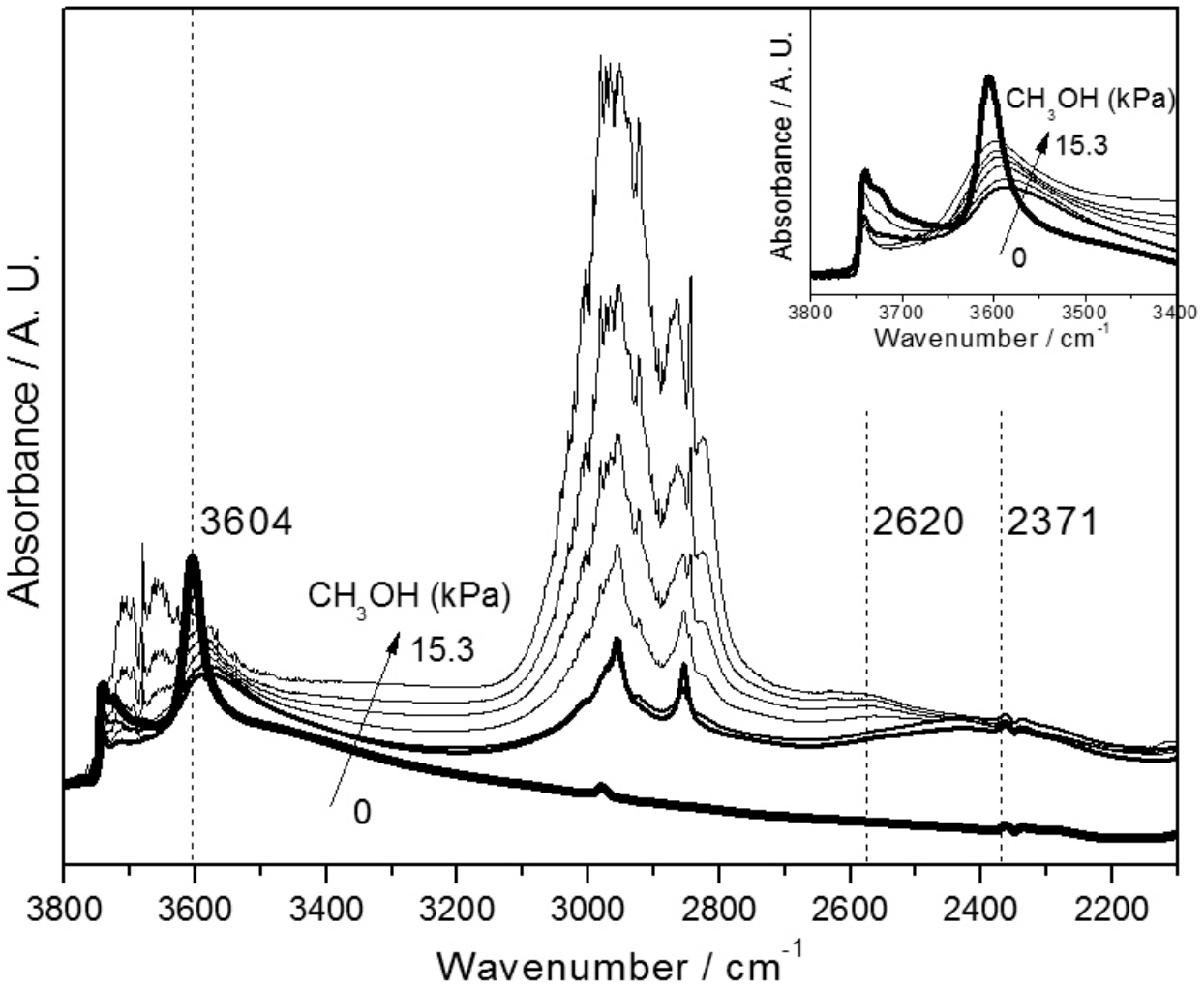

Fig. 1. Infrared spectra of MFI (Si/Al = 43) with increasing CH_3OH pressure (0, 0.2, 0.5, 1.5, 3.8, 7.7, 15.3 kPa; dark to light) during steady-state dehydration reactions at 433 K. Inset: difference spectra to remove absorptions from gaseous CH_3OH.

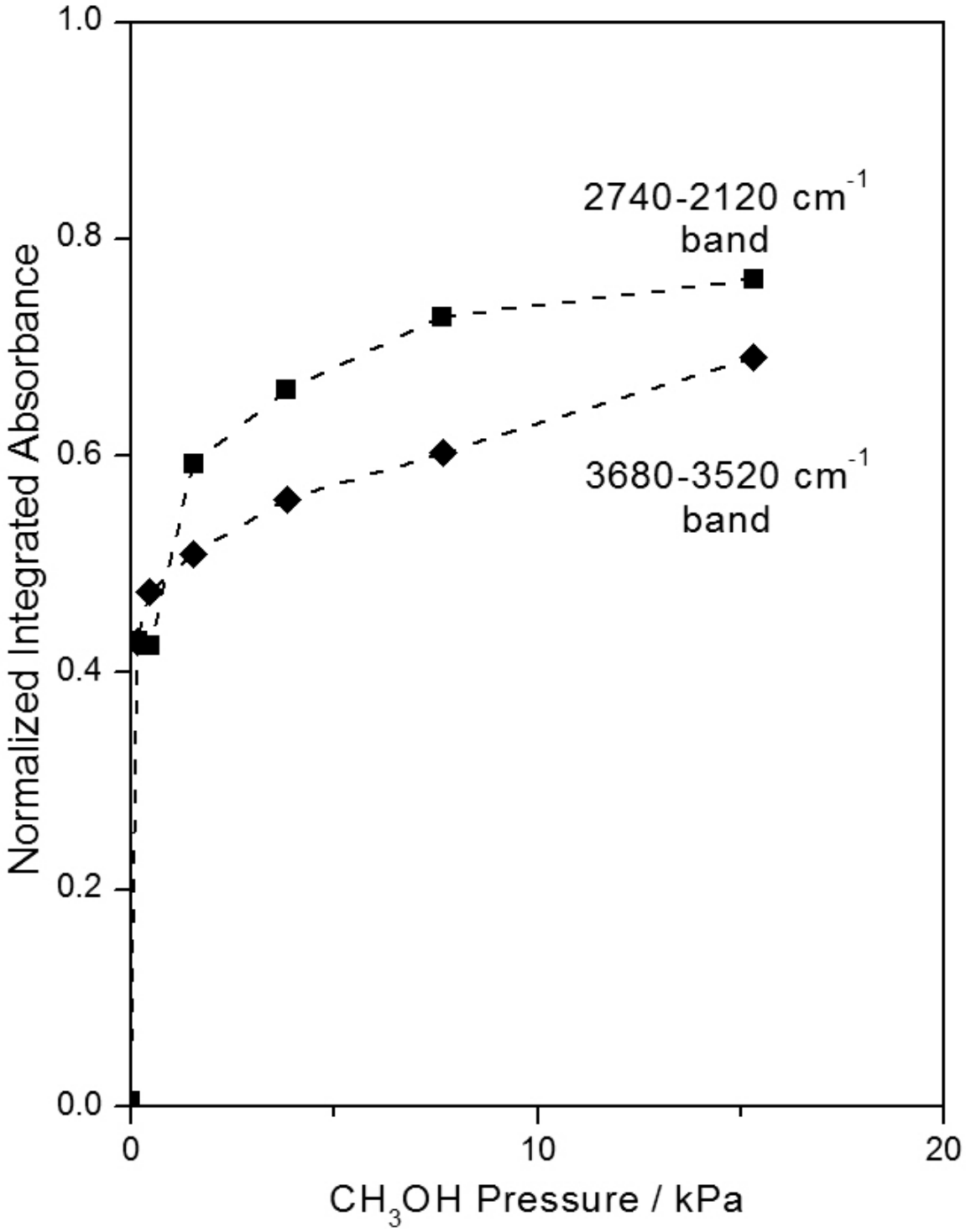

Fig. 2. Integrated absorbance of infrared bands characteristic of Brønsted ν(OH) from H-bonding with CH_3OH (2740-2120 cm^{-1}; ■) and CH_3OH ν(OH) perturbed by H-bonding (3680-3520 cm^{-1}; ◆) as a function of CH_3OH pressure normalized by the area of Si-O-Si overtone bands (2100-1730 cm^{-1}). Contributions of gaseous CH_3OH absorptions have been removed with details in the SI. Lines have been added to guide the eye.

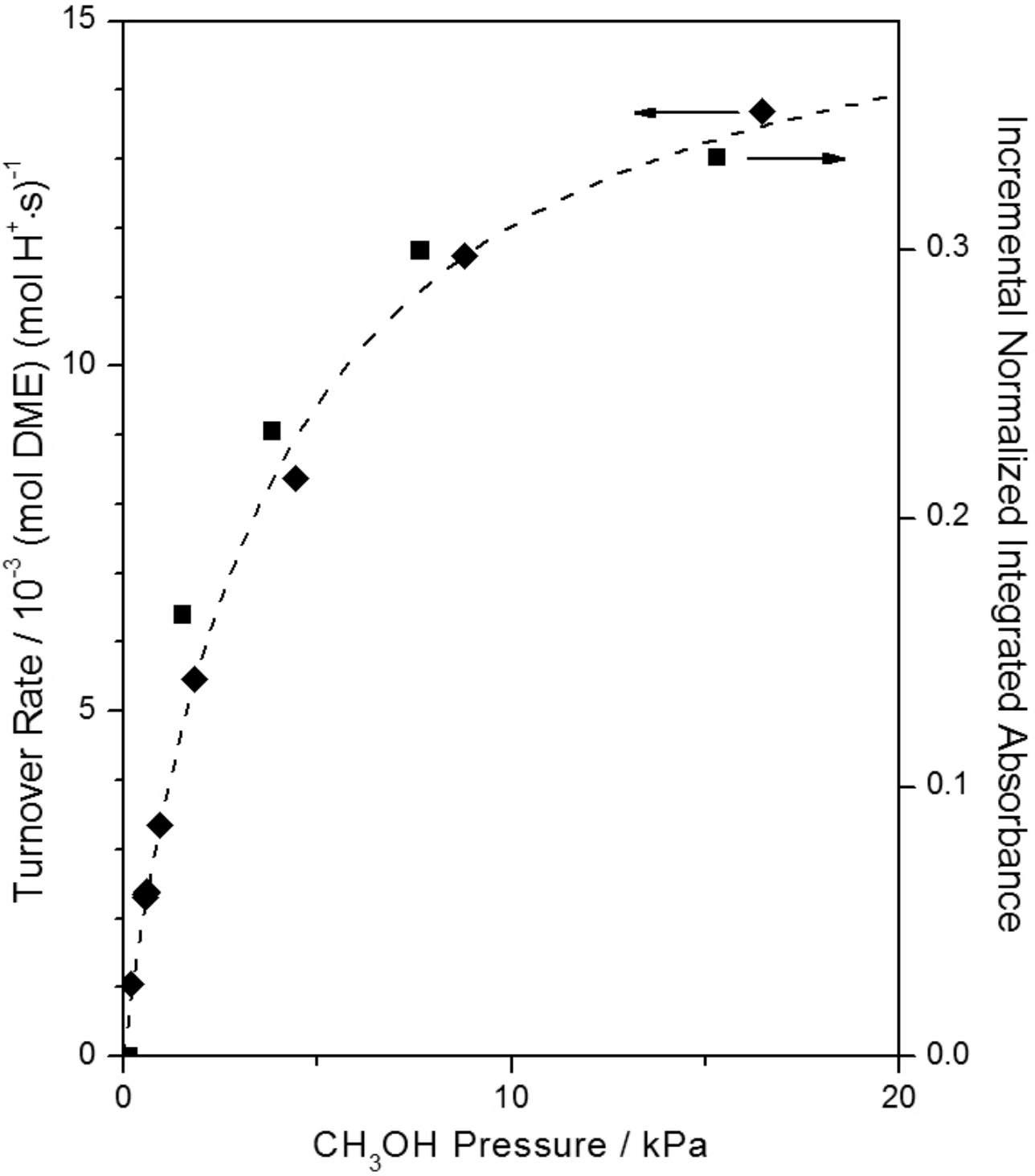

Fig. 3. CH_3OH dehydration turnover rates (◆) and integrated infrared absorbance of CH_3OH dimer ν(OH) perturbed by H-bonding (2740-2120 cm^{-1}; ■) normalized by the area of Si-O-Si overtone bands (2100-1730 cm^{-1}) as a function of CH_3OH pressure on MFI at 433 K. The absorbance data have been subtracted from the area of the same band at 0.5 kPa to remove contributions of CH_3OH.

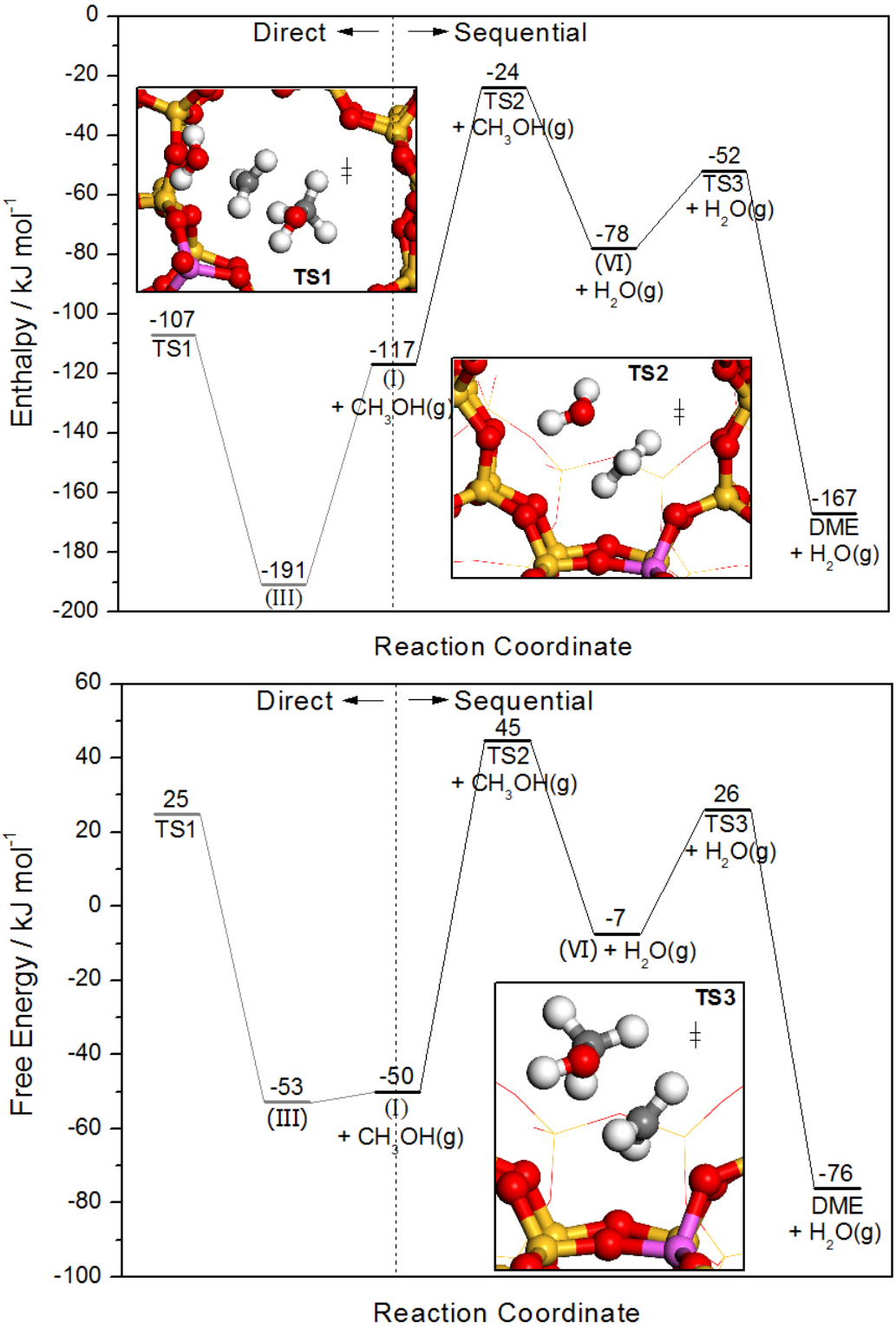

Fig. 4. Enthalpies (top) and free energies (433 K; bottom) of structures (Scheme 1) involved in direct (associative) (left; gray) and sequential (dissociative) (right; black) routes on MFI at the Al12-O20(H)-Si3 location from DFT (vdW-DF2/PAW). Energies relative to the bare zeolite and two CH_3OH(g). Atom colorings for TS structures are red (O), yellow (Si), purple (Al), gray (C), and white (H).

Table 1. Measured and calculated (vdW-DF2/PAW) enthalpic, entropic and free energy barriers for CH_3OH dehydration at 433 K. First-order and zero-order barriers refer to the energy of the direct transition state relative to CH_3OH monomers and CH_3OH(g), and CH_3OH dimers, respectively.

	Measured	**Calculated**
$\Delta H^{\ddagger}_{first}$ / kJ mol^{-1}	42 ± 2	10
$\Delta H^{\ddagger}_{zero}$ / kJ mol^{-1}	90 ± 2	84
$\Delta S^{\ddagger}_{first}$ / J (mol·K)$^{-1}$	-160 ± 10	-150
$\Delta S^{\ddagger}_{zero}$ / J (mol·K)$^{-1}$	-75 ± 2	14
$\Delta G^{\ddagger}_{first}$ / kJ mol^{-1}	111 ± 9	75
$\Delta G^{\ddagger}_{zero}$ / kJ mol^{-1}	123 ± 3	78

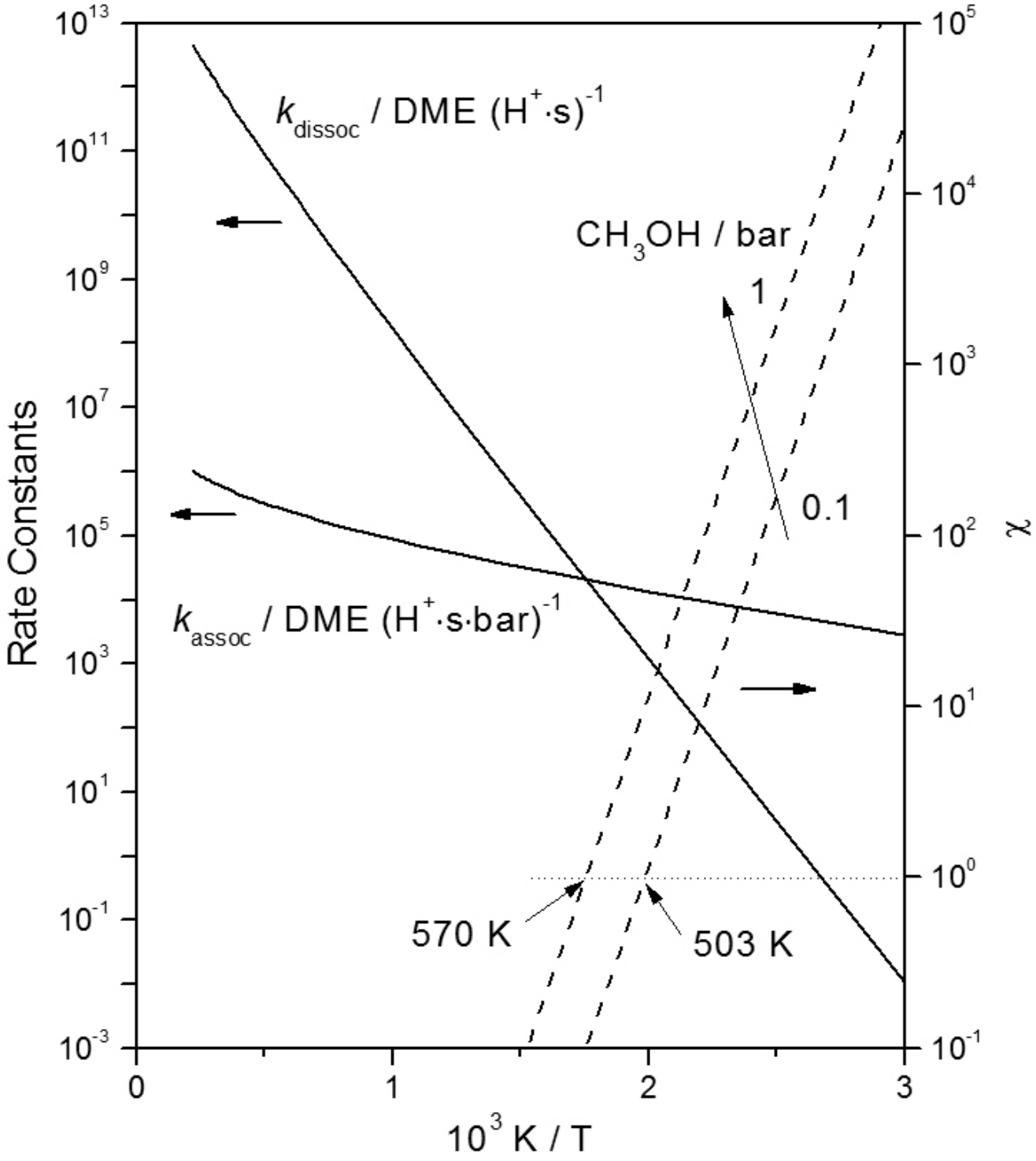

Fig. 5. Associative (k_{assoc} = $k_{D4}K_{D3}K_{D2}$, Scheme 1) and dissociative (k_{dissoc} = k_{S2}) rate constants and the ratio of associative-to-dissociative rates (χ; dashed lines) determined from Eqs. (3) and (4) at 0.1 and 1 bar CH_3OH estimated from DFT-derived enthalpies and entropies (vdW-DF2/PAW).

References

[1] R. Gounder, and E. Iglesia, Acc. Chem. Res. 45 (2012) 229-238.
[2] M. Stöcker, Micropor. Mesopor. Mater. 29 (1999) 3-48.
[3] R.T. Carr, M. Neurock, and E. Iglesia, J. Catal. 278 (2011) 78-93.
[4] S.R. Blaszkowski, and R.A. vanSanten, J. Phys. Chem. B 101 (1997) 2292-2305.
[5] P.G. Moses, and J.K. Norskov, ACS Catal. 3 (2013) 735-745.
[6] S.R. Blaszkowski, and R.A. vanSanten, J. Am. Chem. Soc. 118 (1996) 5152-5153.
[7] A.J. Jones, R.T. Carr, S.I. Zones, and E. Iglesia, J. Catal. 312 (2014) 58-68.
[8] A. Zecchina, S. Bordiga, G. Spoto, D. Scarano, G. Spano, and F. Geobaldo, Journal of the Chemical Society-Faraday Transactions 92 (1996) 4863-4875.
[9] P. Salvador, and W. Kladnig, Journal of the Chemical Society-Faraday Transactions I 73 (1977) 1153-1168.
[10] H. Yamazaki, H. Shima, H. Imai, T. Yokoi, T. Tatsumi, and J.N. Kondo, Angew. Chem. Int. Ed. 50 (2011) 1853-1856.
[11] W. Wang, A. Buchholz, M. Seiler, and M. Hunger, J. Am. Chem. Soc. 125 (2003) 15260-15267.
[12] W. Wang, and M. Hunger, Acc. Chem. Res. 41 (2008) 895-904.
[13] H. Yamazaki, H. Shima, H. Imai, T. Yokoi, T. Tatsumi, and J.N. Kondo, J. Phys. Chem. C 116 (2012) 24091-24097.
[14] K. Lee, É.D. Murray, L. Kong, B.I. Lundqvist, and D.C. Langreth, Physical Review B 82 (2010) 081101.
[15] A.J. Jones, S. Zones, and E. Iglesia, J. Am. Chem. Soc. submitted (2014).
[16] M. Brandle, and J. Sauer, J. Am. Chem. Soc. 120 (1998) 1556-1570.
[17] F. Göltl, A. Grüneis, T. Bučko, and J. Hafner, The Journal of Chemical Physics 137 (2012) -.
[18] T. Bucko, and J. Hafner, J. Phys.-Condes. Matter 22 (2010).
[19] T. Bučko, L. Benco, J. Hafner, and J.G. Ángyán, J. Catal. 279 (2011) 220-228.
[20] U. Olsbye, S. Svelle, M. Bjørgen, P. Beato, T.V.W. Janssens, F. Joensen, S. Bordiga, and K.P. Lillerud, Angew. Chem. Int. Ed. 51 (2012) 5810-5831.
[21] G. Kresse, and D. Joubert, Physical Review B 59 (1999) 1758-1775.
[22] P.E. Blöchl, Physical Review B 50 (1994) 17953-17979.
[23] G. Kresse, and J. Furthmüller, Physical Review B 54 (1996) 11169-11186.
[24] G. Kresse, and J. Hafner, Physical Review B 47 (1993) 558-561.
[25] G. Henkelman, and H. Jónsson, The Journal of Chemical Physics 113 (2000) 9978-9985.
[26] G. Henkelman, and H. Jónsson, The Journal of Chemical Physics 111 (1999) 7010-7022.

CHAPTER THREE

Acid Strength and Solvation in Catalysis by MFI Zeolites and Effects of the Identity, Concentration and Location of Framework Heteroatoms

Abstract

The effects of heteroatom identity (Al^{3+}, Ga^{3+}, Fe^{3+}, or B^{3+}), concentration, and location on catalysis by MFI zeolites is examined and interpreted mechanistically using methanol dehydration rate constants and density functional theory estimates of acid strength (deprotonation energies; DPE). In doing so, we shed light on the concomitant effects of confinement and acid strength on catalytic reactivity. Rate constants (per H^+ from pyridine titrations during catalysis) in the first-order and zero-order kinetic regimes decreased exponentially as the DPE of MFI with different heteroatoms increased. These trends reflect a decrease in the stability of ion-pair transition states relative to the relevant precursors (H-bonded methanol and methanol dimers, respectively, for these two regimes) with decreasing acid strength and resemble those in mesoporous solid acids (e.g. polyoxometalates). Confinement effects, weaker in mesoporous solids, give larger rate constants on MFI than on POM clusters with similar DPE. Such reactivity enhancements reflect the effects of MFI voids that solvate transition states preferentially over smaller precursors via van der Waals interactions with the confining voids. Both dehydration rate constants on MFI with 0.7-2.4 H^+ per unit cell volume (5.2 nm^3) are independent of Al or H^+ densities, indicating that neither H^+ location nor acid strength depend on acid site concentration. Higher site densities (3.6 H^+ per unit cell) lead to larger first-order rate constants, but do not influence their zero-order analogs. These data reflect, and in turn provide evidence for, the initial siting of H^+ in less constrained channel intersections and their ultimate placement within the more solvating environments of the channels themselves. Thus, the higher reactivity of Al-rich samples, often attributed to the stronger acid sites, arises instead from the ubiquitous role of zeolites as inorganic solvents for the relevant transition state, taken together with H^+ siting that depends on Al density. We find that heteroatom composition, but not Al density, influences acid strength in MFI, consistent with experiment and theoretical estimates of DPE, and that methanol dehydration rate constants, properly interpreted, provide relevant insights into the combined effects of acid strength and confinement on the reactivity of solid Brønsted acids.

1. Introduction

Zeolites are inorganic silica-based solids with microporous void structures and Brønsted acid sites that catalyze chemical reactions with unique reactivities and selectivities [1-4]. The isomorphous substitution of framework Si atoms with trivalent atoms (e.g. Al^{3+}, Ga^{3+}, Fe^{3+} or B^{3+}) creates anionic charges that can be compensated by protons located on bridging O-atoms (e.g., Al-O(H)-Si). The acid strength of X-MFI samples (where X indicates the isomorphous substitution of Si^{4+} by Al^{3+}, Ga^{3+}, Fe^{3+} or B^{3+}) depends on the identity of the trivalent framework heteroatom, as shown by deprotonation energy (DPE) estimates from density functional theory (DFT); these DPE values are much smaller for Al-MFI than for Ga-MFI, Fe-MFI or B-MFI (by 11, 23, 72 kJ mol^{-1} [5]). Absolute and relative DPE values differ among X-MFI samples [5-9], however, depending on the type and size of the zeolite model used. These differences reflect how

cluster and periodic models account for longer-range electrostatic interactions that stabilize the anionic framework after deprotonation [10, 11]. Therefore, it is necessary to compare and validate calculated DPE values with experimental estimates of acid strength.

Probes of solid Brønsted acid strength include adsorption enthalpies of amines [12], alkane cracking and dehydrogenation turnover rates [13], Hammett indicators [14], ^{13}C-NMR chemical shifts of adsorbed acetone [15] and Brønsted ν(OH) frequency shifts upon interactions with weak bases [16]. These probes often lead to conflicting conclusions about the acid strength of X-MFI, at least in part, because measured properties depend on the identity of the probe molecules and on the location of protons within the microporous voids, which leads, in turn, to differences in the dispersive stabilization of adsorbed probes because of local variations in void shape and size within a given framework structure [17]. For instance, differential adsorption enthalpies of NH_3 measured calorimetrically on Al-MFI and Fe-MFI zeolites are similar (-145 ± 5 kJ mol^{-1}), but these samples differ markedly in their n-hexane cracking turnover rates ($1.3 \cdot 10^{-3}$ vs. $0.048 \cdot 10^{-3}$ n-$C_6H_{14} \cdot (H^+ \cdot s)^{-1}$, 700 K) [18] leading to contradictory conclusions about their acid strength differences.

CH_3OH dehydration (to dimethyl ether; DME) rate constants on SiO_2-supported Keggin polyoxometalate (POM) clusters decrease exponentially with DFT-derived DPE estimates of the clusters [19]. First-order (k_{first}) CH_3OH dehydration rate constants reflect the free energy of the DME formation transition state relative to an uncharged adsorbed CH_3OH and a gaseous CH_3OH molecule (Scheme 1). Zero-order rate constants (k_{zero}) reflect the free energy of the same transition state, but in this instance relative to that of a cationic CH_3OH dimer (Scheme 1). The differences in charge and size between this transition rate and the two reactive intermediates (H-bonded CH_3OH monomers, k_{first}; protonated CH_3OH dimers, k_{zero}) causes these two rate constants to depend differently on acid strength and solvation by van der Waals interactions with the surrounding void environment. Therefore, such measurements on X-MFI samples may allow the independent assessment of their acid strengths and of their heteroatom siting among the diverse local environments provided by channels and intersections within MFI frameworks. Here, we report these rate constants on X-MFI, normalized by the number of protons and their DPE values, estimated by DFT methods through extrapolation to large MFI clusters.

2. Methods

2.1 Catalyst synthesis and characterization

Al-MFI was synthesized by dissolving $Al(OH)_3$ (53% Al_2O_3, Reheis F-2000 dried gel, 0.02-0.08 g) in a solution containing demineralized H_2O (6 g), tetra-n-propyl ammonium hydroxide (TPAOH, 40 wt%, Aldrich, 1.5 g) and NaOH (1 M solution in demineralized H_2O, Fisher, 1.5 g). Amorphous SiO_2 (Cab-o-sil M-5, 15 mmol) was added to the mixture, which was treated in a rotating sealed Teflon-lined vessel (43/60 Hz; Parr, 23 cm^3) held at 433 K for 6 days in a convection oven (Blue M). Solids were collected by vacuum filtration, washed with H_2O to reduce the pH to ~9, and treated in vacuum overnight at ambient temperature. Ga-MFI and B-MFI were synthesized by the same protocols using $Ga(NO_3)_3$ (nonahydrate, 99.9%, Aldrich, 0.03 g) and $Na_2B_4O_7$ (decahydrate, >99.5%, Aldrich, 0.06 g) instead of $Al(OH)_3$. The same procedure was used to prepare Fe-MFI, using $Fe(NO_3)_3$ (nonahydrate, >99.9%, Baker, 0.12 g), TPAOH (40

wt%, Aldrich, 2.4 g), NaOH (1 M solution in demineralized H_2O, Fisher, 0.5 mMoles), demineralized H_2O (4 g) and Cab-o-sil M-5 (20 mmol). Other Al-MFI samples were obtained from a commercial source (Table 1).

Samples were analyzed by scanning electron microscopy (JEOL JSM-6700F) and X-ray diffraction (Siemens D-500; Cu-K_α radiation) to determine their size and framework identity. Si, Al, Ga, Fe, B and Na contents were measured by inductively-coupled plasma optical emission spectroscopy (ICP-OES; Galbraith Laboratories; Supporting Information). The fraction of Al-atoms in tetrahedral and octahedral coordination was determined from ^{27}Al magic angle spinning NMR lines at 55 ppm and 0 ppm, respectively (details in Section S.2 of the Supporting Information).

2.2 Catalytic rate measurements

MFI samples were pressed, crushed using a mortar and pestle, and sieved (to retain 180-250 μm aggregates) and then diluted with SiO_2 (Cab-o-sil HS-5, washed with 1.0 M HNO_3, 180-250 μm pellets) to maintain a sample mass larger than >0.025 g. Samples were held on a coarse quartz frit within a tubular packed-bed quartz reactor (7.0 mm i.d.) and their mass (5-220 mg) was adjusted to conversions below 5%. The bed temperature was kept constant using a resistively-heated three-zone furnace (Applied Test Systems Series 3210) and Watlow controllers (EZ-ZONE PM Series); it was measured using a K-type thermocouple in contact with the outer surface of the quartz tube at the center of the catalyst bed.

All samples were treated in flowing 5% O_2/He mixture (83.3 $cm^3\ g^{-1}\ s^{-1}$, 99.999%, Praxair) by heating to 773 K (at 0.025 K s^{-1}), holding at 773 K for 2 h, and cooling to 433 K before catalytic measurements. Liquid CH_3OH (99.8%, Sigma-Aldrich) was introduced via heated lines (>373 K) into He flow (99.999%, Praxair) using a syringe pump (Cole-Palmer 780200C series). Reactant, product, and titrant concentrations were measured by gas chromatography (Agilent 6890N GC) using a DB-Wax capillary column (0.320 mm ID x 30 m x 0.50 μm film; J&W Scientific) and flame ionization, and mass spectrometric detection (MKS Spectra Minilab). Dimethyl ether and water were the only products observed at all reaction conditions.

CH_3OH dehydration rates (per mass) on SiO_2 (0.2114 g) and Silicalite-1 (SIL-1, 0.2236 g, synthesized using previously developed protocols [20] (Ludox AS-40, Sigma-Aldrich, silica source) were <0.03 of those on Al-MFI at all conditions; on SIL-1, such rates were ~20% of those measured on H-[B]-MFI (at 55 kPa CH_3OH). These SIL-1 rates were subtracted from measured H-[B]-MFI rates to account for contributions from the purely siliceous framework. Rates were measured periodically at a given reaction condition (10 kPa CH_3OH, B-MFI; 0.6 kPa CH_3OH, other X-MFI; 433 K); no deactivation was detected on Fe-, B-, and some Al-MFI samples (Si/Al = 22.8, 51.9, and 117.6). Al-MFI (Si/Al= 29.2 and 43.8) and Ga-MFI samples were corrected for slight deactivation (<15% over >5 h). Athena Visual Studio [21] was used to regress rate data to the functional form of the mechanism-based rate equations and determine 95% confidence intervals.

2.3 Chemical titration of sites with pyridine and decomposition of exchanged NH_4^+ cations

Brønsted acid sites were measured using pyridine (99.9%, Sigma-Aldrich) as a titrant during CH_3OH dehydration at 433 K. Pyridine (0.3 - 3.0 Pa) was introduced after establishing steady-state CH_3OH dehydration rates (10 kPa CH_3OH, B-MFI; 1.1 kPa CH_3OH on other X-MFI) by introducing a pyridine-CH_3OH liquid mixture into the reactor. Titrant effluent concentrations were measured using the chromatographic protocols described above. The number of protons in each sample was determined from the cumulative titrant uptakes of pyridine required to fully suppress CH_3OH dehydration rates (assuming a 1:1 pyridine:H^+ adsorption stoichiometry).

Protons were also measured by decomposition of NH_4^+ (to form NH_3) on NH_4^+-exchanged samples, prepared by treating the H^+ form of MFI in flowing dry air (2.5 cm^3 g^{-1} s^{-1}, UHP Praxair; heating to 823 K at 0.025 K s^{-1}, 4 h hold) and adding these samples to 0.1 M NH_4NO_3 (>98%, Sigma-Aldrich; 1 g zeolite per 300 cm_3) while stirring at 353 K for 4 h. The solids were recovered by filtration and the exchange procedure was carried out two more times. After the third exchange, samples were filtered, washed with 300 cm^3 demineralized H_2O, and allowed to stand in ambient air. NH_4^+-exchanged samples (0.05-0.13 g) were placed within the reactor described in Section 2.2 and heated to 923 K (at 0.833 K s^{-1}) in flowing He (2.5 cm^3 g^{-1} s^{-1}, 99.999%, Praxair) and Ar (0.83 cm^3 g^{-1} s^{-1}, 99.999%, Praxair) and held for 1 h. A heated, Si-coated stainless steel capillary (420 K, 0.254 mm i.d., 183 cm length) was placed directly after the samples and connected to a mass spectrometer (MKS Spectra Minilab) to measure NH_3 concentrations in the effluent stream. The intensities for NH_3 (17, 16 amu), H_2O (18, 17 amu) and Ar (40 amu) ions were acquired every 4 s.

2.4 Density functional theory calculations of deprotonation energy

Geometry optimizations were performed on neutral (ZH) and deprotonated (Z^-) clusters with the hybrid functional ωB97X-D [22] using the double-ζ, polarized valence 6-31G(d,p) basis set implemented in the Gaussian software package [23]. Wave-functions were converged to $1.0 \cdot 10^{-6}$ hartree and structures were optimized until the root-mean-square force was less than $3 \cdot 10^{-4}$ hartree $bohr^{-1}$. Single-point calculations on the resulting geometries were performed at the ωB97X-D/6-311++G(3df,3pd) level to test the effects of a larger basis set.

DPE values were calculated using cluster models derived from the MFI crystal structure [24] and terminated with H atoms (Si-H bond lengths fixed at 0.1455 nm [25]) to replace terminal O atoms while maintaining charge neutrality. Terminal SiH_x atoms were fixed during geometry optimizations while all other atoms were allowed to relax, thus preventing the energetic relaxation of clusters into structures unrelated to the periodic crystalline framework [26]. Si-H bonds were used instead of Si-O-H to terminate clusters, because Si-O-H leads to unrealistic electrostatic destabilization and large DPE values [11]. The T12 site of MFI, according to the numbering convention of Olson et al. [24], was considered as the heteroatom substitution site for all clusters, with a H^+ located in the X12-O20(H)-Si3 position (where X = Al, Ga, Fe or B) [25, 27]. The resulting H^+ resides in the void created by the intersection of the straight and sinusoidal channels in MFI.

MFI clusters with one X heteroatom and 5, 8, 11, 20, 27, 38 or 51 tetrahedral atoms (denoted as 5T etc.) were extracted from periodic MFI structures built from coordinates derived

from X-ray diffractograms [24] to look at the effect of increasing the number of Si and O atoms that lie between the acid site and the terminal Si atoms on DPE. The clusters with 5 and 38 T-atoms after relaxation are depicted in Figure 3 (heteroatom sites identified; other clusters in Section S.3 of the Supporting Information). Clusters with Fe heteroatoms were calculated with a spin multiplicity of six since Fe^{3+} has a high spin ground state (d^5) in tetrahedral coordination [8] and because spin polarized energy calculations on 5T clusters indicated that this was the most stable electronic configuration.

DPE values represent the energy required to heterolytically cleave H-atoms from the zeolite framework (HZ) to form a non-interacting H^+ and a zeolite framework anion, Z^-. DPE values were calculated as the energy difference between these deprotonation products and the neutral starting structure:

$$E_{DPE} = E_{Z^-} + E_{H^+} - E_{HZ} \quad (1)$$

where E_{Z-}, E_{H+}, and E_{HZ} are the electronic energies of the deprotonated zeolite anion, a bare proton, and the neutral Brønsted acid, respectively.

2.5 Infrared detection of Brønsted acid sites

Infrared spectra were collected in transmission mode using self-supporting wafers (~5-15 mg cm^{-2}) and a quartz vacuum cell with NaCl windows. Spectra were measured in the 4000-400 cm^{-1} range with a 2 cm^{-1} resolution using a Nicolet NEXUS 670 spectrometer equipped with a Hg-Cd-Te (MCT) detector by averaging 64 scans. Samples were treated by heating to 723 K (0.033 K s^{-1}) in dry air (1.67 cm^3 s^{-1}, zero grade, Praxair), holding for 2 h and then cooling to 433 K. Samples were evacuated using a diffusion pump (<0.01 Pa dynamic vacuum; Edwards E02) before collecting spectra. All spectra were normalized by the intensity of the Si-O-Si overtones (2100-1750 cm^{-1}).

3. Results and discussion

3.1 CH_3OH dehydration on X-MFI: Proton site counts and kinetic effects of CH_3OH pressure

Figure 1 shows CH_3OH dehydration rates (433 K; per heteroatom from elemental analysis; Table 1) as a function of pyridine titrant uptakes on X-MFI samples. CH_3OH dehydration rates decreased linearly with the amount of pyridine adsorbed (Figure 1); rates did not increase when pyridine was removed from the inlet stream, indicating that pyridine irreversibly titrates all sites active for CH_3OH dehydration. Pyridine (0.6 nm kinetic diameter [28]) can diffuse through MFI channels (10-MR channels, ~0.55 nm diameter) and is protonated by Brønsted acid sites, rendering such sites unreactive for CH_3OH dehydration, but it can also coordinate to Lewis acid sites in zeolites [29]. Larger 2,6-di-*tert*-butylpyridine (1.05 nm diameter) molecules selectively titrate Brønsted acid sites [30], but did not decrease rates on H-[Al]-MFI-1, indicating that such titrants cannot access H^+ within MFI channels and that the fraction of H^+ at external MFI surfaces is inconsequential for catalysis. We compare pyridine uptakes (Table 1) with ex-situ H^+ counts from the thermal decomposition of the NH_4^+-form of these zeolites to determine the quantity of Lewis acid sites from the difference of their values; these site counts are selective to

Brønsted acid sites because NH_4^+ cations in solution replace H^+ during exchange but do not coordinate to Lewis acid sites. NH_4^+ and pyridine uptakes were similar (within a factor of 0.8; Table 1) indicating that pyridine adsorbs negligibly at any Lewis acid sites that may be present on these samples. The negligible adsorption of pyridine on Lewis acid sites and the near complete suppression of DME formation rates by pyridine titrants on these samples indicate that Lewis acid sites do not contribute detectably to CH_3OH dehydration rates on these samples.

DME formation rates were fully suppressed by contact with pyridine on Ga-MFI and Fe-MFI samples, but small residual rates (~10% of initial rates) were detected after saturation titrant uptakes on B-MFI and on H-[Al]-MFI-6 (Figure 1). The small residual rates after titration do not appear to be the result of Lewis acid sites because pyridine titrants will also coordinate with Lewis acid sites if they are present [29]. They may instead reflect DME formation on H^+ that are accessible to CH_3OH reactants but inaccessible to pyridine titrants as the result of adsorbed pyridine molecules that hinder the diffusion of pyridine molecules to reactive H^+ or due to structural defects that occlude pyridine molecules from certain voids. Therefore, the total number of protons on each sample was estimated by extrapolating titrant uptakes to zero CH_3OH dehydration rates. They are reported in Table 1 along with sample provenance, chemical composition, and Al coordination determined from ^{27}Al MAS NMR.

Proton counts (per heteroatom) from pyridine titrations and NH_4^+ decomposition were smaller than unity (except for H-[Al]-MFI-4 and H-[Ga]-MFI; Table 1), indicating that some heteroatoms do not have associated protons of sufficient strength to protonate pyridine irreversibly. This may reflect distorted heteroatoms with tetrahedral or octahedral coordination or extra-framework phases [31, 32] that lack reactive protons. ^{27}Al MAS NMR data show that some samples contain more framework Al atoms (0.88 Al_{Td}/Al_{Tot}) than protons (from pyridine titration, 0.65 H^+/Al_{tot}) in H-[Al]-MFI-1 (Table 1), but NMR studies use samples hydrated at ambient conditions, which can re-form tetrahedral Al centers [33]. This may lead to Al species that are tetrahedral during NMR experiments but do not contain Brønsted acid sites after relevant catalyst pretreatment and reaction conditions [34]. The ubiquitous and variable H^+/Al_{Td} sub-stoichiometry make tetrahedral Al sites an equivocal surrogate for the number of protons, which must be determined instead by using specific titrants, whenever possible as catalysis takes place [34]. Here, we use pyridine uptakes, which titrate Brønsted acid sites in these samples, as an estimate of the number of protons in calculating turnover rates.

CH_3OH dehydration turnover rates (per H^+) are shown in Figure 2 as a function of CH_3OH pressure on X-MFI samples. Turnover rates on Al-MFI, Ga-MFI and Fe-MFI samples increased linearly with CH_3OH pressure below 3 kPa CH_3OH and then more gradually, consistent with a Langmuir-type rate equation:

$$\frac{r}{\left[H^+\right]} = \frac{k_{first}\left[CH_3OH\right]}{1+\frac{k_{first}}{k_{zero}}\left[CH_3OH\right]} \quad (2)$$

Here, k_{first} and k_{zero} are the regressed first-order and zero-order parameters that give rise to the dashed curves in Figure 2. Dehydration turnover rates on B-MFI samples increased linearly with CH_3OH pressure at all pressures (up to 60 kPa CH_3OH) so that only k_{first} could be measured.

Turnover rates were influenced by the identity of the heteroatom (Al, Ga, Fe, B) at low pressures (<10 kPa CH_3OH) in a manner consistent with their different DPE values (Section 3.2) and with the expectation that stronger acids, with a more stable conjugate anion, would lead to lower activation energies for reactions mediated by ion-pair transition states [35]. Turnover rates ultimately become zero-order in CH_3OH at higher pressures on Al-MFI, Ga-MFI and Fe-MFI; these constant values confirm the absence of mass transfer effects, a conclusion confirmed by the similar turnover rates measured on Al-MFI samples with different Si/Al ratios and crystal sizes (Section 3.4).

Next, we assess the acid strength of X-MFI samples using theoretical DPE values and use these values in Section 3.3 to interpret and compare rate constants in terms of the relative contributions of dispersive and electrostatic forces on the stability of the transition state and its relevant precursors.

3.2 Density function theory calculations of deprotonation energy

DFT-derived DPE values have been reported with contradictory results for zeolites using periodic [36, 37], embedded cluster [38, 39] and free cluster [5-8] models. Periodic boundary conditions give rise to spurious electrostatic interactions among the charge defects formed by deprotonation in neighboring cells [40-42], which have remained uncorrected in these previous studies. Embedding approaches connect cluster models, treated locally using rigorous quantum mechanics (QM), to a potential field that represents the periodic zeolite via linking H-atoms [39]. It remains unclear, however, how the presence and position of these linking atoms affect calculated DPE values as they have been shown to do for small clusters [11, 35]. In addition, the wave-function of the cluster region is not influenced directly by the charge distribution of the potential region [38], which may be important for describing the long-range electrostatics important in anion energy calculations of clusters [10, 11].

Cluster models represent small portions of larger periodic structures, which do not accurately represent the O:Si stoichiometry in zeolites; these clusters must be terminated abruptly in a way that influences DPE values [11, 35]. Large clusters mitigate the artifacts created by terminal atoms on the stability of the cluster to deprotonation [11], therefore, the use of large clusters represents the most reliable strategy to explore these electrostatic effects, albeit at significant computational expense. DPE values (calculated at the HF/3-21G level) oscillate with the monotonic addition of Si and O shells around an Al-atom in MFI for cluster models up to 8 tetrahedral-atoms (T-atoms) in size [11], but DPE values slowly converge to constant values with increasing cluster size [10]. The large clusters required to approach realistic electrostatic interactions (>46 T-atoms) [10] have not been used, to our knowledge, to calculate DPE values for MFI with heteroatoms other than Al, an approach that we follow here in order to assess the effects of acid strength on CH_3OH dehydration rate constants on X-MFI.

DPE values are shown in Figure 4 as a function of the reciprocal of the number of T-atoms in the clusters for each X-MFI composition. DPE values decreased with increasing cluster size (5-51 T-atoms), suggesting that (i) anionic charges are transferred (delocalized) many atom distances away or (ii) O, Si and terminal H atoms become polarized in the clusters through long-range electrostatic interactions with the anion; we will henceforth refer to these two scenarios as delocalization and polarization, respectively. These size effects are strongest for B-MFI, which shows the highest DPE value and the least stable anionic cluster (DPE decreased by 132 kJ mol^{-1} from 5T to 38T B-MFI clusters). This may reflect the small size of B^{3+} cations (effective ionic radius of 0.027 nm [43], absolute hardness of 111 eV [44]), which stabilizes negative charge less effectively than larger cations (e.g., Al^{3+} with an effective ionic radius of 0.054 nm [43], absolute hardness of 46 eV [44]), causing DPE values to be more sensitive to long-range effects that are more accurately described as the size of the clusters increase. The effects of the size of the clusters used on DPE estimates weaken for larger clusters (>20 T-atoms; Figure 4), suggesting that electrostatic interactions rigorously approach those found in actual zeolite lattices, as discussed by Brand et al. [10], and that the effects of delocalization or polarization do not extend far beyond the second coordination sphere of O-atoms from the heteroatom (where the first coordination sphere of O-atoms is defined as that containing O-atoms bonded directly to the heteroatom).

Next we consider the influence of basis set size on DPE trends with cluster size in Al-MFI clusters (Figure 4). Increasing the basis set size allows enhanced electron density polarization and diffuseness and may impact the ability of clusters to delocalize or polarize charge. Increasing the 6-31G(d,p) basis set to the near-complete 6-311++G(3df,3pd) decreased DPE values by 41 and 25 kJ mol^{-1} for Al-MFI with 5T and 20T clusters, respectively (Figure 4). The effects of the larger basis set decreases with increasing cluster size; extrapolation of the difference in DPE values calculated with the two basis sets to larger clusters suggests that DPE values are 19 kJ mol^{-1} larger for 6-31G(d,p) than for 6-311++G(3df,3pd) basis sets for clusters larger than 38 T-atoms (Supporting Information). This suggests that DPE values of 51T Al-MFI clusters calculated at the 6-311++G(3df,3pd) level are ~1200 kJ mol^{-1}, a value also reported for Al-MFI using embedding cluster methods (1200 kJ mol^{-1}) [38]. This value also resembles that inferred from 2-butanol dehydration rate constants measured on POM clusters and another aluminosilicate (H-Al-BEA; 1185 kJ mol^{-1}) [45]. The systematic effects of cluster size on DPE suggest that both basis sets give similar DPE differences among X-MFI samples; DPE comparisons among solid acids of different types (e.g. zeolites and heteropolyacids), however, require near-complete basis sets, similar structural models (e.g., cluster vs. periodic) and the same level of theory (e.g., DFT vs. MP2).

The strong and systematic effects of cluster size on DPE (>130 kJ mol^{-1} for B-MFI clusters from 5T to 38T) seem surprising for insulating frameworks where considerable charge transfer is not expected. The origins of these cluster size effects were probed by examining the electron density differences between neutral and deprotonated structures. Figure 5a shows the electron density distribution of the neutral (HZ) and anionic (Z^-) 38T Al-MFI clusters (with Al at the origin). The locations of peaks in Figure 5a align with the locations of the first (Al-O*) and second (Al-O-Si-O*) coordination spheres of O-atoms away from the heteroatom (the asymmetry of the cluster prevents the perfect assignment of subsequent electron density peaks because the O-atoms are located at various positions), consistent with the negative charge located

predominantly at these locations. Deprotonation of the cluster (Figure 5a) did not lead to detectable changes in the position of these peaks, but caused a large increase in electron density at 0.8 nm, which corresponds to the position of the second coordination sphere of O-atoms. This suggests that atom displacements resulting from deprotonation do not significantly influence the electron density because these would result in changes in the positions of peaks in Figure 5a. Instead, the increase in electron density upon deprotonation at the second coordination sphere O-atoms reflects either (i) charge delocalization or (ii) charge polarization of the atom or Si-O bond, which we discuss next.

The difference between electron densities for protonated and deprotonated 38T Al-MFI clusters (Figure 5a) is shown in Figure 5b. A positive feature indicates a loss of electron density at that position. The weak feature at ~0.3 nm shows that the O-atoms bonded to the Al heteroatom acquire only a small negative charge upon deprotonation and that this negative charge resides predominantly at more distant O-atoms (0.8 nm) in the second O-coordination sphere. The loss of electron density at 0.6 nm corresponds to the first coordination sphere of Si-atoms (Al-O-Si*). The similar size of the negative features at 0.6 and 0.8 nm, respectively, suggests that electron density moves from Si-atoms in the first coordination sphere (Al-O-Si*) to O-atoms in the second coordination sphere (Al-O-Si-O*) upon deprotonation. Therefore, the most evident changes in electron density upon deprotonation arise from the polarization of charge along the Si-O bond, which places a larger electron density on the second coordination sphere O-atoms and removes some electron density from the first coordination sphere Si-atoms. The delocalization of electron density near atoms close to the heteroatom, however, seems negligible, in view of the lack of strong features below 0.6 nm (Figure 5b), which would indicate a change of electron density near the Al heteroatom. The polarization of the Si-O bond may be the result of the loss of the electrostatic potential of the H^+ cation, which removes the long-range electrostatic attraction of electrons to the H^+ location, therefore allowing electrons to concentrate on distant but more electronegative O-atoms (instead of Si-atoms).

Changes in the cluster electron density upon deprotonation at distances beyond 1 nm from the Al center are evident in Figure 5b. These features are smaller than those residing at the second coordination sphere O-atoms. A Bader charge analysis [46] (Section S.5 of the Supporting Information) shows that individual Si and O charges change by less than a factor of 1.05 upon deprotonation, consistent with the low dielectric constants for aluminosilicates [47] and their consequent resistance to charge delocalization. We conclude that the deprotonation of clusters induces changes in the polarization of Si-O bonds and atoms (instead of a long-range delocalization of charge) and thereby changes the ability of the cluster to stabilize charge. DFT-derived DPE values converge only for cluster models larger than 20 T-atoms, in which second coordination sphere O-atoms are not connected to terminal Si-H bonds, suggesting that polarization up to the second O-atom coordination sphere is essential for stabilization of the negative charge formed upon deprotonation and therefore for accurate DPE calculations in zeolites. We note that only minor changes to the electron density are observed at the Al-O bonds, which may explain the consistency of DPE values calculated here and with embedded approaches, which allow for the polarization of the potential region by the anionic structure, but do not allow for the influence of the potential region on the wave-function of the QM cluster.

3.3 Mechanistic origins of CH_3OH dehydration rate constants

Next, we interpret measured CH_3OH dehydration rate constants (k_{first} and k_{zero}) in terms of elementary steps and their rate and equilibrium constants. DFT calculations and measured CH_3OH dehydration turnover rates indicate that CH_3OH dehydration proceeds via direct routes involving H-bonded monomers and protonated dimers on W-based polyoxometalate clusters (POM) [19]. Protonated CH_3OH dimers (middle, Scheme 1) form via reactions of gaseous CH_3OH with neutral CH_3OH monomers (left, Scheme 1) and then reorient to properly align the orbitals involved in the kinetically-relevant elimination step (right, Scheme 1).

DFT estimates of CH_3OH dehydration routes on small zeolite cluster models (3 T-atoms) previously showed that these direct routes are preferred over alternate sequential routes, involving methoxide intermediates, also on zeolitic protons [48, 49], but such clusters fail to capture van der Waals forces and long-range electrostatic interactions essential for accurate transition state energies within microporous voids. Yet, attractive induced-dipole forces, which are not accurately captured by most DFT functionals, should cause an even stronger preference for the larger transition states involved in direct routes, as long as such void spaces are large enough to contain them. CH_3OH monomers, but not methoxides, were detected in the infrared spectra of H-MFI and H-FAU during contact with CH_3OH at CH_3OH/Al_{Td} stoichiometries below unity, while protonated CH_3OH dimers became evident at higher CH_3OH contents [50]. The exclusive presence of monomers at low CH_3OH pressures and the linear increase in dehydration rates with CH_3OH pressure at these conditions (Figure 2) provide direct evidence for the involvement of direct routes on H-MFI (see Section S.6 of the Supporting Information). Protonated dimers, detected in the infrared spectra of working catalysts at higher CH_3OH pressures [50], are also consistent with direct dehydration routes and with the zero-order rate dependence observed at high CH_3OH pressures (Figure 2). The combination of DFT, infrared and kinetic evidence strongly suggest that zeolite protons catalyze CH_3OH dehydration through direct routes (Scheme 1).

Direct routes involving quasi-equilibrated CH_3OH adsorption, protons occupied by H-bonded CH_3OH monomers or protonated dimers, and H_2O elimination as the sole kinetically-relevant step lead to the rate equation (Eq. (3)) [19]:

$$\frac{r_{DME}}{\left[H^+\right]} = \frac{k_{DME} K_D \left[CH_3OH\right]}{1 + K_D \left[CH_3OH\right]} = \frac{k_{first} \left[CH_3OH\right]}{1 + \frac{k_{first}}{k_{zero}} \left[CH_3OH\right]} \tag{3}$$

where K_D is the equilibrium constant for adsorption of a CH_3OH on a H-bonded monomer to form the protonated dimer and k_{DME} is the rate constant for the formation of DME from protonated dimers (middle, Scheme 1). Measured zero-order rate constants (k_{zero}) reflect differences in free energy between the cationic DME formation transition state (right, Scheme 1) and the protonated dimer (middle, Scheme 1). First-order rate constants (k_{first}) reflect differences in free energy of the same transition state relative to a gaseous CH_3OH molecule and an essentially neutral adsorbed CH_3OH monomer (left, Scheme 1).

Reactions mediated by cationic transition states, as in the case of CH_3OH dehydration, exhibit activation enthalpies that decrease monotonically with decreasing DPE [35]. When

activation entropies do not depend strongly on acid strength, as expected for isostructural polyoxometalate clusters or X-MFI samples, activation free energies will depend linearly (and rate constants exponentially) on DPE values [19, 51], as we discuss in the next section.

3.4 Influence of acid strength on dehydration rate constants on substituted MFI and POM

Measured CH_3OH dehydration rate constants are shown as a function of DPE values (calculated on 38T clusters) for X-MFI in Figure 6. First-order and zero-order rate constants decrease exponentially with increasing DPE, consistent with activation barriers that increase linearly with increasing DPE for the cationic transition states that mediate these reactions [19, 35]. Activation barriers increase with increasing DPE when cationic DME formation transition state energies are more sensitive to changes in electrostatics (reflected in DPE values) than reactive intermediates (Scheme 1), as is the case here because of the higher charge in the DME formation transition states than in CH_3OH monomers or dimers [19, 48].

First-order and zero-order rate constants depend differently on DPE (Figure 6) because they reflect the energies of uncharged H-bonded CH_3OH monomers and protonated dimers, respectively, relative to the same cationic transition state (Scheme 1). In the case of first-order rate constants the transition state is preferentially stabilized over uncharged precursors with decreasing DPE because stronger acid sites are able to stabilize, through electrostatic interactions, cationic species more [19]. In the case of zero-order rate constants the influence of decreasing DPE is attenuated because changes in the electrostatic stabilizations of the cationic transition state and protonated dimer become similar due to their similar charge. Indeed, the Bader charge in the bridging H-atom in protonated CH_3OH dimer intermediates on POM is near unity (+0.88 to +0.86 e on P and Co POM, respectively) [19] indicating that this species is highly charged and would be stabilized similarly to the cationic transition state with changes in the electrostatic stability of the zeolite conjugate base.

DPE values for Ga-MFI and Fe-MFI differ only slightly (3.4 kJ mol^{-1}, 38T clusters) and are within the accuracy of DFT methods (±10 kJ mol^{-1} [39]). Measured rate constants are also similar for Ga-MFI and Fe-MFI samples (Figure 6); the ratios of Ga-MFI to Fe-MFI rate constants are 1.6 and 0.7 for first-order and zero-order rate constants, respectively. The difference in k_{first} values is especially small when compared with the nearly 10^6-fold differences in first-order rate constants among POM and X-MFI samples with DPE values that differ by 212 kJ mol^{-1} (Figure 7). The similar DPE and k_{first} values indicate that Ga-MFI and Fe-MFI samples have similar acid strength. This is inconsistent with the conclusions of previous DFT-derived DPE calculations of Ga-MFI and Fe-MFI which showed DPE differences of up to 20 kJ mol^{-1} [5, 7, 8] probably because of the small clusters used in their calculations (2 to 8 T-atoms).

Next, we examine how DPE influences values of k_{first} on MFI and POM catalysts (Figure 7). DPE values of POM clusters with W addenda atoms ($H_{8-n}X^{n+}W_{12}O_{40}$; 1080-1143 kJ mol^{-1} [19]) depend on the identity of their central atom (X^{n+} = P^{5+}, Si^{4+}, Al^{3+}, and Co^{2+}) and the concomitant change in their number of protons [52]. First-order rate constants on MFI and POM samples both decrease exponentially with increasing DPE (Figure 7), indicating that in all cases stronger acids preferentially stabilize the dehydration transition state over the H-bonded CH_3OH monomer. The slope of the correlation between $ln(k_{first})$ and DPE values for MFI and POM

samples is much smaller than unity (Figure 7), indicating that a large fraction of the energy required to separate the proton is recovered upon formation of the ion-pair at the transition state. The slopes (-d($ln(k_{first})$)/d(DPE)) are also similar on POM (0.08 ± 0.06) and MFI (0.11 ± 0.06), leading us to conclude that the fraction of the DPE recovered at the transition state is insensitive to the structure, composition, and void space of the solid acid [19].

The values of k_{first} predicted from trend lines for POM (Figure 7) at DPE values of X-MFI 38T clusters (1226-1292 kJ mol^{-1}) are much smaller than measured k_{first} values on X-MFI samples. In particular, Al-MFI and Co-based POM have similar k_{first} values (within a factor of 1.3), but they differ in DPE by 83 kJ mol^{-1}. These DPE differences are much larger than expected from inaccuracies in DFT methods (~10 kJ mol^{-1}) or the effects of different basis sets (~19 kJ mol^{-1}; Section 3.2) suggesting that these differences cannot be explained by differences in basis set size used to calculate DPE on these two systems (DPE values on POM were calculated with a plane wave basis set and Vanderbuilt ultrasoft pseudopotentials [19]). Instead, the larger k_{first} values on MFI samples than those expected for hypothetical POM samples with equivalent DPE suggests that the transition state and reactive intermediate energies reflected in k_{first} are influenced by interactions that are not described in DPE considerations.

Protons in MFI reside within small voids and adsorb CH_3OH with much greater enthalpies (115 ± 10 kJ mol^{-1}, microcalorimetry, 400 K; [53]) than estimates for CH_3OH interactions with protons on POM (62 to 75 kJ mol^{-1} calculated with VASP on Co and P POM, respectively; [19]). This difference is undoubtedly due, in part, to the van der Waals interactions and H-bonding of CH_3OH with framework O-atoms in MFI as demonstrated by CH_3OH adsorption enthalpies on silicalite (pure silica MFI) of 65 ± 10 kJ mol^{-1} (350 K, microcalorimetry, pure silica MFI [53]). These van der Waals interactions will also stabilize DME formation transition states and to a greater extent than H-bonded CH_3OH monomers because of its larger size and number of atoms (Scheme 1). Therefore, larger values of k_{first} for X-MFI than those of a hypothetical POM sample with the same DPE (by 612-fold at a DPE of 1226 kJ mol^{-1}) may be explained, at least partially, by differences in the van der Waals stabilization of the DME formation transition state, which benefits more from tighter confinement than the CH_3OH monomer. It is not clear, however, to what extent these interactions influence measured rate constants because the DPE values calculated on POM and X-MFI are at different levels of theory and thus are not directly comparable. The preferential solvation of transition states by van der Waals interactions has been explained previously as the “nest effect” in zeolite catalysis [54] and its influence on reactivity is discussed elsewhere [51, 55]. We conclude that k_{first} values compared on MFI and POM samples indicate that DME formation transition states benefit from confinement in the micropores of MFI.

3.5 Al density and acid strength in Al-MFI zeolites

In this section, we examine the effects of Al density on the reactivity of protons in MFI zeolite structures using mechanism-derived CH_3OH dehydration rate constants to probe how Al density influences the strength and location of Brønsted acid sites. Figure 8 shows k_{zero} and k_{first} as a function of Al or H^+ densities (per unit cell), determined by elemental analysis and pyridine titration, respectively, on Al-MFI samples of different provenance and Si/Al ratio (Table 1). The number of H^+ per unit cell decreases by more than five-fold (3.6 to 0.7 H^+/u.c) in these samples

(H-[Al]-MFI-1 to H-[Al]-MFI-6; Table 1). The values of k_{zero} (per H^+) are similar ($15 \cdot 10^{-3} \pm 3 \cdot 10^{-3}$ DME molecules$\cdot(H^+ \cdot s)^{-1}$) on all Al-MFI samples and do not show any discernible monotonic trend with changes in Al or H^+ density (Figure 8). These data indicate that acid strength is similar in these materials, in view of the fact that zero-order rate constants depend exponentially on DPE (Figure 6) and are insensitive to confinement differences in MFI voids because of the similar size of DME formation transition states and protonated dimers (Scheme 1 and [19]). This is consistent with similar DPE values calculated at three crystallographically unique tetrahedral Al-substitution sites (within 10 kJ mol^{-1}; QM-Pot) [39] and with geometric arguments that support the presence of isolated Al T-atoms in MFI at Si/Al ratios above 9.5 [56]; next-nearest-neighbor Al-atoms decrease the acid strength of associated Brønsted sites [36, 57]. First-order rate constants (per H^+) are similar ($4.2 \cdot 10^{-3} \pm 0.6 \cdot 10^{-3}$ DME molecules$\cdot(kPa \cdot H^+ \cdot s)^{-1}$) also on MFI samples at H^+/u.c. densities below 3.6, but are measurably higher on samples with higher Al contents. These data suggest that proton densities below 3.6 H^+/u.c. do not influence the size of the confining environment around protons, since the consequent solvation effects would influence k_{first} values because of the significant differences in size between the transition state and the relevant H-bonded CH_3OH precursors (Section 3.4).

At higher H^+/u.c. densities in H-[Al]-MFI-1 (3.6 H^+/u.c.) k_{first} values are three-fold larger than on the other Al-MFI samples (Figure 8), but k_{zero} values are similar. Therefore the higher k_{first} value at high H^+/u.c. densities does not reflect a decrease in DPE, because DPE will influence both rate constants (Figure 6). These differences may instead arise from a change in the solvating environment around H^+, which affect k_{first} more than k_{zero} because of the difference in the size and number of van der Waals contacts of the monomer and dimer species reflected in their values (Scheme 1 and [19]). The increase in dispersive stabilization suggested by larger k_{first} values reflects a smaller void space near protons at higher H^+/u.c. densities. Such smaller void spaces arise from (i) occlusion of void space by extra-framework Al (Al_{ex}) species, as shown in FAU samples [34]; (ii) van der Waals interactions of transition states with nearby H-bonded CH_3OH; or (iii) the preferential siting of H^+ (and their associated Al atoms) within channels instead of intersections in MFI.

Al_{ex} contents can be estimated from the difference between H^+ and Al contents (Table 1). This value is actually smaller for H-[Al]-MFI-1 (1.9 Al_{ex}/u.c.) than samples with lower k_{first} values (e.g. H-[Al]-MFI-2; 3.0 Al_{ex}/u.c.), inconsistent with occluded Al_{ex} as the cause of smaller local voids. In addition, the Al_{ex} density (1.9 Al_{ex}/u.c.) in H-[Al]-MFI-1 is small compared with the available void volume in MFI (4 intersections/u.c.) and with the Al_{ex} density (37 Al_{ex}/u.c.; 4 Al_{ex}/supercage) in H-USY, for which detrital Al decreases void size and stabilizes transition states [34]. Interactions between H-bonded CH_3OH and DME formation transition states require protons to be located at distances improbable for these proton densities (3.6 H^+/u.c.) for the large unit cells of MFI (2.0 x 2.0 x 1.3 nm^3; [58]) and the number of H^+ binding locations (192 O-atoms/u.c.).

MFI structures contain straight and sinusoidal 10-MR channels (ca. 0.55 nm diameter), which intersect to form ellipsoidal voids (0.64 nm included sphere diameter [59]). The location of Al among these two environments depends sensitively on synthesis protocols and is not always dictated by thermodynamic stability [60, 61]. In fact Al siting in MFI using ^{27}Al MAS NMR [60] and diffraction on Cs-[62-64] and Cu-[65] exchanged MFI show that only a few of

the 12 T-sites in MFI contain Al atoms and that the relative occupancy differs markedly among samples. The similar first-order rate constants in Al-MFI samples with low H^+ density (<3.6 H^+/u.c.; 5 samples) indicate that H^+ reside within similar environments and, in view of their proclivity for diverse distributions among T-sites, probably within only one of the two possible environments (channels or intersections). We conclude instead that protons first occupy T-sites at channel intersections in these samples. Indeed, 8 out of 12 T-sites in MFI lead to H^+ at such intersections. The preferential siting of H^+ at intersections was inferred from the formation of n-hexane "dimers" at each H^+ for samples with 2.7 H^+/u.c., which cannot take place at smaller channel locations [66].

The higher k_{first} value on H-[Al]-MFI-1 compared with samples of lower H^+ densities reflects transition state stabilization within more confined spaces, indicating that H^+ become increasingly sited within channels, instead of intersections, as the H^+ density increases. This is consistent with the appearance of a Brønsted ν(OH) band (3656 cm^{-1}) in the infrared spectra of H-[Al]-MFI-1 not found in H-[Al]-MFI-4 (Figure 9; ~3604 cm^{-1}), indicating that some H^+ species reside in a different environment than in samples with lower Al contents. These stretching bands have been used previously to distinguish OH species at different O-sites in FAU (sodalite vs. supercage; ~80 cm^{-1} difference) [34] and MOR (8-MR vs. 12-MR; ~20 cm^{-1} difference) [67]. However, the assignment of ν(OH) frequencies to acid strength or confinement differences is ambiguous because ν(OH) frequencies depend strongly on the local framework geometry at H^+ sites [39]. The adsorption enthalpy of n-butane at a H^+ in the channel intersections in MFI increases by 8 kJ mol^{-1} when n-butane points into the sinusoidal, instead of the straight, channel (calculated with DFT; [68]) suggesting that even subtle changes in the H^+ and thus the transition state position may be responsible for the three-fold difference in k_{first} (corresponding to a 4 kJ mol^{-1} difference in activation free energy barriers at 433 K; see Section S.7 of the Supporting Information). We speculate that the presence of four T-atom rings, which seem to correlate empirically with higher Al content zeolites, and which are part of the structural detail at the channel intersections in MFI, might favor preferential location for Al in these voids and explain the siting of Al in channels only after the saturation of these locations at high Al densities.

CH_3OH dehydration rate constants rigorously reflect the acid strength and void environment of Al-MFI samples of different provenance and H^+ density. Similar values of k_{zero} over a range of Al/u.c. or H^+/u.c. densities provide compelling evidence that acid strength is independent of Al and H^+ densities and of H^+ location on Al-MFI samples of different provenance. Values of k_{first}, however, are larger on an Al-MFI sample with the highest Al density (H-[Al]-MFI-1) indicating that Al preferentially occupies T-sites in channel intersection voids at low Al densities (Si/Al > 23) and populates locations within channels only at higher proton densities.

4. Conclusions

The mechanistic interpretation of CH_3OH dehydration rate constants per proton clarifies the effects of the identity (Al^{3+}, Ga^{3+}, Fe^{3+}, B^{3+}), concentration and location of heteroatoms on acid strength and solvation on a series of MFI samples. DFT-derived deprotonation energies (DPE; calculated rigorously on large clusters to mitigate the effects of cluster termination)

capture the changes in electrostatic stability that influence the stability of DME formation transition states reflected in CH_3OH dehydration rate constant values on POM and MFI samples of different composition. In turn, equivalent first-order and zero-order rate constants on a series of Al-MFI samples with a wide range of H^+ densities (0.7 – 2.4 H^+/u.c.) indicate that acid strength and H^+ location is independent of acid site concentration. The abrupt increase in first-order but not zero-order rate constants for samples with high H^+ density (3.6 H^+/u.c.) provide evidence for the preferential siting of H^+ in the channel intersection void of MFI and the ultimate placement of H^+ in channels only at these high site densities.

First-order rate constants decreased exponentially with DPE on X-MFI and W-based polyoxometalate (POM) solid acids to similar extents indicating the ubiquitous influence of DPE on the stability of DME formation transition states and relevant precursors regardless of catalyst structure or composition. Larger first-order rate constants on X-MFI than hypothetical POM samples at similar DPE values reflect the enzyme-like confinement and van der Waals stabilization of DME formation transition states in the microporous voids of X-MFI samples.

These findings reveal the fundamental and substantial influence of acid strength and solvation on the reactivity of solid Brønsted acids. First-order and zero-order rate constants measured on X-MFI samples and combined with rigorous DPE calculations clear up controversies surrounding the acid strength of MFI and indicate that heteroatom composition, and not density, influences the acid strength of X-MFI.

Acknowledgments

I acknowledge Dr. Rob Carr (UC Berkeley), Dr. Stacey Zones (Chevron), Dr. Rajamani Gounder (UC Berkeley) and Dr. David Hibbits (UC Berkeley) for helpful technical discussions throughout the course of these studies, Prof. Raul F. Lobo (Univ. of Delaware) for the Silicalite-1 sample, and Dr. Sonjong Hwang (Caltech) for the NMR spectra. We gratefully acknowledge the financial support for this research from the Chevron Energy Technology Company. AJ acknowledges a graduate research fellowship from the National Science Foundation. Supercomputing resources were provided by the Molecular Graphics and Computation Facility in the College of Chemistry at the University California, Berkeley under NSF CHE-0840505. We also thank Dr. George D. Meitzner for his technical comments and editing of this manuscript.

Figures, Tables and Schemes

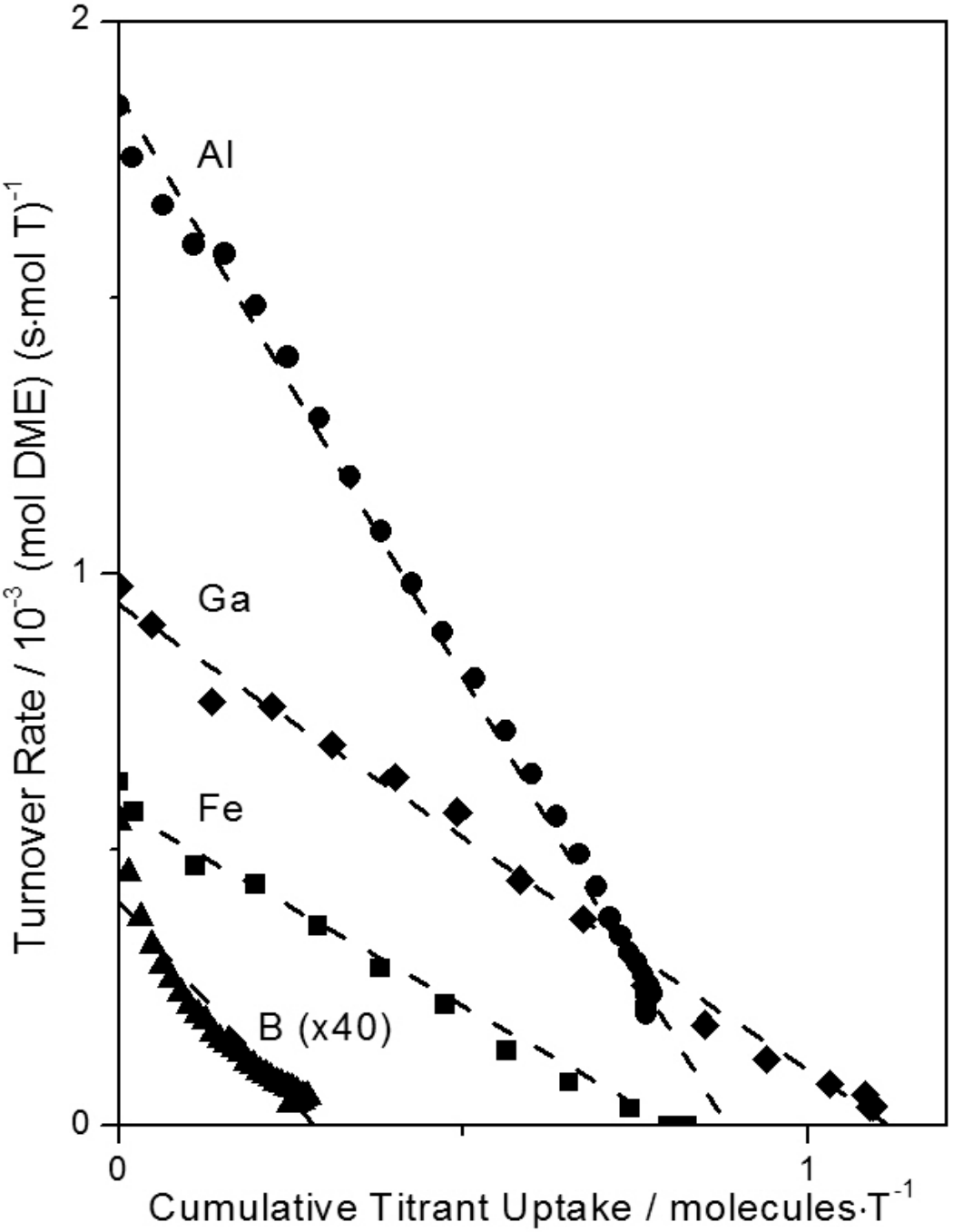

Fig. 1. CH_3OH dehydration rates at 433 K (per metal atom (T) measured from elemental analysis; Table 1) as a function of cumulative pyridine on H-[Al]-MFI-6 (●), H-[Ga]-MFI (♦), H-[Fe]-MFI (■) and H-[B]-MFI (▲) (1.1 kPa CH_3OH and 0.6 Pa pyridine for Al, Ga, and Fe substituted MFI samples; 10 kPa CH_3OH and 1.2 Pa pyridine for B-MFI). Dashed lines are linear regressed fits of the data.

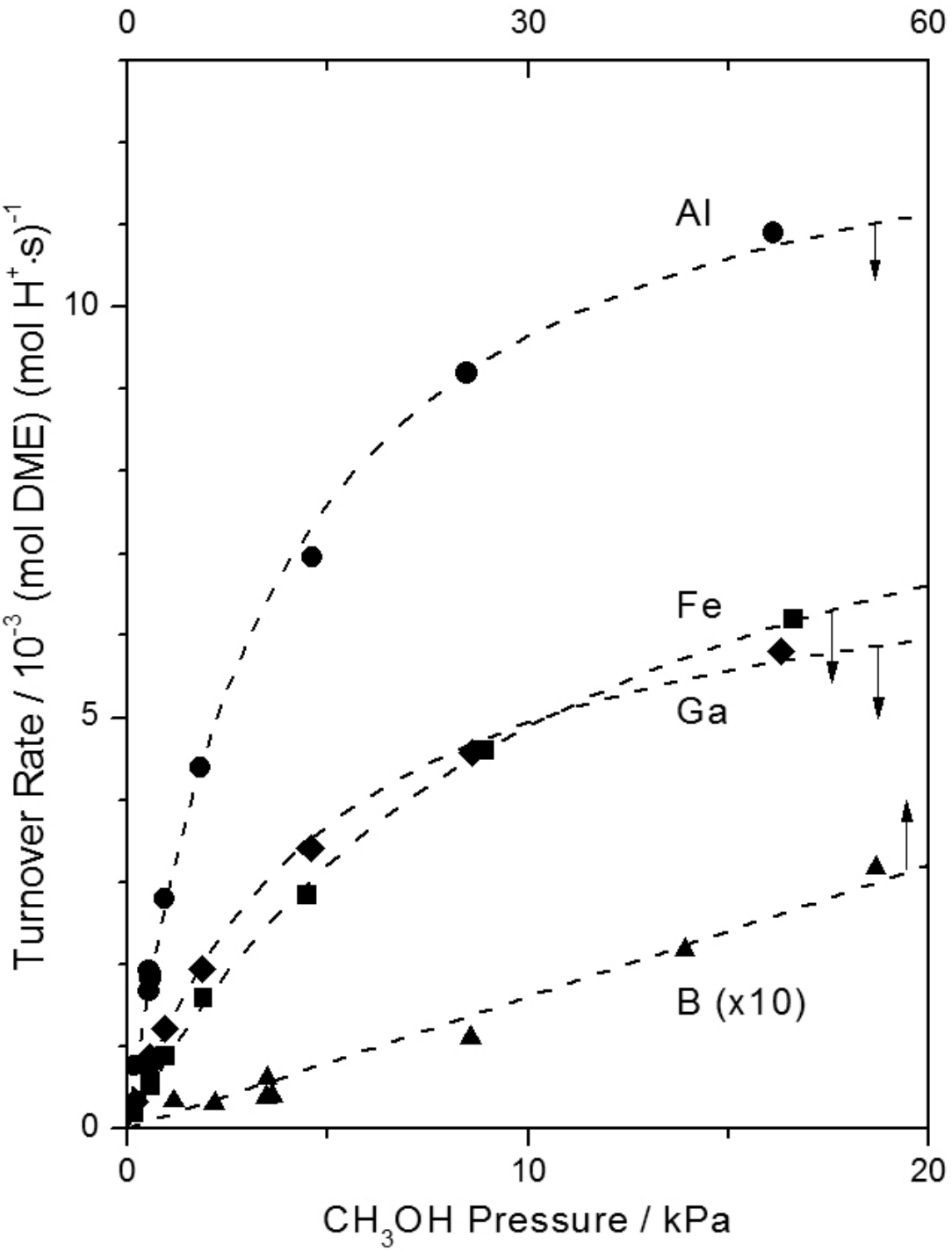

Fig. 2. CH_3OH dehydration turnover rates at 433 K normalized by pyridine uptakes on H-[Al]-MFI-6 (●), H-[Ga]-MFI (♦), H-[Fe]-MFI (■) and H-[B]-MFI (▲). Dashed curves represent regression of data points to equation 1.

Table 1. Zeolite sample information

Zeolite	Provenance	Si/T[a]	H^+/T[b]	H^+/T[c]	% T_{Td}[d]
H-[Al]-MFI-1	Commercial-1	16.6	0.65	0.52	88
H-[Al]-MFI-2	This work	22.8	0.27	0.33	85
H-[Al]-MFI-3	Commercial-1	29.2	0.77	0.72	89
H-[Al]-MFI-4	Commercial-1	43.8	1.03	0.89	89
H-[Al]-MFI-5	This work	51.9	0.59	-	87
H-[Al]-MFI-6	This work	117.6	0.86	-	96
H-[Ga]-MFI	This work	108.7	1.09	-	-
H-[Fe]-MFI	This work	61.1	0.85	0.68	-
H-[B]-MFI	This work	75.3	0.25	-	-

[a]Determined from elemental analysis (ICP-OES; Galbraith Laboratories).
[b]Determined from pyridine titrations during CH_3OH dehydration reactions at 433 K.
[c]Determined from NH_4^+ decomposition.
[d]Fraction of Al in tetrahedral coordination (%T_{Td}) determined from ^{27}Al MAS NMR.

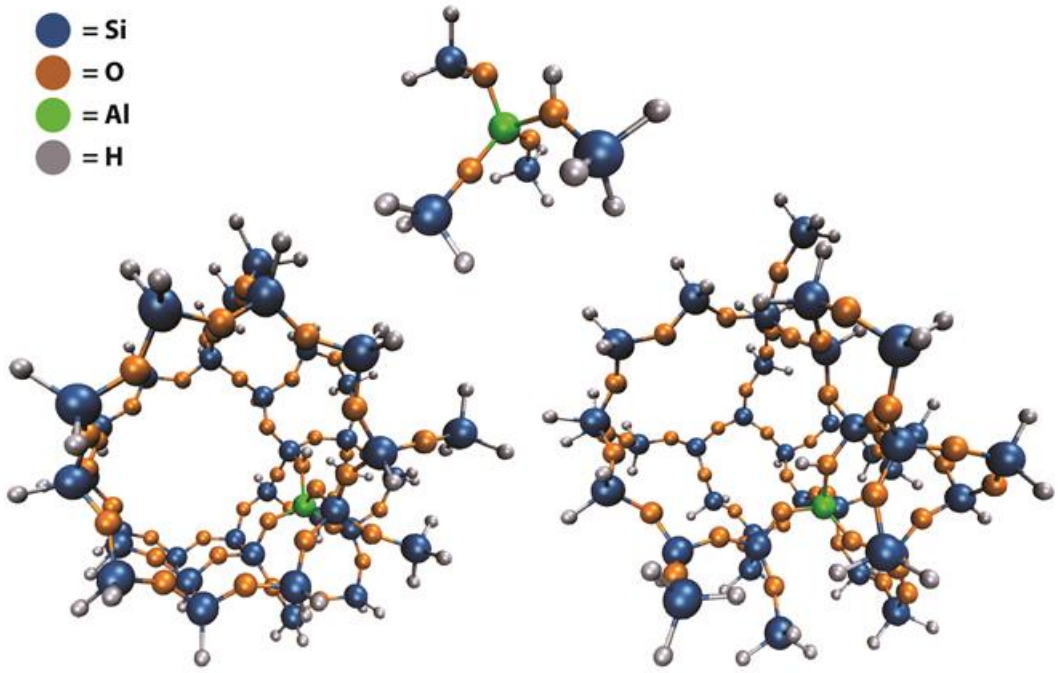

Fig. 3. Optimized geometries of $H_{13}Si_4Al_1O_3$ (5T; top) and $H_{55}Si_{37}Al_1O_{49}$ (38T; bottom) H-Al-MFI clusters (geometries for 8, 11, 20, 27 and 51 T-atom clusters provided in the Supporting Information). The 38 T-atom cluster is shown in two orientations looking down the 10-MR straight channel (left) and looking down the 10-MR sinusoidal channel at the void created from channel intersections (right). Atom colorings are as follows: H in gray, Si in blue, O in orange and Al in green.

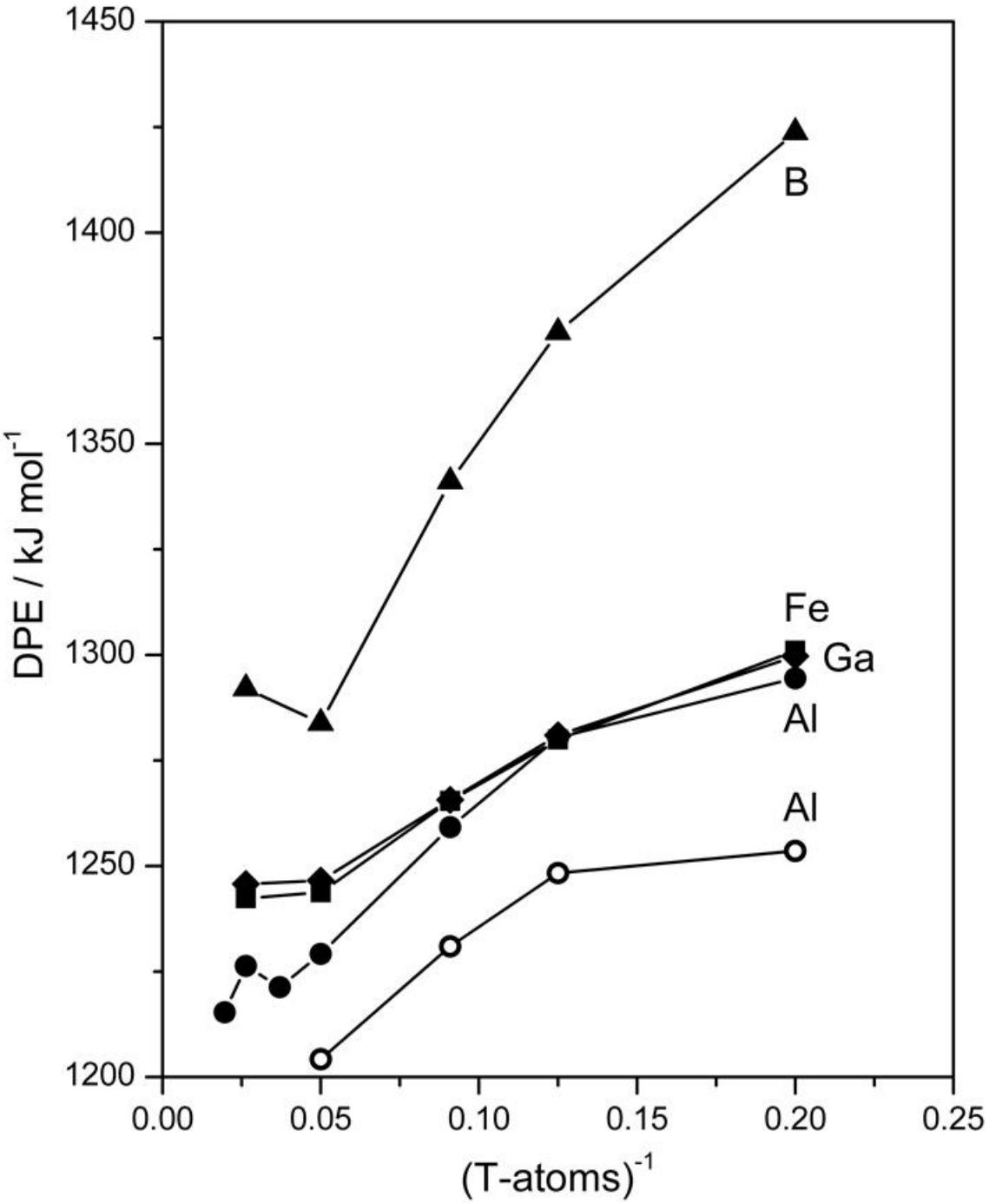

Fig. 4. Calculated DPE values for Al (●), Ga (♦), Fe (■) and B (▲) heteroatoms in MFI at the T12 site as a function of cluster size calculated with the ωB97X-D exchange correlation functional and a 6-31G(d,p) basis set. Open circles are single point calculations of optimized Al-MFI clusters with the 6-311++G(3df,3pd) basis set.

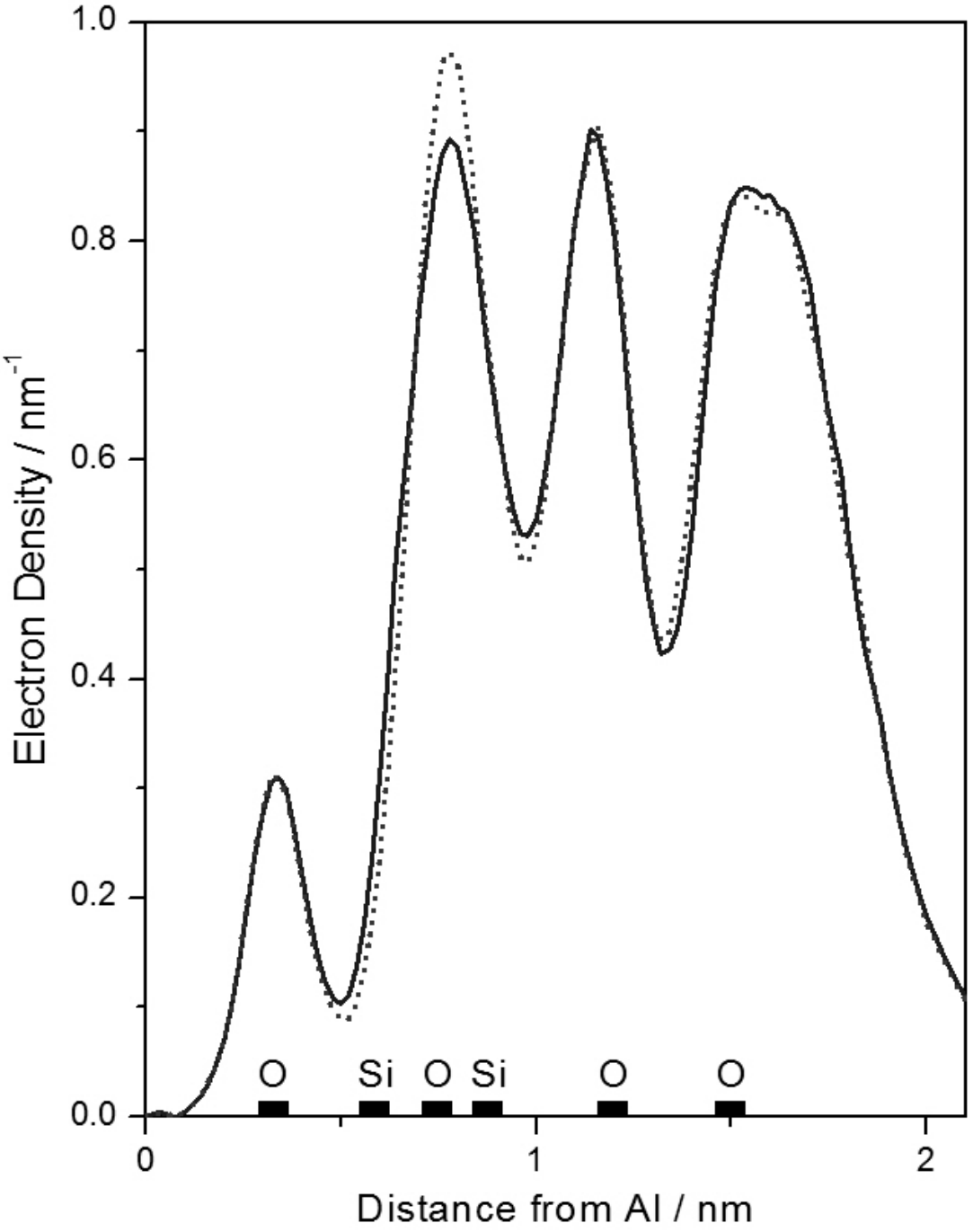

Fig. 5a. Electron density distribution of a 38 T-atom Al-MFI cluster as a function of the distance from Al before (solid line) and after (dotted line) deprotonation. Al is located at the origin; average positions of some O and Si atoms are identified for clarification.

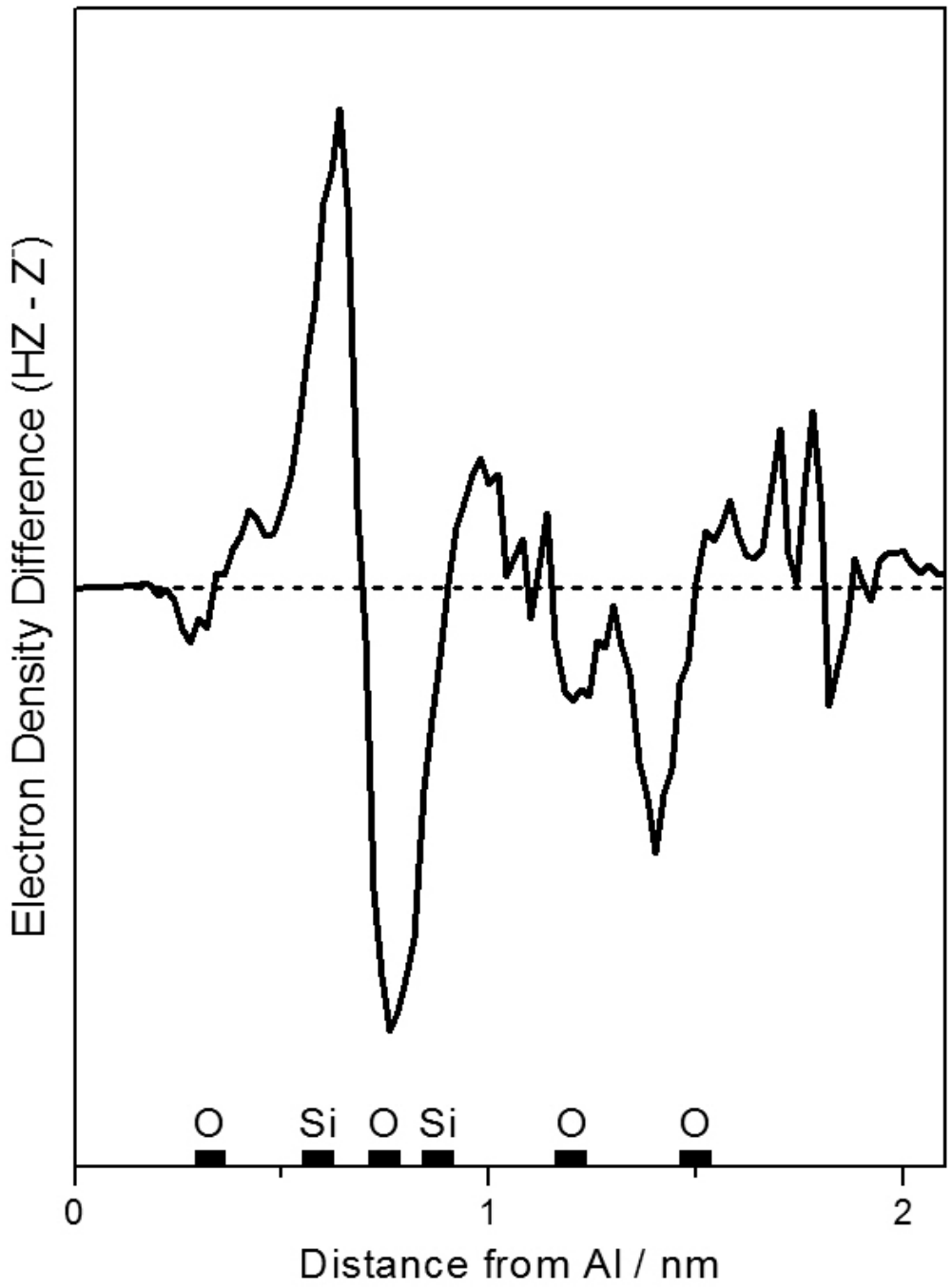

Fig. 5b. Difference in the electron densities between the protonated (HZ) and deprotonated (Z^-) 38 T-atom Al-MFI clusters in (Figure 5a). Al is located at the origin; average positions of some O and Si atoms are identified for clarification. Positive features indicate a loss of electron density in that region.

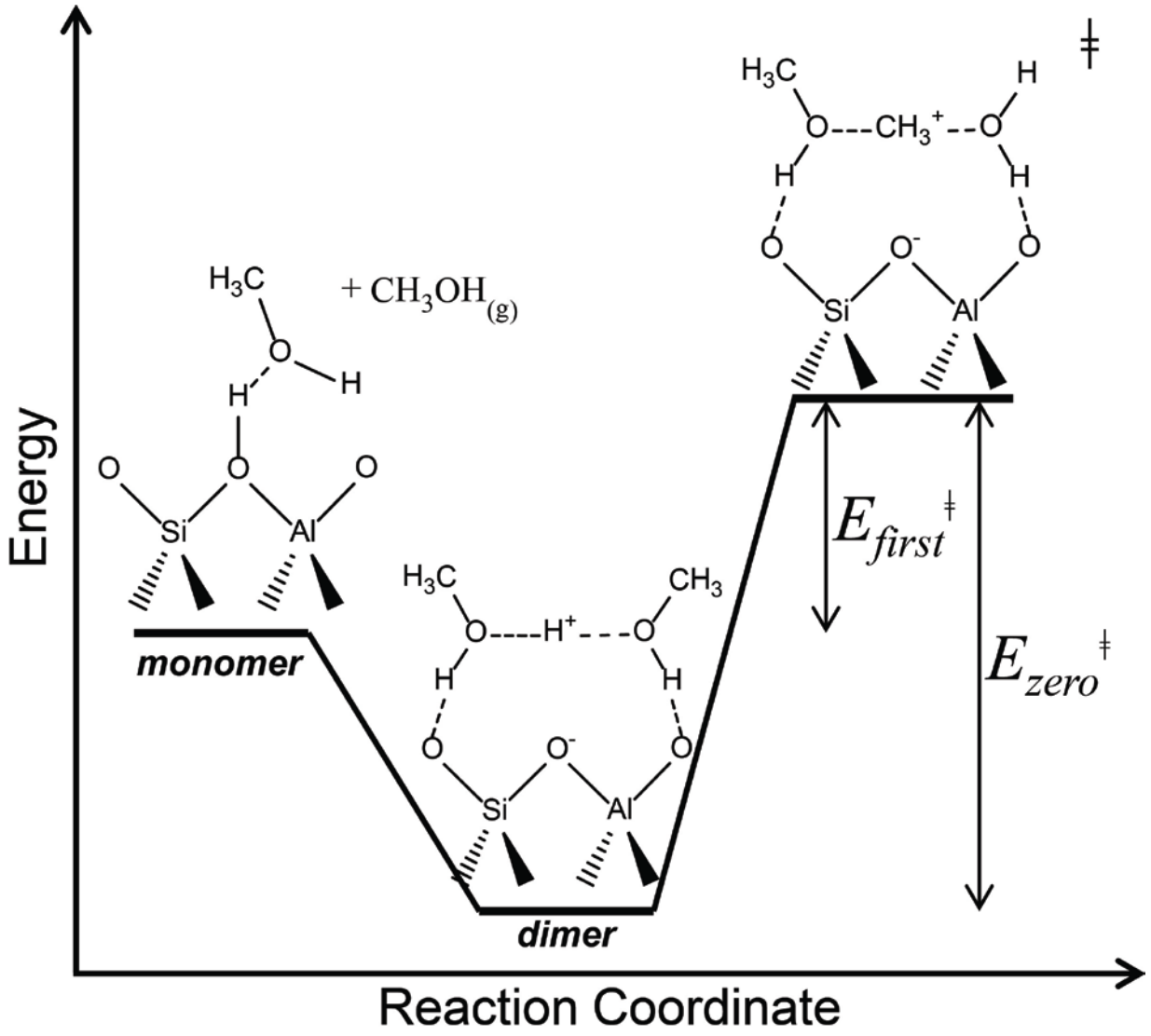

Scheme 1. Illustration of the relationships between the energies of H-bonded CH_3OH monomers, protonated dimers, and cationic DME formation transition states reflected in measured first-order ($E_{first}^{\ddagger}$) and zero-order ($E_{zero}^{\ddagger}$) CH_3OH dehydration rate constants.

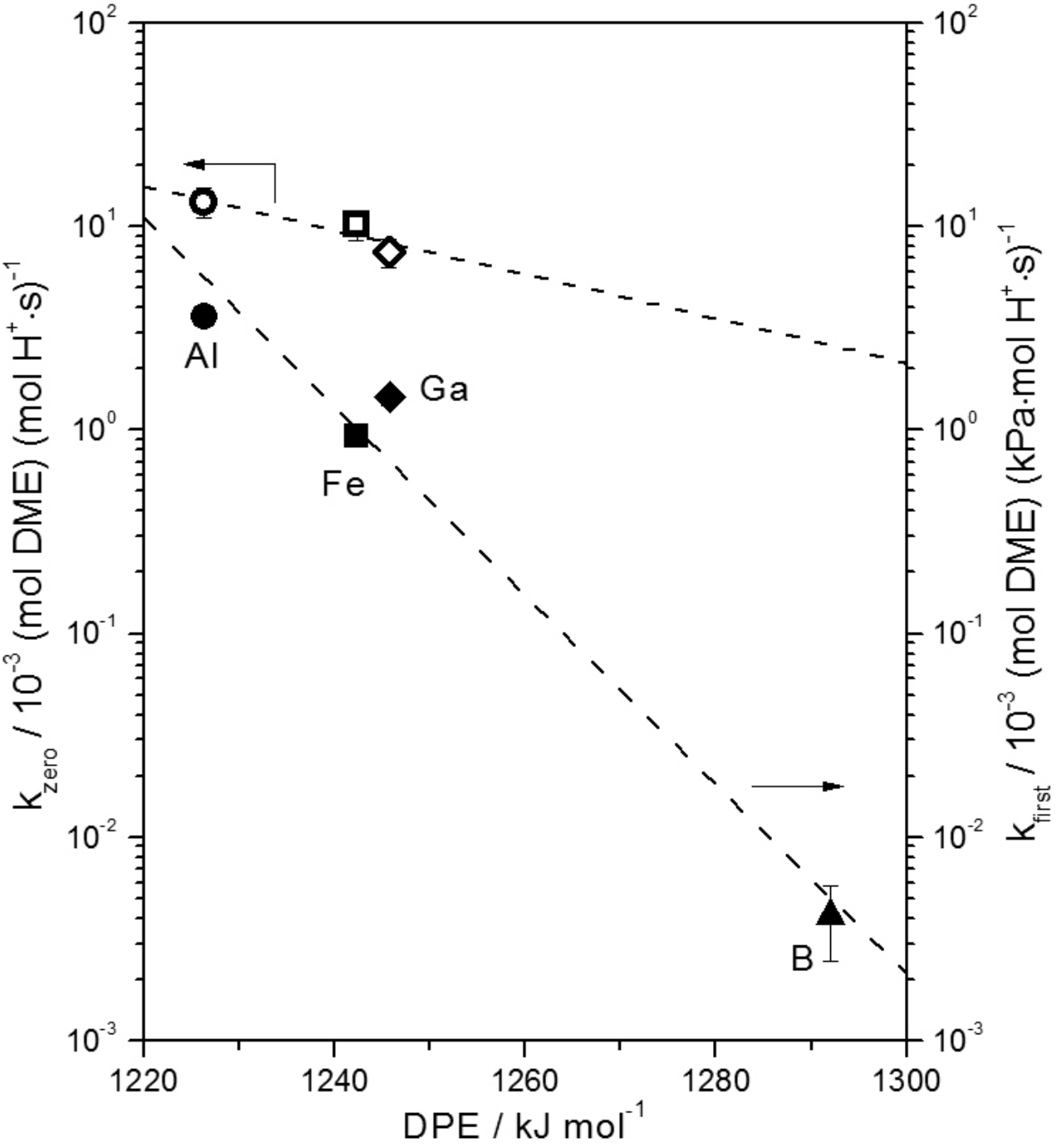

Fig. 6. First-order (closed) and zero-order (open) CH_3OH dehydration rate constants at 433 K plotted at their respective DPE values calculated on 38 T-atom clusters for H-[Al]-MFI-5 (●), H-[Ga]-MFI (♦), H-[Fe]-MFI (■) and H-[B]-MFI (▲). Dashed lines represent least squares regression of the natural log versus DPE values. The value of k_{zero} for B-MFI is unavailable experimentally because of the much higher CH_3OH pressures required to reach CH_3OH dimer-saturated surfaces.

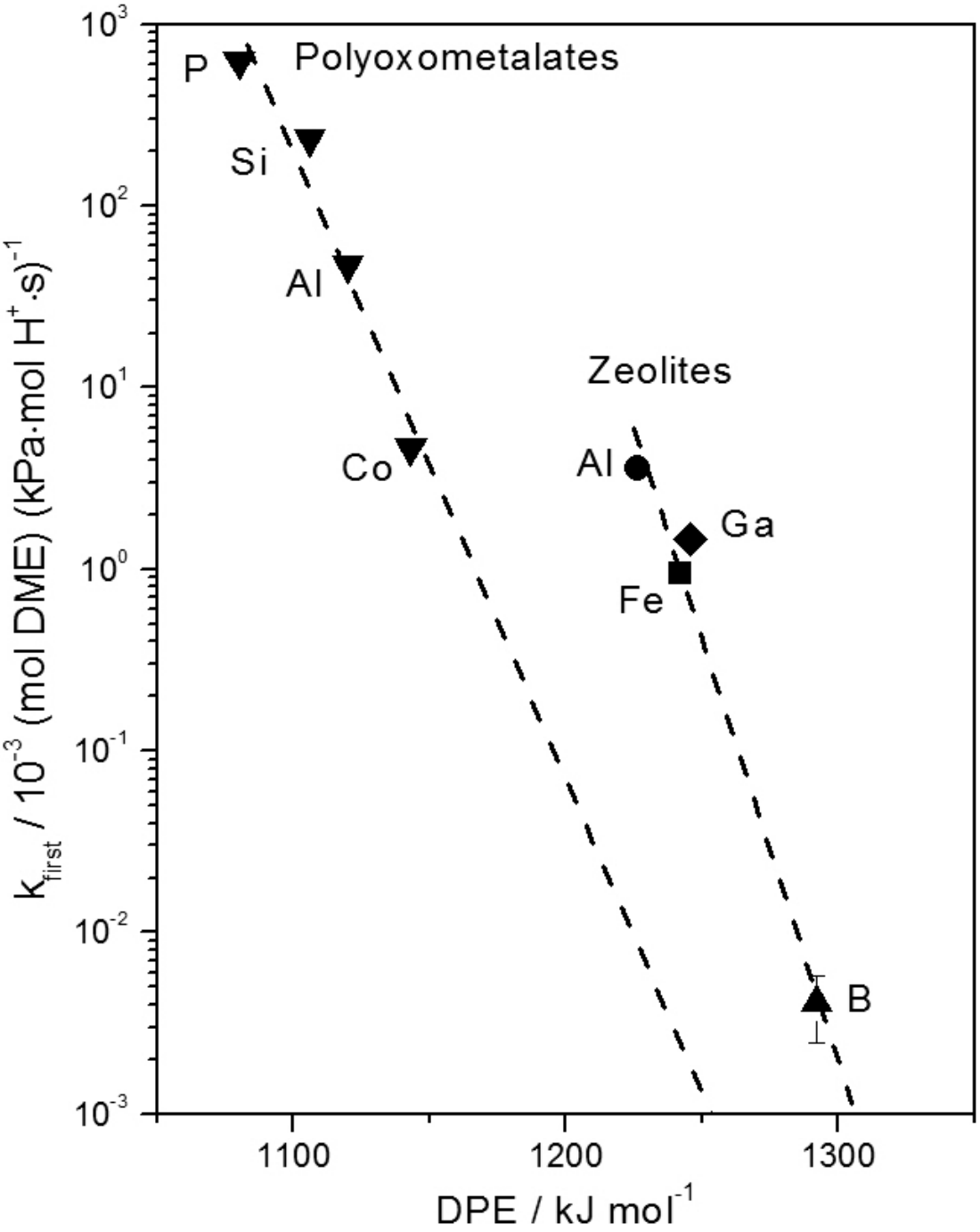

Fig. 7. First-order CH_3OH dehydration rate constants at 433 K plotted at DPE values calculated for 38 T-atom clusters for H-[Al]-MFI-5 (●), H-[Ga]-MFI (♦), H-[Fe]-MFI (■), and H-[B]-MFI (▲), and for $H_{8-n}X^{n+}W_{12}O_{40}/SiO_2$ (in order of increasing DPE: X = P, Si, Al, Co) samples (▲) taken from Carr et al. [19] at their calculated DPE values. Dashed lines represent least square regressions of natural log versus DPE data.

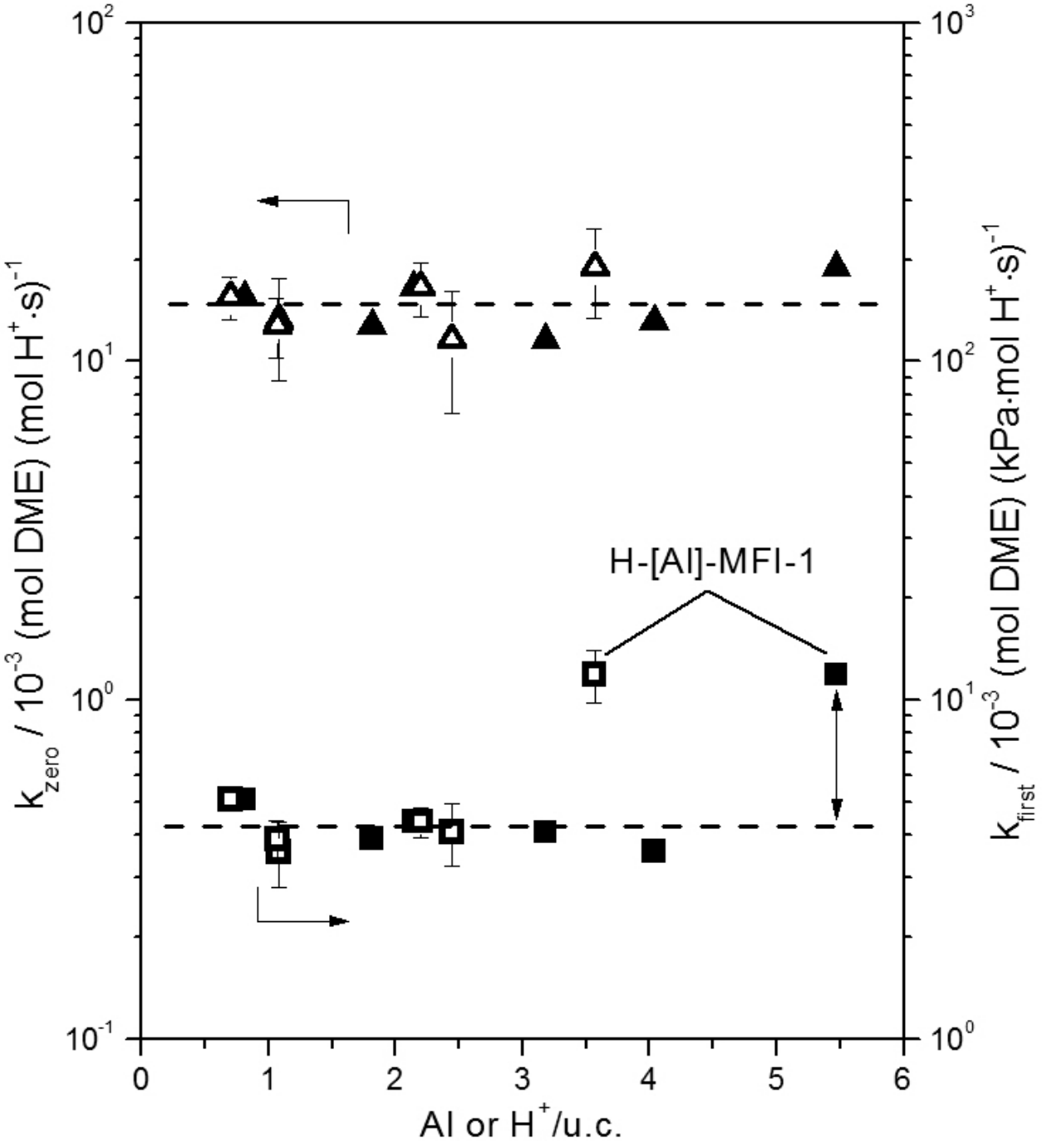

Fig. 8. First-order (■) and zero-order (▲) CH_3OH dehydration rate constants at 433 K on Al-MFI samples of varying provenance and Al (closed) or H^+ (open) densities per unit cell (Table 1; H-[Al]-MFI-1 through 6) determined from elemental analysis and pyridine titrations, respectively. Horizontal dashed lines are provided as a guide to the eye.

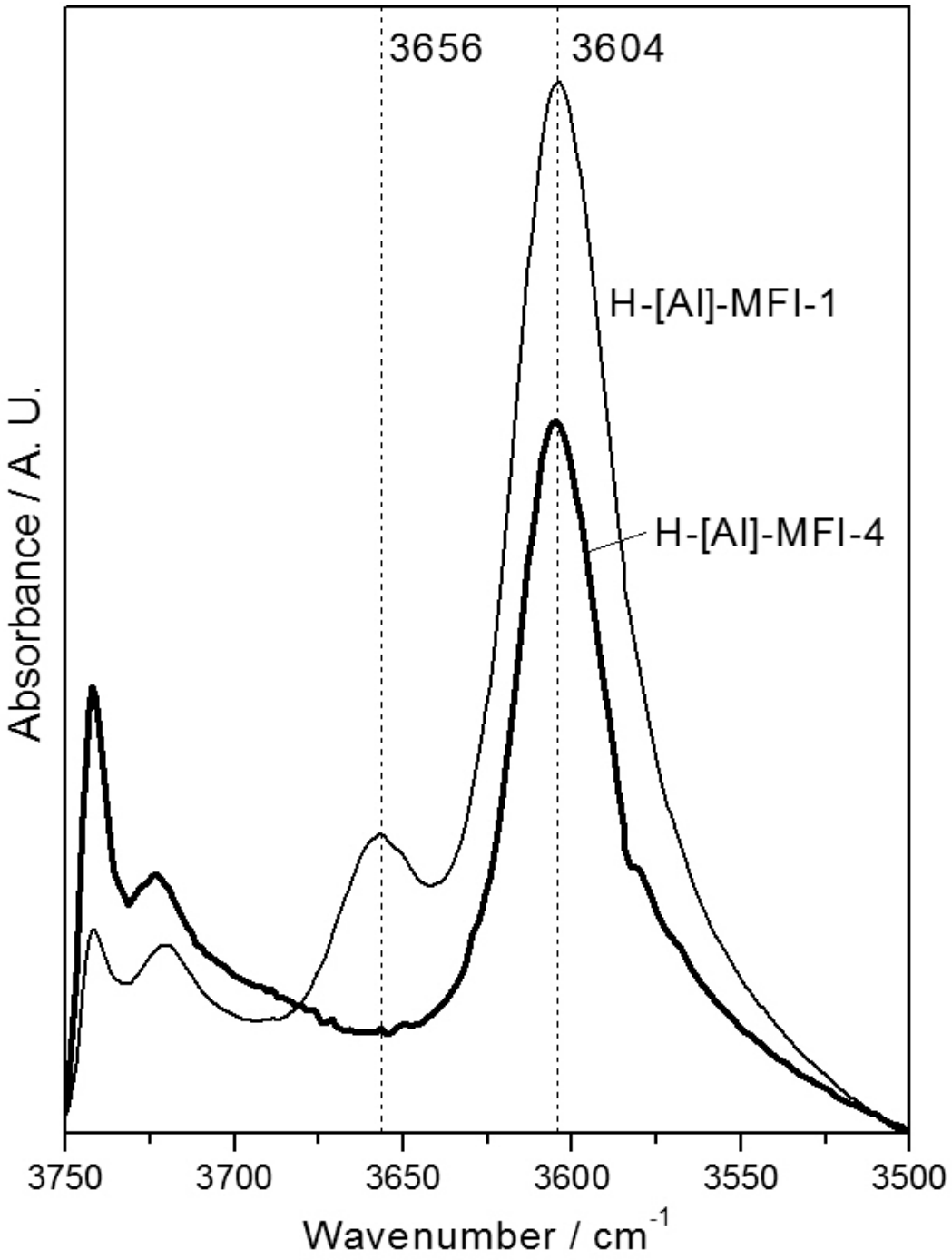

Fig. 9. Infrared spectra of H-[Al]-MFI-1 (thin line) and H-[Al]-MFI-4 (thick line) under dynamic vacuum at 433 K.

References

[1] J. Čejka, G. Centi, J. Perez-Pariente, and W.J. Roth, Catal. Today 179 (2012) 2-15.
[2] A. Corma, Chem. Rev. 95 (1995) 559-614.
[3] J. Čejka, A. Corma, and S. Zones, Zeolites and Catalysis: Synthesis, Reactions and Applications. John Wiley & Sons, 2010.
[4] H.V. Bekkum, Introduction to Zeolite Science and Practice. Elsevier, 2001.
[5] A. Chatterjee, T. Iwasaki, T. Ebina, and A. Miyamoto, Micropor. Mesopor. Mater. 21 (1998) 421-428.
[6] R. Zahradnik, P. Hobza, B. Wichterlova, and J. Cejka, Collect. Czech. Chem. Commun. 58 (1993) 2474-2488.
[7] P. Strodel, K.M. Neyman, H. Knözinger, and N. Rösch, Chem. Phys. Lett. 240 (1995) 547-552.
[8] S.P. Yuan, J.G. Wang, Y.W. Li, and H. Jiao, The Journal of Physical Chemistry A 106 (2002) 8167-8172.
[9] S. Jungsuttiwong, J. Lomratsiri, and J. Limtrakul, Int. J. Quantum Chem. 111 (2011) 2275-2282.
[10] H.V. Brand, L.A. Curtiss, and L.E. Iton, J. Phys. Chem. 97 (1993) 12773-12782.
[11] H.V. Brand, L.A. Curtiss, and L.E. Iton, J. Phys. Chem. 96 (1992) 7725-7732.
[12] D.J. Parrillo, and R.J. Gorte, J. Phys. Chem. 97 (1993) 8786-8792.
[13] S.M. Babitz, B.A. Williams, J.T. Miller, R.Q. Snurr, W.O. Haag, and H.H. Kung, Appl. Catal., A 179 (1999) 71-86.
[14] W.F. Kladnig, J. Phys. Chem. 83 (1979) 765-766.
[15] A.I. Biaglow, R.J. Gorte, G.T. Kokotailo, and D. White, J. Catal. 148 (1994) 779-786.
[16] J.A. Lercher, C. Grundling, and G. EderMirth, Catal. Today 27 (1996) 353-376.
[17] R.J. Gorte, Catal. Lett. 62 (1999) 1-13.
[18] D.J. Parrillo, C. Lee, R.J. Gorte, D. White, and W.E. Farneth, The Journal of Physical Chemistry 99 (1995) 8745-8749.
[19] R.T. Carr, M. Neurock, and E. Iglesia, J. Catal. 278 (2011) 78-93.
[20] D.W. Fickel, A.M. Shough, D.J. Doren, and R.F. Lobo, Micropor. Mesopor. Mater. 129 (2010) 156-163.
[21] W.E. Stewart, and M. Caracotsios, Athena Visual Studio, v. 14.2, (2010).
[22] J.D. Chai, and M. Head-Gordon, PCCP 10 (2008) 6615-6620.
[23] M.J. Frisch, G.W. Trucks, H.B. Schlegel, G.E. Scuseria, M.A. Robb, J.R. Cheeseman, G. Scalmani, V. Barone, B. Mennucci, G.A. Petersson, H. Nakatsuji, M. Caricato, X. Li, H.P. Hratchian, A.F. Izmaylov, J. Bloino, G. Zheng, J.L. Sonnenberg, M. Hada, M. Ehara, K. Toyota, R. Fukuda, J. Hasegawa, M. Ishida, T. Nakajima, Y. Honda, O. Kitao, H. Nakai, T. Vreven, J.A. Montgomery, J.E. Peralta, F. Ogliaro, M. Bearpark, J.J. Heyd, E. Brothers, K.N. Kudin, V.N. Staroverov, R. Kobayashi, J. Normand, K. Raghavachari, A. Rendell, J.C. Burant, S.S. Iyengar, J. Tomasi, M. Cossi, N. Rega, J.M. Millam, M. Klene, J.E. Knox, J.B. Cross, V. Bakken, C. Adamo, J. Jaramillo, R. Gomperts, R.E. Stratmann, O. Yazyev, A.J. Austin, R. Cammi, C. Pomelli, J.W. Ochterski, R.L. Martin, K. Morokuma, V.G. Zakrzewski, G.A. Voth, P. Salvador, J.J. Dannenberg, S. Dapprich, A.D. Daniels, Farkas, J.B. Foresman, J.V. Ortiz, J. Cioslowski, and D.J. Fox. 2009. Gaussian 09, Revision C.01. Wallingford CT.
[24] D.H. Olson, G.T. Kokotailo, S.L. Lawton, and W.M. Meier, J. Phys. Chem. 85 (1981) 2238-2243.
[25] S. Svelle, C. Tuma, X. Rozanska, T. Kerber, and J. Sauer, J. Am. Chem. Soc. 131 (2009) 816-825.
[26] J. Sauer, in: G. Pacchioni, P. Bagus, and F. Parmigiani, (Eds.), Cluster Models for Surface and Bulk Phenomena, Plenum Press, New York.
[27] J. Gomes, P.M. Zimmerman, M. Head-Gordon, and A.T. Bell, J. Phys. Chem. C 116 (2012) 15406-15414.
[28] H. Bludau, H.G. Karge, and W. Niessen, Microporous Mesoporous Mat. 22 (1998) 297-308.

[29] E. C.A, J. Catal. 141 (1993) 347-354.
[30] C.D. Baertsch, K.T. Komala, Y.H. Chua, and E. Iglesia, J. Catal. 205 (2002) 44-57.
[31] B.H. Wouters, T.H. Chen, and P.J. Grobet, J. Am. Chem. Soc. 120 (1998) 11419-11425.
[32] J.A. van Bokhoven, and N. Danilina, Zeolites and Catalysis, Wiley-VCH Verlag GmbH & Co. KGaA. 283-300.
[33] B. Xu, F. Rotunno, S. Bordiga, R. Prins, and J.A. van Bokhoven, J. Catal. 241 (2006) 66-73.
[34] R. Gounder, A.J. Jones, R.T. Carr, and E. Iglesia, J. Catal. 286 (2012) 214-223.
[35] A.M. Rigby, G.J. Kramer, and R.A. vanSanten, J. Catal. 170 (1997) 1-10.
[36] L. Grajciar, C.O. Arean, A. Pulido, and P. Nachtigall, PCCP 12 (2010) 1497-1506.
[37] C. Lo, and B.L. Trout, J. Catal. 227 (2004) 77-89.
[38] M. Brandle, and J. Sauer, J. Am. Chem. Soc. 120 (1998) 1556-1570.
[39] U. Eichler, M. Brandle, and J. Sauer, J. Phys. Chem. B 101 (1997) 10035-10050.
[40] P.G. Moses, and J.K. Norskov, ACS Catal. 3 (2013) 735-745.
[41] M. Leslie, and M.J. Gillan, Journal of Physics C-Solid State Physics 18 (1985) 973-982.
[42] C. Freysoldt, J. Neugebauer, and C.G. Van de Walle, Phys. Rev. Lett. 102 (2009).
[43] R. Shannon, Acta Crystallographica Section A 32 (1976) 751-767.
[44] R.G. Pearson, Inorg. Chem. 27 (1988) 734-740.
[45] J. Macht, R.T. Carr, and E. Iglesia, J. Catal. 264 (2009) 54-66.
[46] W. Tang, E. Sanville, and G. Henkelman, J. Phys.-Condes. Matter 21 (2009).
[47] R. Pophale, P.A. Cheeseman, and M.W. Deem, PCCP 13 (2011) 12407-12412.
[48] S.R. Blaszkowski, and R.A. vanSanten, J. Phys. Chem. B 101 (1997) 2292-2305.
[49] S.R. Blaszkowski, and R.A. vanSanten, J. Am. Chem. Soc. 118 (1996) 5152-5153.
[50] A. Zecchina, S. Bordiga, G. Spoto, D. Scarano, G. Spano, and F. Geobaldo, Journal of the Chemical Society-Faraday Transactions 92 (1996) 4863-4875.
[51] R. Gounder, and E. Iglesia, Chem. Commun. 49 (2013) 3491-3509.
[52] M.J. Janik, J. Macht, E. Iglesia, and M. Neurock, The Journal of Physical Chemistry C 113 (2009) 1872-1885.
[53] C.C. Lee, R.J. Gorte, and W.E. Farneth, The Journal of Physical Chemistry B 101 (1997) 3811-3817.
[54] E.G. Derouane, J. Catal. 100 (1986) 541-544.
[55] R. Gounder, and E. Iglesia, Acc. Chem. Res. 45 (2012) 229-238.
[56] D. Barthomeuf, Mater. Chem. Phys. 17 (1987) 49-71.
[57] A. Corma, Current Opinion in Solid State & Materials Science 2 (1997) 63-75.
[58] C. Baerlocher, and L.B. McCusker. Database of Zeolite Structures.
[59] M.D. Foster, I. Rivin, M.M.J. Treacy, and O.D. Friedrichs, Micropor. Mesopor. Mater. 90 (2006) 32-38.
[60] S. Sklenak, J. Dedecek, C. Li, B. Wichterlova, V. Gabova, M. Sierka, and J. Sauer, PCCP 11 (2009) 1237-1247.
[61] G. Sastre, V. Fornes, and A. Corma, J. Phys. Chem. B 106 (2002) 701-708.
[62] C.W. Kim, N.H. Heo, and K. Seff, The Journal of Physical Chemistry C 115 (2011) 24823-24838.
[63] D.H. Olson, N. Khosrovani, A.W. Peters, and B.H. Toby, J. Phys. Chem. B 104 (2000) 4844-4848.
[64] J. Dědeček, Z. Sobalík, and B. Wichterlová, Catalysis Reviews 54 (2012) 135-223.
[65] B.F. Mentzen, and G. Bergeret, J. Phys. Chem. C 111 (2007) 12512-12516.
[66] F. Eder, M. Stockenhuber, and J.A. Lercher, The Journal of Physical Chemistry B 101 (1997) 5414-5419.
[67] R. Gounder, and E. Iglesia, J. Am. Chem. Soc. 131 (2009) 1958-1971.
[68] B.A. De Moor, M.F. Reyniers, O.C. Gobin, J.A. Lercher, and G.B. Marin, J. Phys. Chem. C 115 (2011) 1204-1219.

CHAPTER FOUR

The Strength of Acid Sites in Zeolites and their Consequences for Adsorption and Catalysis

The diverse reactivity of zeolites for catalysis is often non-rigorously attributed to differences in the strength of their acid sites by comparison with the adsorption enthalpies of bases.[1-4] Brønsted acid strength is defined as the deprotonation energy (DPE), or the energy required to heterolytically cleave the H-O bond and separate the resulting proton and anion to a distance of negligible interaction,

$$DPE = E_{Z^-} + E_{H^+} - E_{ZH} \,. \tag{1}$$

DPE values of zeolites are not directly accessible to experiments, however, density functional theory (DFT) calculations show that DPE values differ from 1171 to 1200 kJ mol^{-1} at particular Al-O(H)-Si bridging positions in zeolites (FAU, CHA, MOR and MFI).[5] Yet, CH_3OH dehydration rate constants measured on a variety of zeolite frameworks (FAU, SFH, BEA, MOR, MFI, and CHA) increase systematically with the increasing confinement of transition states and not the density of acid sites indicating acid strength differences are negligible for catalysis.[3, 6] These rate constants do not reflect DPE differences calculated from theory, in part, because rate constants reflect the potential energy surface of transition states and reactive intermediates at all accessible acid sites in zeolites, while DFT-derived DPE values are calculated for individual acid sites. In this work we reconcile these findings by calculating DPE values at all crystallographically unique sites in MFI, BEA, MOR, CHA, FAU and FER, and by appropriately averaging the resulting values to reflect the averaged stability also of transition states. The results shed light on the nature of acid strength in solid acids and their consequences for reactivity and the stability of adsorbed species.

DFT-derived (RPBE/PAW) DPE values of MFI and BEA with Al and protons in all crystallographically distinct configurations and one Al-atom per u.c. are shown in Figure 1 (DPE values of all sites in MOR, FAU, CHA and FER in SI). DPE values differ by <47 and <31 kJ mol^{-1} depending on the location of the Al-atom and proton in MFI and BEA, respectively (Figure 1). The proton environment and the Al-location determine DPE values in MFI; the substitution of Si at the T8 position (numbering according to convention[7]) with Al leads to DPE values that differ as much as 36 kJ mol^{-1} depending on whether the proton is located at the O7 (Al8-O7(H)-Si7) or O12 (Al8-O12(H)-Si12) atom. Al at T12 (Al12-O12(H)-Si8) leads to DPE values 24 kJ mol^{-1} larger than if Al occupies T8 (Al8-O12(H)-Si12) with the proton at the same O-atom. We conclude that DPE values depend sensitively on subtle differences in the locations of both protons and Al-atoms in the framework.

Next, we investigate the subtle changes in the zeolite framework that may give rise to the range in DPE values. Si-O-Al bond angles at Si-O(H)-Al bridging structures increase from 126° to 144°, but do not correlate with DPE differences (Figure 2) as concluded on FAU and MFI at a select number of acid sites.[8] The smallest DPE values (<1640 kJ mol^{-1}) are only found on structures with large (>135°) bond angles, however, these bond angles can also lead to larger DPE values. The insensitivity of DPE values to changes in bond angles and thus changes in the hybridization of the O-atom suggests that the O-H bond has a significant ionic character

supported by the positive Bader charge of the proton in MFI clusters (+0.7 e).[3] DPE values also do not correlate with O-H bond distances, ν(OH) stretching frequencies, or the location of T-atoms in any discernible manner indicating these are inappropriate surrogates of acid strength (SI).

Protons contained in smaller voids are closer to more framework O-atoms and can form stabilizing H-bonds. These stabilizing interactions increase O-H bond distances (SI) and may also influence DPE values. Yet, no clear correlations of DPE are found with metrics of these H-bonding interactions, O-H bond distances, Si-O-Al bond angles, and ν(OH) frequencies (SI) indicating DPE values cannot be determined from one simple metric and likely depend on a combination of these factors and non-local interactions; these non-local interactions may include ring strain and electrostatic interactions between framework O dipoles and the proton.

NH_3 adsorption electronic energies calculated with DFT (PBE-D2/PAW) at various proton (and Al) positions in MFI varied by 35 kJ mol^{-1} (130 – 165 kJ mol^{-1}) and do not correlate with DPE values of the protons where NH_3 molecules were placed before DFT optimizations (Figure 4), nor with maximum DPE values of protons at a given Al-site (SI). NH_3 adsorption enthalpies measured by microcalorimetry on MFI (150 kJ mol^{-1}; 480 K) are within calculated values, but do not depend on coverage below stoichiometric adsorption concentrations.[9] The range of calculated energies is not reflected in these measurements because adsorption measurements reflect temperature-dependent averages (discussed below) of adsorption events that do not necessarily reflect the isolated adsorption structures in DFT calculations. NH_3 adsorption enthalpies also do not detect 10 kJ mol^{-1} changes in DPE from the substitution of Al heteroatoms with Fe in MFI.[3, 10] The insensitivity of NH_3 adsorption enthalpies to DPE reflect the strong interaction energies of NH_4^+ cations with the anionic framework that recover most of the energy required to deprotonate the zeolite.[3, 11] Large differences in calculated NH_3 adsorption energies, instead reflect the quantity and strength of H-bonding interactions of the NH_4^+ cation with framework O-atoms. These results underscore the inadequacies of NH_3 adsorption enthalpies for acid strength detection. The correlation of NH_3 adsorption energies with reaction energies in some cases, e.g. propene methylation rates,[12] reflect instead van der Waals and H-bonding interactions and are relevant only when these interactions reproduce those of transition states.[6, 13]

The relationship between DPE values and measured activation barriers to form ion-pair transition states from gas-phase reactants in acid catalyzed reactions is illustrated by a Born-Haber thermochemical cycle (Scheme 1). In this hypothetical cycle, the reactant, R, is protonated in the gas-phase to form the gas-phase transition state analog, RH^+, which is then stabilized by the zeolite to form the transition state.

Brønsted acid sites in zeolites created by the charge imbalance of an Al heteroatom are bound to O-atoms at Al-O-Si bridges (Scheme 2); infrared spectra of FAU during pyridine titrations indicate that protons migrate across all four O-atoms connected to the same Al-atom at moderate temperatures (298 K).[14] The mobility of protons at catalytically relevant temperatures, the quasi-equilibrated adsorption of gas-phase reactants and their equilibrium with transition states in transition state theory formalisms lead to an equilibrated pool of transition states at a given Al-atom,

$$\left[TS_1\right] \underset{}{\overset{K_i}{\rightleftharpoons}} \left[TS_i\right]. \tag{2}$$

The total measured rate at an Al-site, r_{Al}, is given by the sum of the transmission frequencies, ν, multiplied by the concentration of the transition state at each microstate, i:

$$r_{Al} = \sum_{i=1}^{N} r_i = \sum_{i=1}^{N} \upsilon\left[TS_i\right]. \tag{3}$$

The equilibration of transition states with gas-phase reactants lead to the following expression that relates an average measured activation free energy, $\left\langle \Delta G^{\ddagger} \right\rangle$, to the activation free energies to form transition states at each microstate:

$$\frac{k_B T}{h} e^{\frac{-\left\langle \Delta G^{\ddagger} \right\rangle}{k_B T}} \prod_j a_j^{\nu_j} = \sum_{i=1}^{N} \frac{k_B T}{h} e^{\frac{-\Delta G_i^{\ddagger}}{k_B T}} \prod_j a_j^{\nu_j} \ . \tag{4}$$

These treatments approach the ensemble sampling of the entire potential energy surface when the number of microstates, N, is large and are analogous to molecular dynamics methods. The activities rigorously cancel from both sides of Eq. (4) because they refer to the same gas-phase reactants and Eq. (4) simplifies to

$$e^{\frac{-\left\langle \Delta G^{\ddagger} \right\rangle}{k_B T}} = \sum_{i=1}^{N} e^{\frac{-\Delta G_i^{\ddagger}}{k_B T}} \ . \tag{5}$$

Eq. (5) gives the measured free energy activation barrier $\left\langle \Delta G^{\ddagger} \right\rangle$ in terms of the barriers at each microstate (e.g. each unique transition state position at an Al-atom). The measured enthalpy is related to the free energy from the Van't Hoff equation,

$$\frac{\partial \ln\left(\left\langle K^{\ddagger} \right\rangle\right)}{\partial T^{-1}} = \frac{\partial \left\langle \Delta G^{\ddagger} \right\rangle}{\partial T^{-1}} = -\frac{\left\langle \Delta H^{\ddagger} \right\rangle}{k_B}. \tag{6}$$

Combining Eq. (5) with Eq. (6), we obtain an equation for the measured enthalpic barrier of a reaction,

$$-\left\langle \Delta H^{\ddagger} \right\rangle = \frac{\sum_{i=1}^{N} \left[-\Delta H_i^{\ddagger} \exp\left(\frac{-\Delta G_i^{\ddagger}}{k_B T} \right) \right]}{\sum_{i=1}^{N} \exp\left(\frac{-\Delta G_i^{\ddagger}}{k_B T} \right)}. \tag{7}$$

Measured activation enthalpies, $\left\langle \Delta H^{\ddagger} \right\rangle$, reflect the enthalpy difference of equilibrated transition states (<TS>; Scheme 1) with an equilibrated pool of reactants or reactive intermediates (e.g. gas-phase reactants and an equilibrated pool of zeolite protons, <ZH>; Scheme 2). The reactivity of a zeolite, therefore, depends on DPE values that reflect the stability of the equilibrated pool of protons, determined from Eq. (8),

$$\left\langle DPE \right\rangle = E_{Z^-} + E_{H^+} - \left\langle E_{ZH} \right\rangle, \quad (8)$$

where $<E_{ZH}>$ is calculated from Eq. (7) and the energies of the four proton microstates corresponding to an Al-atom (Scheme 2).

<DPE> values are shown in Figure 1 calculated at the 12 and 8 unique Al-substitution sites in MFI and BEA. <DPE> values are similar (within 13 kJ mol^{-1}) regardless of the Al-atom location on MFI, BEA, MOR, FER, FAU, and CHA zeolites (MOR, FER, FAU and CHA in SI). Increasing the force criterion during geometry optimizations decreases differences in <DPE> (details in SI) implying that <DPE> differences reflect inaccuracies in DFT methods and not intrinsic differences in <DPE>. The similarity of <DPE> values in MFI is consistent with CH_3OH dehydration rate constants that depend on acid strength, which are also similar on Al-MFI samples with varying Al density (0.8-5.5 Al/u.c.).[3] We conclude that acid strength differences reflected in measured activation barriers (<DPE>) are negligible because of the equilibration of transition states and reactive intermediates in different microstates at Al-atoms. Structural changes, which did not influence the acid strength of isolated protons (DPE) in any monotonic manner, also do not affect the temperature averaged acid strength at each Al-atom (<DPE>).

DPE values calculated with periodic-DFT lead to <DPE> values that are similar regardless of the environment of the Al-atom, yet <DPE> values are up to 96 kJ mol^{-1} larger on MFI than BEA zeolites and ~400 kJ mol^{-1} larger than DPE values estimated with DFT cluster models[3] and QM-Pot.[5, 8] The differences in <DPE> between zeolites are inconsistent with <DPE> values that are independent of Al-atom location in a given zeolite, because heteroatom location differences simulate the structural differences of Al-atoms in other frameworks. The differences appear to reflect artifacts in periodic-DFT treatments of charged unit cells due to spurious interactions of charges between neighboring cells and an ill-defined potential.[15, 16]

DFT calculations of DPE at all crystallographically unique positions in MFI, BEA, MOR, FER, FAU and CHA indicate that DPE values depend sensitively on the environment of the proton, but are not described rigorously by any one metric. Average DPE values (<DPE>) that reflect the temperature-averaged equilibration of protons analogous to those averages for transition states in measured rates, however, are similar and independent of Al-atom position. Similar <DPE> values are consistent with CH_3OH dehydration rate constants that indicate catalytically-relevant acid strength differences are negligible.[6] DFT calculations that attempt to compare transition state and reactive intermediate enthalpies with measured barriers, therefore, should appropriately average the energy of equilibrated reactive intermediates and transition states, or, as an approximation, reference calculations to the most stable transition states and

reactants to estimate temperature-averaged structures. The most stable protons at each Al-atom in MFI, BEA, MOR, FER, FAU and CHA are provided in the SI as a reference.

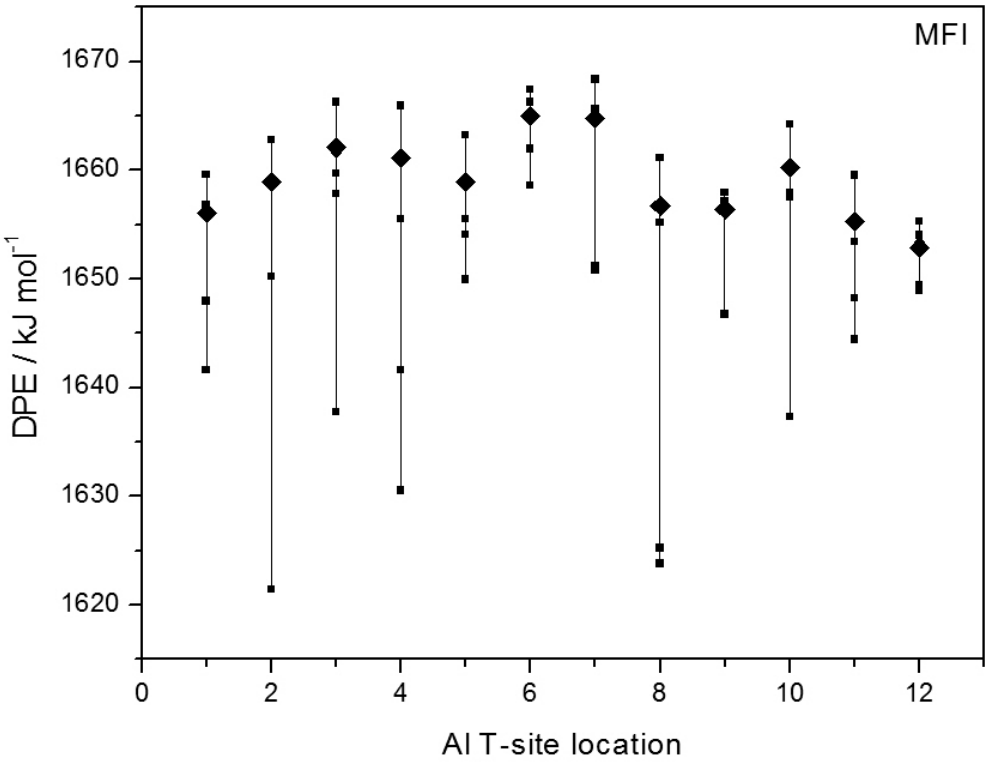

(a)

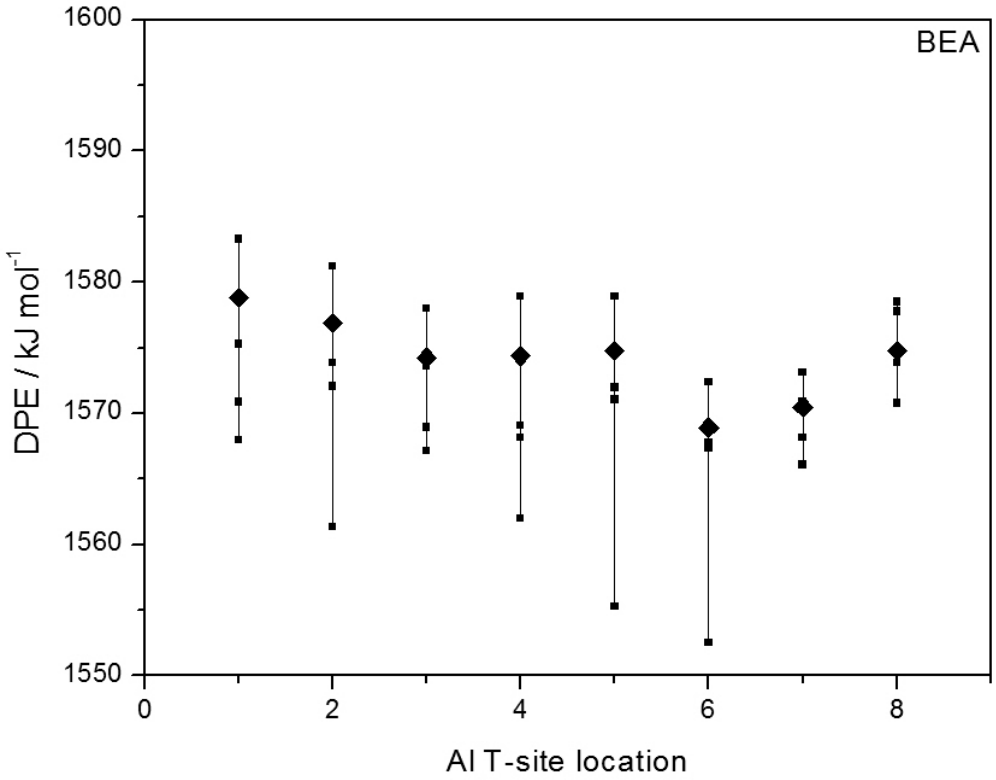

(b)

Fig. 1. DPE values of zeolites (■) with protons and Al at all crystallographically unique positions in (a) MFI and (b) BEA calculated with DFT at the RPBE/PAW level and DPE averages (◆) calculated with Eq. (7) and (8).

Scheme 1. Thermochemical cycle of an acid catalyzed activation of R in a zeolite depicting the energy levels of various equilibrated protons (ZH) and transition states (TS) and their averages (<ZH> and <TS>) reflected in activation barriers $\langle E_a^{\ddagger} \rangle$ and their relationship with deprotonation energies (DPE), proton affinities (E_{pa}) and stabilization energies (E_{stab}).

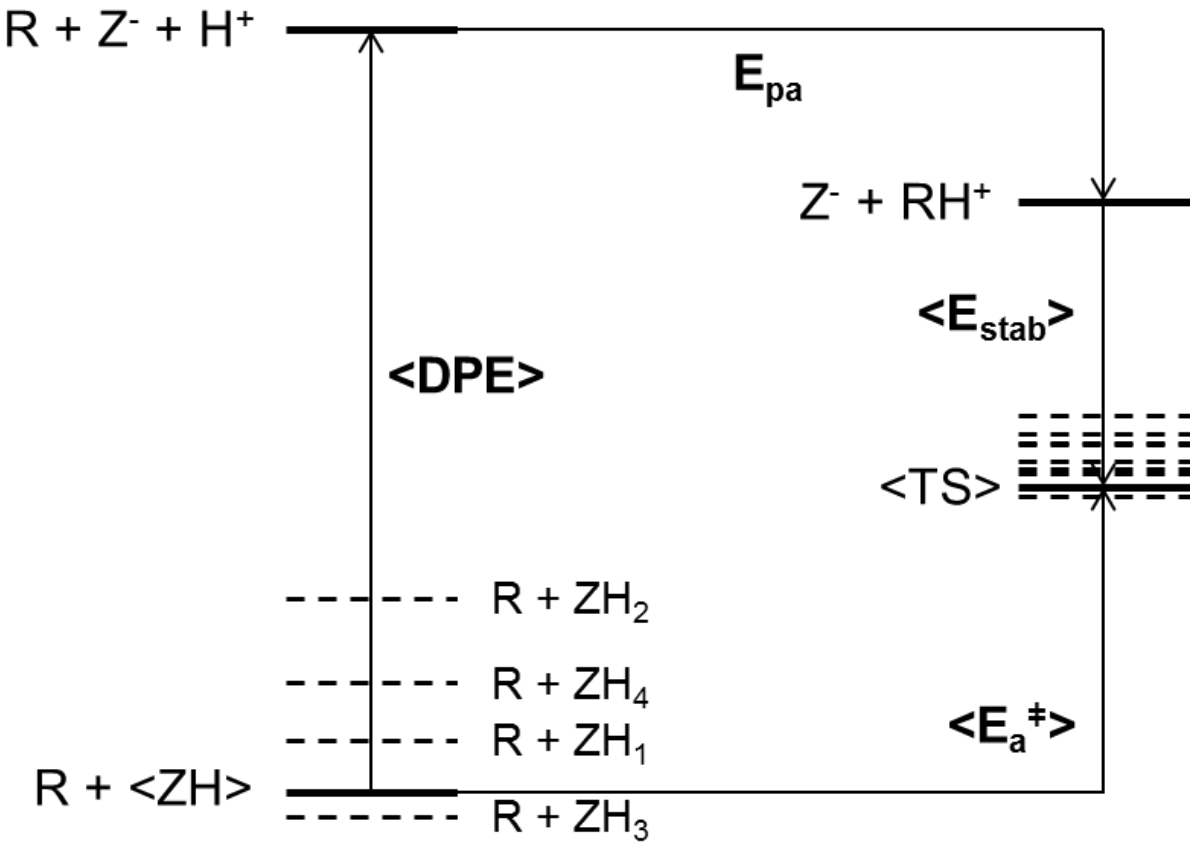

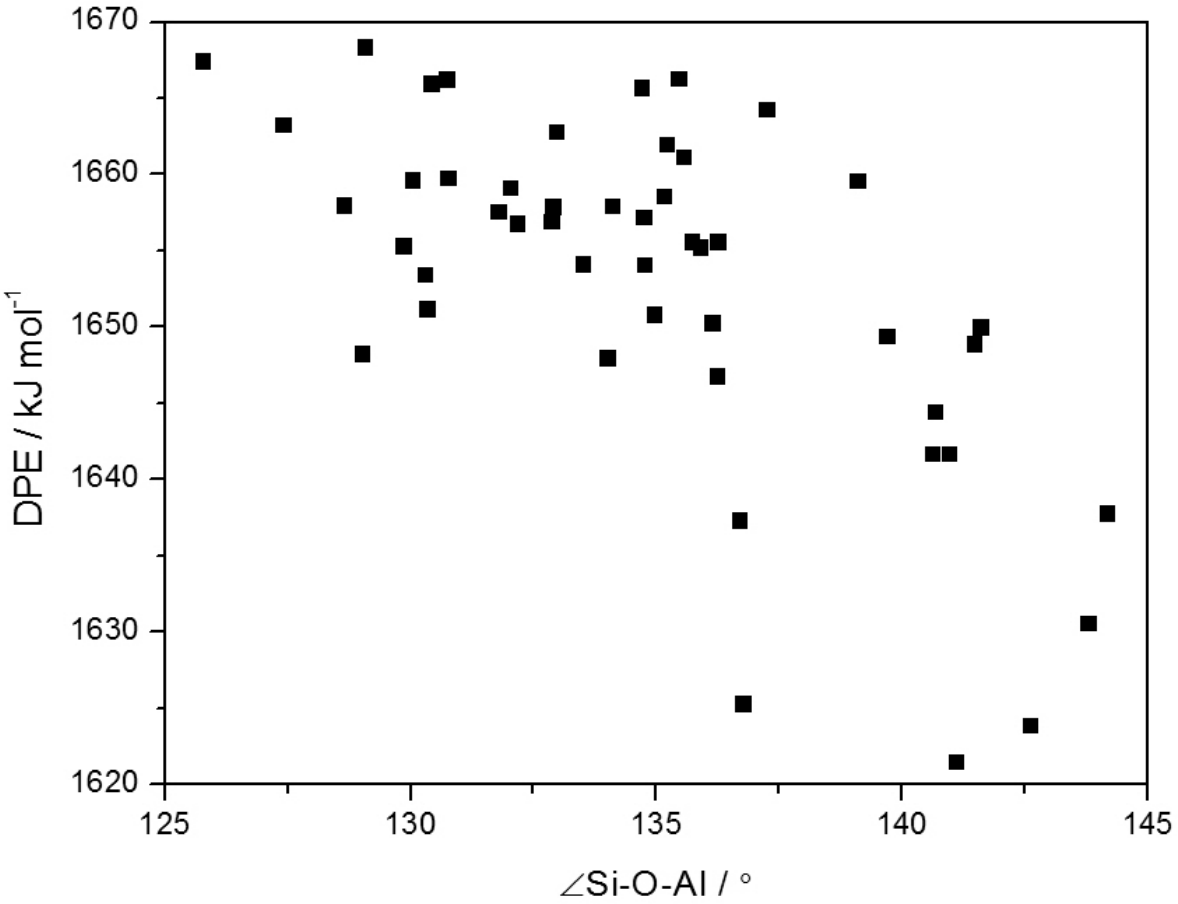

Fig. 2. DPE values as a function of the Si-O-Al bond angle at the Si-O(H)-Al bridge in MFI calculated at the RPBE/PAW level of theory.

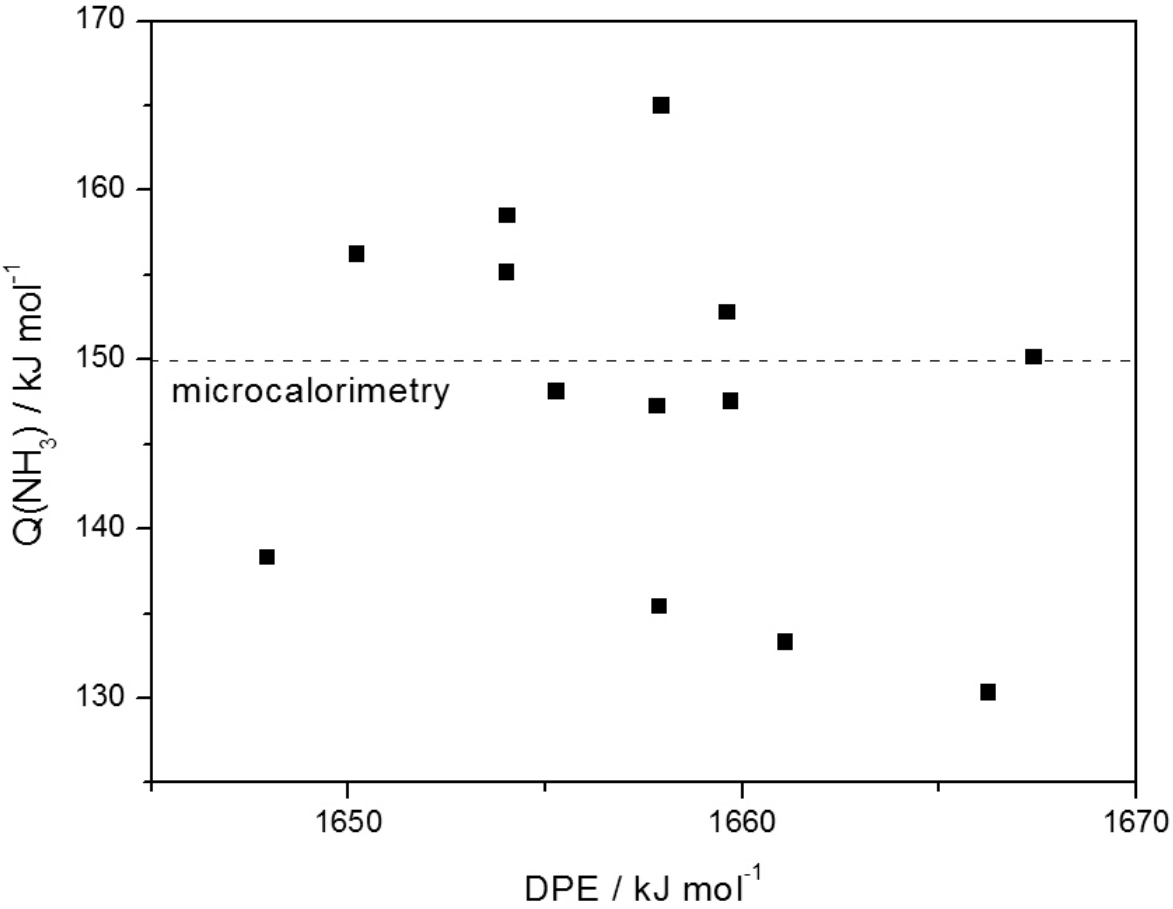

Fig. 3. NH_3 adsorption energies at various proton and Al locations calculated with DFT (PBED2/PAW) on H-MFI as a function of their DPE values calculated (RPBE/PAW). Dotted line represent adsorption enthalpies in MFI (microcalorimetry, 460 K).[9]

Scheme 2. Schematic of zeolite proton energies and deprotonation energies as a function of proton location at a given Al T-site and the energy of their resonance structure.

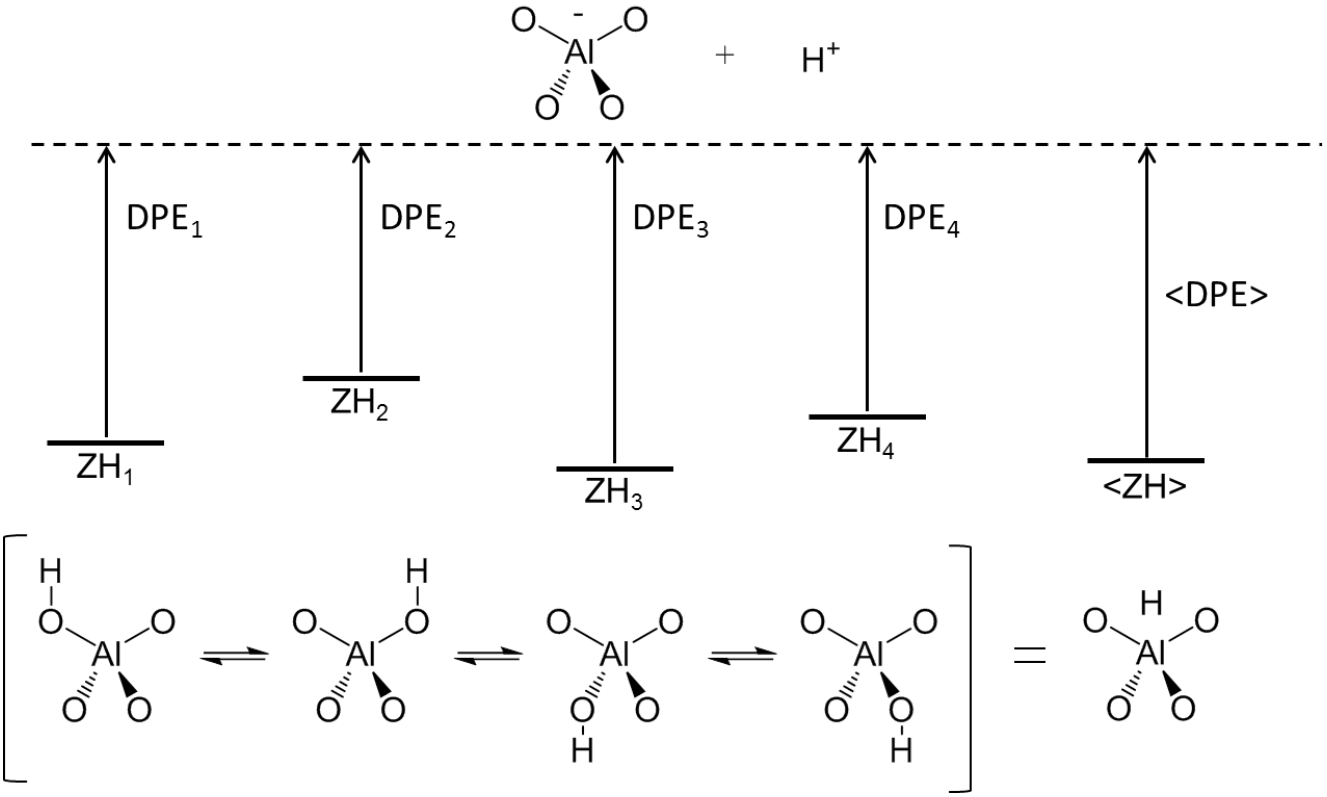

References

[1] A. Corma, Chem. Rev. 95 (1995) 559-614.
[2] R.J. Gorte, Catal. Lett. 62 (1999) 1-13.
[3] A.J. Jones, R.T. Carr, S.I. Zones, and E. Iglesia, J. Catal. 312 (2014) 58-68.
[4] W.E. Farneth, and R.J. Gorte, Chem. Rev. 95 (1995) 615-635.
[5] M. Brandle, and J. Sauer, J. Am. Chem. Soc. 120 (1998) 1556-1570.
[6] A.J. Jones, S. Zones, and E. Iglesia, J. Am. Chem. Soc. submitted (2014).
[7] D.H. Olson, G.T. Kokotailo, S.L. Lawton, and W.M. Meier, J. Phys. Chem. 85 (1981) 2238-2243.
[8] U. Eichler, M. Brandle, and J. Sauer, J. Phys. Chem. B 101 (1997) 10035-10050.
[9] D.J. Parrillo, and R.J. Gorte, J. Phys. Chem. 97 (1993) 8786-8792.
[10] D.J. Parrillo, C. Lee, R.J. Gorte, D. White, and W.E. Farneth, The Journal of Physical Chemistry 99 (1995) 8745-8749.
[11] M.J. Janik, R.J. Davis, and M. Neurock, Catal. Today 105 (2005) 134-143.
[12] C.-M. Wang, R.Y. Brogaard, B.M. Weckhuysen, J.K. Nørskov, and F. Studt, The Journal of Physical Chemistry Letters 5 (2014) 1516-1521.
[13] R. Gounder, and E. Iglesia, Chem. Commun. 49 (2013) 3491-3509.
[14] R. Gounder, A.J. Jones, R.T. Carr, and E. Iglesia, J. Catal. 286 (2012) 214-223.
[15] C. Freysoldt, J. Neugebauer, and C.G. Van de Walle, Phys. Rev. Lett. 102 (2009).
[16] L. Grajciar, C.O. Arean, A. Pulido, and P. Nachtigall, PCCP 12 (2010) 1497-1506.

CHAPTER FIVE

Implications of Transition State Confinement within Small Voids for Acid Catalysis

Abstract

The catalytic diversity of microporous aluminosilicates reflects their unique ability to confine transition states within intracrystalline voids of molecular dimensions and the number (but not the strength) of the protons that act as Brønsted acids. First-order rate constants for CH_3OH conversion to dimethyl ether reflect the energy of transition states relative to those for gaseous and H-bonded CH_3OH molecules; on zeolites, these constants depend exponentially on n-hexane physisorption energies for different void size and shape and proton location, indicating that van der Waals stabilization of transition states causes their different reactivity, without concomitant effects of void structure or proton location on acid strength. The dispersive contribution to adsorption enthalpies of DME, a proxy in shape and size for relevant transition states, was calculated using density functional theory and Lennard-Jones interactions on FAU, SFH, BEA, MOR, MTW, MFI, and MTT zeolites and averaged over all proton locations; first-order rate constants also depended exponentially on these enthalpies. In contrast, zero-order rate constants, which reflect the stability of transition states relative to protonated CH_3OH dimers similar in size, depended weakly on dispersive stabilization, whether measured from experiment or simulations, because dispersive forces influence species similar in size to the same extent. These results, taken together, demonstrate the preeminent effects of confinement on zeolite reactivity and the manner by which the local voids around protons held within diverse intracrystalline environments give rise to the unique behaviors that have made zeolites ubiquitous in the practice of catalysis. Enthalpic stabilization of relevant transition states prevail over entropic losses caused by confinement at low temperatures in a manner reminiscent of how catalytic pockets and solvents do so in catalysis by molecules or enzymes.

1. Introduction

Zeolite catalysts contain microporous voids that solvate transition states and reactive intermediates through van der Waals interactions and, in doing so, influence the catalytic properties of the Brønsted acid sites that reside within such voids.[1, 2] These effects are evident from transition state energies derived from measured activation barriers for monomolecular cracking of C_3-C_6 *n*-alkanes on H-MFI, which decrease monotonically with increasing *n*-alkane chain size (by ~12 kJ mol^{-1} per CH_2 group) as a consequence of van der Waals interactions that preferentially stabilize larger transition states.[2] The functional form of Gibbs free energies causes enthalpic stabilization to prevail over entropy losses caused by confinement at modest temperatures.[3-5] Measured activation barriers for C_3H_8 cracking also decrease as voids become smaller, from H-FAU (165 kJ mol^{-1} [6], ~1.1 nm voids[7]), to H-BEA (156-159 kJ mol^{-1} [6], ~0.6 nm voids[7]) and to H-MFI (147 kJ mol^{-1} [6], ~0.5 nm voids[7]); these trends also indicate that a tighter fit imposed by the smaller voids enthalpically stabilizes C_3H_8 cracking transition states more effectively than larger voids. Yet, C_3H_8 cracking barriers differ markedly among samples with a given framework, when such samples differ in provenance or synthesis history (e.g., 147-167 kJ mol^{-1} for four different H-MOR samples[2]). Also, such barriers do not trend monotonically with void size or with the C_3H_8 adsorption energy within such voids for many

zeolites (H-FAU, H-BEA, H-MOR, H-MFI, H-MWW, H-FER).[2, 6] The origins of such inconsistencies remain unclear, at least in part, because of the uncertain location[8, 9] and strength[10, 11] of Brønsted acid sites and also because of the ubiquitous nature of diffusional artifacts in these microporous solids. Understanding the intrinsic reactivity of zeolites, and solid acids in general, requires structure-function relationships that involve accurate descriptors of acid strength and confinement.

The strength of a Brønsted acid is given by its deprotonation energy (DPE), which is required for heterolytic cleavage of its O-H bonds. DPE values can be estimated from density functional theory (DFT), but they cannot be measured. NH_3 adsorption energies (Q_{NH3}) are often used instead as indirect proxies of acid strength;[10] their values, however, are insensitive to DPE changes expected from the substitution of Al by Fe in MFI (Q_{NH3} = -145 ± 5 kJ mol^{-1} for both H-[Al]-MFI to H-[Fe]-MFI samples,[12] which have DPE values that differ by 16 kJ mol^{-1} [11]). Q_{NH3} values vary from 104-160 kJ mol^{-1} among H-MFI, H-FAU, H-CHA and H-MOR,[13] but these trends are inconsistent with their similar DPE (1171 – 1200 kJ mol^{-1}, QM-Pot[13]), because Q_{NH3} values reflect stabilization by both acid strength *and* solvation (via van der Waals interactions), which are inextricably linked; yet, Q_{NH3} values are often interpreted - non-rigorously and inaccurately - as reflecting solely the strength of Brønsted acid sites. The measurement of acid strength, therefore, requires a systematic method for separating the contributions from acid strength and solvation to the energies of intermediates and transition states in solid acids. These methods must involve a combination of mechanistically-interpreted rate data in terms of two or more rate constants that depend differently on acid strength and solvation effects.

The rate constants for elementary steps become sensitive to acid strength[14] and solvation[1, 2, 15] when they reflect the free energy of carbenium-ion transition states relative to intermediates that differ in charge and size. At low temperatures, enthalpic effects prevail over the entropic losses inherent in confinement and electrostatic stabilization because of the functional form of Gibbs free energies. For instance, the two rate constants in the rate equations for CH_3OH dehydration on Brønsted acids reflect the energy of the transition state that mediates dimethyl ether (DME) formation relative to that of either a protonated CH_3OH dimer (k_{zero}) or a H-bonded CH_3OH and a gaseous CH_3OH molecule (k_{first}) (Scheme 1).[16] The values of these rate constants increase exponentially with decreasing DPE on H-MFI zeolites with different framework heteroatoms[11] and on W-based polyoxometalate clusters with different central atoms;[16] such trends reflect effects of composition on the stability of their respective conjugate bases (reflected in their DPE), which influence, in turn, the stability of the ion-pair transition states more sensitively than that of their relevant precursors. The sensitivity of k_{first} and k_{zero} depend differently on changes in DPE, because of differences in charge of their respective relevant precursors (CH_3OH dimers and H-bonded species, respectively). The k_{first} and k_{zero} values also depend differently on the size of voids that contain the protons, because van der Waals stabilization of DME formation transition states, CH_3OH dimers and H-bonded CH_3OH depends on their respective different sizes.[11, 16, 17] The specific contributions of acid strength and solvation to such rate constants have been reported previously on H-MFI zeolites,[11] but a similar analysis has not yet been applied to other zeolite frameworks to discern the influence of zeolite structure on acid strength and the implications of solvation for these rate constants and for catalytic reactivity more generally.

Here, we report and interpret CH_3OH dehydration rate constants (normalized per accessible proton) on microporous aluminosilicates differing in framework structure and Al and proton density (H-FAU, chemically-dealuminated H-FAU,[18] H-SFH, H-BEA, H-MTW, H-MOR, H-MFI, H-MTT). We relate these intrinsic reactivity measures to measured n-hexane adsorption enthalpies and to van der Waals interaction energies for DME adsorbed at zeolite protons derived from density functional theory (DFT) and from Lennard-Jones force-field estimates. These results provide essential mechanistic insights about how differences in acid strength and solvation among zeolites influence CH_3OH dehydration rate constants and confirm the dominant effects of solvation in the remarkable diversity of zeolites in acid catalysis.

2. Methods

2.1 Catalyst synthesis and characterization

H-MFI samples (Table 1) were prepared according to protocols described previously.[11] H-MCM-41 (Sigma-Adrich, 643653, Si/Al = 29.8), H-FAU (Engelhard, Si/Al = 2.8), NH_4^+-BEA (Zeolyst, Si/Al = 11.8), NH_4^+-MOR-1 (Zeolyst, Si/Al = 10.0), H-MOR-2 (Tosoh, Si/Al = 9.1), NH_4^+-MFI-1 (Zeolyst, Si/Al = 16.6), NH_4^+-MFI-3 (Zeolyst, Si/Al = 29.2), and NH_4^+-MFI-4 (Zeolyst, Si/Al = 43.8) samples were obtained in their H^+ or NH_4^+ forms. Chemically dealuminated H-FAU (H-CD-FAU, Si/Al = 7.5) was prepared according to protocols in the LZ-210 patent to remove extra framework Al moieties.[18, 19] An aqueous $(NH_4)_2SiF_6$ solution (15 L, 99%, 1.5 M, Alfa Aesar) at 323 K was added continuously (at 1.67 g s^{-1}) to a mixture of H-USY (12 kg, Union Carbide, Si/Al = 2.9) and deionized water (36 L) at 348 K while stirring. The resulting slurry was treated to decrease the fluoride content in the samples in 1.8 kg batches by adding aqueous $Al_2(SO_4)_3$ (0.8 L, 0.6 M) and stirring for 24 h at 368 K. The resulting solids were filtered and washed with deionized water (300 g water per 1 g zeolite) to yield NH_4-H-CD-FAU.

H-SFH was prepared by replacing B in B-SSZ-53 by Al. B-SSZ-53 was synthesized from an aqueous suspension of N,N,N-trimethyl-[1-(4-fluorophenyl)cyclopentyl]methyl ammonium hydroxide (3 mmol), NaOH (1.2 mmol, 1 M, EMD Chemicals), $Na_2B_4O_7 \cdot 10H_2O$ (0.16 mmol, Aldrich), deionized water (11.25 g) and amorphous SiO_2 (0.9 g, Cab-o-sil M-5) treated in a rotating sealed Teflon-lined vessel (43/60 Hz, Parr, 23 cm^3) held at 433 K for 288 h in a convection oven (Blue M).[20] The resulting solids were washed with deionized water, dried at 393 K for 1 h, then treated in flowing O_2/N_2 (0.02/0.33 cm^3 g^{-1} s^{-1}, UHP, Praxair) at 823 K (0.02 K s^{-1} to 393 K, hold 2 h, 0.02 K s^{-1} to 823 K, hold 5 h) to remove organic moieties from the voids and yield B-SSZ-53. B was replaced with Al by heating a suspension of B-SSZ-53 (0.40 g), $Al(NO_3)_3 \cdot 9H_2O$ (0.10 g) in deionized water (10 g) at 368 K for 72 h.[21] The solids were washed twice with a 0.02 M HCl solution (50 cm^3), then deionized water (300 g water per 1 g zeolite), and finally treated in ambient air at 298 K for 24 h.

NH_4^+-MTW was synthesized by dissolving $Al(OH)_3$ (0.19 g, 53 % Al_2O_3, Reheis F-2000 dried gel) in a solution of 1,4-bis(1-azoniabicyclo[2,2,2]octane)butyl dibromide (15 mmol in 25 g of water, synthesized according to previous protocols[22]), NaOH (7.7 mmol, 1 M, EMD Chemicals) and deionized water (20 g). SiO_2 (4.5 g, Cab-o-sil M-5) was then added and the resulting gel treated in a sealed Teflon-lined vessel (Parr, 125 cm^3) at 443 K for 132 h without

stirring. The settled solids were collected by filtration, washed with deionized water (300 g water per 1 g zeolite) and treated in flowing dry air (2.5 cm^3 g^{-1} s^{-1}, UHP, Praxair) by heating to 823 K at 0.025 K s^{-1} and holding for 4 h to remove organic residues. The solids were added to an aqueous NH_4NO_3 solution (>98%, Sigma-Aldrich, 1 g zeolite per 300 cm^3 0.1 M solution) while stirring at 353 K for 4 h. The solids were recovered by filtration and the exchange was repeated a total of three times to yield NH_4^+-MTW.

H-MTT was synthesized using reported procedures (Example 1 in ref.[23]) by preparing a solution of N,N'-diisopropyl-imidazolium hydroxide (300 g, 1 M, synthesized according to previous protocols[24]) in deionized water (4500 g) and mixing it with a suspension containing KOH (2400 g, 1 M, Fisher), amorphous SiO_2 (1524 g, 30 wt % SiO_2, Ludox AS-30), colloidal SiO_2/Al_2O_3 (1080 g, 26 wt % SiO_2, 4 wt % Al_2O_3, Nalco 1056) and isobutylamine (150 g, >99 %, Aldrich) within a Hastelloy C-lined autoclave (5 gallon, 1500/60 Hz stirring rate) and mixed for 0.5 h at 298 K. The mixture was subsequently treated by heating at 0.005 K s^{-1} to 443 K and holding for 106 h while stirring (150/60 Hz stirring rate). The solids were collected by filtration and washed with deionized water (300 g water per 1 g zeolite).

Zeolite frameworks were confirmed by X-ray diffraction (XRD; Siemens D-500; Cu-K_α radiation). Si and Al contents were measured by inductively-coupled plasma optical emission spectroscopy (ICP-OES; Galbraith Laboratories) and are reported in Table 1.

2.2 Catalytic measurements

Aggregates crushed and sieved from pressed samples to retain 180-250 μm particles (0.03-0.20 g; adjusted to maintain reactant conversions <5 %) were diluted with SiO_2 (Cab-o-sil HS-5, washed with 1.0 M HNO_3, 180-250 μm aggregates, 0.2-0.5 g) and held onto a coarse quartz frit within a tubular quartz reactor (7.0 mm i.d.). The bed temperature was measured with a K-type thermocouple held in contact with the outer tube surface at the bed axial mid-point and kept constant using a three-zone resistively-heated furnace (Applied Test Systems Series 3210) and Watlow controllers (EZ-ZONE PM Series).

All samples were treated in flowing 5% O_2/He (83.3 cm^3 g^{-1} s^{-1}, 99.999%, Praxair) by heating to 773 K at 0.025 K s^{-1}, holding at 773 K for 2 h, and then cooling to 433 K before catalytic measurements. Liquid CH_3OH (99.8%, Sigma-Aldrich) was introduced into flowing He (99.999%, Praxair) through heated lines (>373 K) using a syringe pump (Cole-Palmer 780200C series). Reactant, product, and titrant concentrations were measured by gas chromatography (Agilent 6890N GC) using a DB-Wax capillary column (0.320 mm ID x 30 m x 0.50 μm film; J&W Scientific) and flame ionization or mass spectrometric detection (MKS Spectra Minilab). Dimethyl ether and water were the only products detected at the conditions of these experiments.

2.3 Titration of acid sites by bases

Brønsted acid site densities were measured using 2,6-di-*tert*-butylpyridine (>97%, Sigma-Aldrich), pyridine (>99.9%, Sigma-Aldrich) and CH_3NH_2 (42.9% in CH_3OH, TCI) by introducing these titrants during CH_3OH dehydration (uptakes shown in Table 1). CH_3OH dehydration turnover rates were first measured without the presence of titrants (1.1 kPa CH_3OH,

433 K) before titrant-CH_3OH mixtures were added using a syringe pump (Cole-Palmer 780200C series). The titrant concentrations in the effluent were measured using the chromatographic protocols described above. The number of protons in each sample was determined from titrant uptakes (assuming a 1:1 titrant:H^+ adsorption stoichiometry).

Brønsted acid site densities were also measured from the evolution of NH_3 from NH_4^+-exchanged samples during their thermal treatment. Samples (H^+ and NH_4^+ form) were treated in flowing dry air (2.5 cm^3 g^{-1} s^{-1}, UHP Praxair; heating to 823 K at 0.025 K s^{-1}, 4 h hold) and cooled to 298 K. The treated samples were transferred in ambient air to solutions of 0.1 M NH_4NO_3 (>98%, Sigma-Aldrich; 1 g zeolite per 300 cm^3 solution) while stirring at 353 K for 4 h to replace H^+ with NH_4^+. The solids were recovered by filtration and the exchange process repeated two more times. After the third exchange and filtering, solids were washed with deionized water (300 g water per 1 g zeolite) and left in contact with ambient air for 12 h. These NH_4^+-exchanged samples (0.05-0.09 g) were placed within the reactor described in Section 2.2 and heated to 923 K at 0.833 K s^{-1} and held for 1 h in a flowing mixture of He (2.5 cm^3 g^{-1} s^{-1}, 99.999%, Praxair) and Ar (0.83 cm^3 g^{-1} s^{-1}, 99.999%, Praxair, used as internal standard). NH_3 concentrations were measured by transferring the effluent flow into a mass spectrometer (MKS Spectra Minilab) through a heated Si-coated stainless steel capillary (420 K, 0.254 mm i.d., 183 cm length) positioned immediately below the samples. The intensities for NH_3 (17, 16 amu), water (18, 17 amu) and Ar (40 amu) ions were acquired every 4 s.

2.4 Infrared assessment of pyridine interactions in zeolites

The interactions of pyridine with Brønsted and Lewis acid sites were determined from the intensity of OH vibrational bands (3400-3800 cm^{-1}) and pyridinium (1545 cm^{-1}) and pyridine-Lewis interaction bands (1455 cm^{-1}) before and after titrant introduction.[25] Infrared spectra were collected using a Nicolet NEXUS 670 spectrometer equipped with a Hg-Cd-Te (MCT) detector in transmission mode using self-supporting wafers (~5-15 mg cm^{-2}) and a quartz vacuum cell with NaCl windows. Spectra were measured in the 4000-400 cm^{-1} range with a 2 cm^{-1} resolution by averaging 64 scans. Samples were treated by heating to 723 K (0.033 K s^{-1}) in dry air (1.67 cm^3 s^{-1}, zero grade, Praxair), holding for 2 h, then cooling to 433 K; samples were subsequently evacuated using a diffusion pump (<0.01 Pa dynamic vacuum; Edwards E02) before collecting spectra. Pyridine (99.8%, Aldrich) was purified of absorbed gases by cooling to 77 K in a closed quartz cell, evacuating, and then heating to 298 K; this procedure was repeated three times. Purified pyridine was introduced to samples held at 433 K by incremental dosing without intervening evacuation. After pyridine saturation, the sample cell was opened to an evacuated closed loop in order to incrementally evacuate the sample. All spectra and integrated areas were normalized by the intensity of the Si-O-Si overtones (2100-1750 cm^{-1}).

2.5 Zeolite models and density functional theory methods

van der Waals interactions of DME adsorbed at protons in zeolites from density functional theory (DFT) were used as proxies for the dispersion forces prevalent at DME transition states. DME structures and energies were determined using plane-wave periodic gradient-corrected DFT methods as implemented in the Vienna ab initio Simulation Package (VASP),[26-29] and a plane-wave energy cutoff of 396 eV. All calculations were carried out using van der Waals

corrections in the vdW-DF2 functional[30] and the rPW86 exchange functional[31] with a plane-wave basis set of the projector-augmented-waves (PAW) method.[32, 33] A (1 x 1 x 1) γ-centered *k*-point mesh was used to sample the first Brillouin zone; larger *k*-point mesh sizes changed adsorption energies by <0.05 eV on BEA, MFI and MTT. All atoms were relaxed until electronic energies varied by $<1 \times 10^{-6}$ eV and the forces on all atoms were <0.05 eV A^{-1}.

H-MFI structures contain straight and sinusoidal 10-MR channels (~0.40 nm ray-averaged diameter[11]) that intersect to form larger ellipsoidal voids (~0.82 nm ray-averaged diameter[11]). Atomic coordinates and unit cell parameters (2.0022 x 1.9899 x 1.3383 nm^3 and $\alpha = \beta = \gamma = 90°$) of orthorhombic MFI (0.32 Al/u.c.) were determined from XRD.[34] The Al12-O20(H)-Si3 and Al7-O17(H)-Si4 Brønsted acid sites (numbered according to convention[35]) were chosen for DME adsorption on MFI because they are located at the intersection and sinusoidal channel voids, respectively. Lattice relaxation (maintaining interaxial lattice angles) of the MFI unit cell containing Al12-O20(H)-Si3 led to a <1% increase in the volume of the unit cell (2.008461 x 1.996122 x 1.342485 nm^3), but led to negligible changes (<3 kJ mol^{-1}) in DME van der Waals interaction energies; thus, XRD lattice constants were used without relaxation for all zeolites.

H-FAU structures contain large supercage voids (1.1 nm largest included sphere diameter,[7] 8 supercages/u.c.) connected by 12-MR windows (0.74 nm[36]). Atomic coordinates and unit cell parameters ($a = b = c = 2.4345$ nm and $\alpha = \beta = \gamma = 90°$) were taken from the *International Zeolite Association (IZA)* site.[36] The Al1-O1(H)-Si1 site (numbered according to convention[36]) was chosen to probe DME adsorption energies because the resulting proton resides in supercage voids.

H-BEA contains straight 12-MR channels (0.56-0.77 nm[36]) which intersect to form voids similar in size to the channels themselves (largest included sphere diameter ~0.66 nm[7]). Atomic coordinates and unit cell parameters (1.26614 x 1.26614 x 2.64016 nm^3 and $\alpha = \beta = \gamma = 90°$) for BEA polymorph A were taken from XRD[37] as reported in Accelrys Materials Studio.[38] The Al2-O7(H)-Si7 site (numbered according to convention[36]) contains a H^+ at the intersection of the two channels and was chosen for these studies.

H-MTT contains one-dimensional 10-MR channels (largest free sphere diameter of 0.50 nm [7]). Atomic coordinates and unit cell parameters (0.501 x 2.152 x 1.113 nm^3 and $\alpha = \beta = \gamma = 90°$) were determined from XRD[39] as reported in Accelrys Materials Studio.[38] The Al3-O6(H)-Si7 site (numbered according to convention[36]) contains a H^+ that resides in the 10-MR channel. A super-cell containing three unit cells along the lattice *a* direction was considered in calculations to minimize interactions between periodic adsorption images.

H-MOR structures contain one-dimensional 12-MR channels (0.65 x 0.70 nm [36]) with 8-MR (0.26 x 0.57 nm[36]) side pockets. Atomic coordinates and unit cell parameters (0.18256 x 0.20534 x 0.07542 nm^3 and $\alpha = \beta = \gamma = 90°$) were obtained from the *IZA* site.[36] Protons were considered in the 12-MR channels at the O1, O4, O5, O7, and O10 (numbered according to convention[36]) positions (see Supporting Information for structure images).

2.6 van der Waals adsorption energies from force field calculations with Lennard-Jones potentials

van der Waals interaction energies for DME adsorbed within zeolite void structures were determined from the distances of DME atoms to framework $O_{zeolite}$-atoms using Lennard-Jones potentials[40, 41] and a custom code described herein. Zeolite structures were obtained from the *IZA* site.[36] The structure and orientation of DME with respect to Si-O(H)-Al moieties in zeolites were determined from DME structures at the Al12-O20(H)-Si3 site in MFI calculated from DFT (Section 2.5). The $O_{DME} - O_{zeolite}$ bond distance and $O_{DME} - O_{zeolite} - Si_{zeolite}$ dihedral angles from this DFT-derived structure were used to place DME at each crystallographically unique $O_{zeolite}$-atom; these DME structures were rotated to optimize van der Waals interactions (discussed below). DME structures and energies at $O_{zeolite}$-atoms inaccessible to a spherical probe with a diameter of 0.325 nm (e.g., CH_4) were discarded; the accessibility of O-atoms to such a probe was determined from Voronoi decompositions of the zeolite void space using Zeo++.[42, 43]

The orientation of DME at each unique $O_{zeolite}$-atom was determined from a non-linear conjugate gradient optimization of van der Waals interaction energies allowing DME structures to rotate around the O_{DME}-atom about three orthogonal axes. This optimization technique, which maintains $O_{DME} - O_{zeolite}$ distances, was chosen because DFT-derived $O_{DME} - O_{zeolite}$ distances were similar for all binding locations and zeolite structures (H-FAU, H-BEA, H-MFI, H-MOR, H-MTT; 0.254 ± 0.002 nm; Section 2.5 and Supporting Information) and because transition states are expected to have similar distances to zeolite anions at different proton sites as the result of their ion-pair nature and the strong energetic penalties of separating charge. Structure rotations were continued until van der Waals energies decreased by $<10^{-8}$ eV degree^{-1}.

Initial DME structures were rotated along the axis normal to the Si-O-Si plane at each $O_{zeolite}$-atom in 36° increments (0°, 36°, 72°, etc.) to ensure that minimum energy structures were found. These DME structures were allowed to rotate and minimize their interaction enthalpies along all three orthogonal axes until van der Waals energies varied by $<10^{-8}$ eV degree^{-1}. The structures with the most stable van der Waals interaction energies at each $O_{zeolite}$-atom in a given zeolite were averaged:

$$< Q_{LJ}(DME) >= k_B T \ln\left(\frac{1}{N_{O-atoms}} \sum_{i=1}^{N_{O-atoms}} e^{\frac{Q_{LJ,i}(DME)}{k_B T}} \right). \quad (1)$$

Where $Q_{LJ,i}(DME)$ is the optimum van der Waals interaction energy of DME at $O_{zeolite}$-atom 'i', $N_{O\text{-}atoms}$ is the number of accessible $O_{zeolite}$-atoms, and T is the reaction temperature.

The average given by Eq. (1) resembles the ensemble (exponential) average of transition state and reactive intermediate energies at different zeolite protons (and thus O-atoms) reflected in the free energies of measured rates and rate constants. Measured reaction rates, $\langle r \rangle$, reflect the sum of the reaction rate at each proton:

$$\frac{\langle r \rangle}{N_{H^+}} = \frac{1}{N_{H^+}} \sum_{i=1}^{N_{H^+}} r_i \ . \tag{2}$$

Transition state theory treatments of thermodynamically non-ideal systems[44] lead to the following reaction rate dependencies on transition state free energies relative to gas-phase reactants:

$$\frac{k_B T}{h} e^{\frac{-\langle \Delta G^{\ddagger} \rangle}{k_B T}} \prod_j a_j^{\nu_j} = \frac{1}{N_{H^+}} \sum_{i=1}^{N_{H^+}} \frac{k_B T}{h} e^{\frac{-\Delta G_i^{\ddagger}}{k_B T}} \prod_j a_j^{\nu_j} \ , \tag{3}$$

where $\Delta G_i^{\ddagger}$ is the free energy difference of the transition state relative to gas-phase reactants at proton i, and a_j and ν_j are the gas-phase activity and reaction stoichiometry of species j, respectively. The $\Delta G_i^{\ddagger}$ reflect transition state free energies relative to gas-phase reactants, because transition states are in equilibrium with reactive intermediates and gas-phase species; this implies that transition states are also in equilibrium with transition states at other protons. Eq. (3) simplifies to

$$\langle \Delta G^{\ddagger} \rangle = -k_B T \ln \left(\frac{1}{N_{H^+}} \sum_{i=1}^{N_{H^+}} e^{\frac{-\Delta G_i^{\ddagger}}{k_B T}} \right), \tag{4}$$

which closely resembles Eq. (1) when DME interaction energies replace free energies and protons are located at all accessible O-atoms.

3. Results and discussion

3.1 Brønsted acid site titrations and contributions of Brønsted and Lewis acid sites to measured CH_3OH dehydration rates

The number of accessible protons must be measured to express their reactivity as turnover rates, thus allowing comparisons of their reactivity among different zeolite structures. The number of protons was determined here from 2,6-di-*tert*-butylpyridine, pyridine, and CH_3NH_2 uptakes during catalysis (Table 1). All zeolites in this study are henceforth referred to by their framework type, but are implicitly in their H-form. Smaller pyridine and CH_3NH_2 titrants were used when larger 2,6-di-*tert*-butylpyridine titrants, which selectively titrate Brønsted acid sites,[45] could not be used to access protons in structures with 10-MR and 8-MR windows or channels. Rates decreased linearly with the amount of adsorbed titrant and did not increase when the titrant was removed from the reactant stream (Figure 1), indicating that titrants bind irreversibly onto the acid sites that catalyze CH_3OH dehydration to DME, as shown previously on W-based polyoxometalates[16] and MFI zeolites.[11]

Pyridine interacts with Brønsted and Lewis acid sites to form characteristic infrared absorption bands at ca. 1545 cm^{-1} and ca. 1455 cm^{-1}, respectively.[25] The infrared absorption band characteristic of the pyridinium ion (1545 cm^{-1}) increased linearly, and the Brønsted ν(OH)

band (3604 cm^{-1}) decreased linearly, with pyridine uptake (Figure 2) up to pyridine/Al ratios of unity, consistent with measured H^+/Al ratios of unity (Figure 1) and with the irreversible binding of pyridine to protons. The absorption band characteristic of pyridine interacting with Lewis acid sites (ca. 1455 cm^{-1}) was undetectable below pyridine/Al ratios of unity, then increased linearly with increasing pyridine pressure, and decreased upon evacuation of gaseous pyridine (Figure 2), consistent with the reversible binding of pyridine to Lewis acid sites. The reversible binding of pyridine to Lewis acid sites shows that pyridine selectively titrates Brønsted acid sites. The proton affinity of CH_3NH_2 (899 kJ mol^{-1} [46]) is significantly lower than that of pyridine (930 kJ mol^{-1} [46]), indicating that CH_3NH_2 titrants will also bind weakly and reversibly to any Lewis acid sites present in these zeolites.

2,6-di-*tert*-Butylpyridine did not fully suppress CH_3OH dehydration rates on CD-FAU, FAU (Figure 1) and BEA. CH_3OH dehydration rates after these titrations were independent of CH_3OH pressure and inconsistent with pre-titration rates that were proportional to CH_3OH pressure (Supporting Information). The addition of pyridine to reactant streams after 2,6-di-*tert*-butylpyridine titrations caused rates to decrease further; these rates increased, however, when pyridine was subsequently removed from reactant streams, consistent with the presence of Lewis acid sites and with the reversible binding of pyridine onto these sites (Figure 2). These data indicate that Lewis acid sites are present and make small contributions to measured CH_3OH dehydration rates on some zeolites (CD-FAU, CD-FAU and BEA); the reactivity of Lewis acid sites are determined from dehydration rates after titrant saturation. Brønsted acid-catalyzed turnovers were determined here by taking the difference in rates before and after titrations and correctly normalizing these rates by titrant uptakes, which reflect the number of Brønsted acid sites.

Brønsted acid site densities measured from the amount of NH_3 evolved from NH_4^+-exchanged zeolites were smaller by factors of 0.8 (MTT, SFH and 3 MFI samples) and 0.7 (MTW) than those determined from titrations during catalysis (Table 1). NH_4^+ selectively replaces H^+ during aqueous exchange and thus probes only Brønsted acid sites. The differences in site counts among pyridine and CH_3NH_2 titrations and NH_3 evolution may reflect the adsorption of amine titrants onto Lewis acid sites; the reversibility of amine titrants on Lewis acid sites (Figure 2) and the low pressures of amines during titrations, however, preclude large contributions of these sites to measured titrant uptakes. These differences may instead reflect the hydrolysis of the zeolite framework under aqueous NH_4^+-exchange procedures, which can lead to a loss in zeolite crystallinity and a concomitant loss in the number of protons in some zeolites.[47]

NH_4^+ amounts were larger (by factors of 1.5-1.7) than 2,6-di-*tert*-butylpyridine uptakes on CD-FAU, FAU and BEA samples. These samples have very low H^+/Al ratios (<0.37 from 2,6-di-*tert*-butylpyridine titrations) and thus a significant amount of Al outside of tetrahedral framework positions. ^{27}Al MAS NMR indicates that Al species convert from tetrahedral to octahedral coordinations, which do not have associated Brønsted acid sites, in the presence of H_2O in FAU[48] and BEA[49] structures at moderate temperatures (298-443 K) because of the hydrolysis of Al-O bonds. NH_3 adsorption reestablishes the tetrahedral coordination of some Al-atoms leading to the creation of associated NH_4^+ cations, but these Al-atoms revert to octahedral coordinations when NH_3 is thermally removed (723 K) and the samples are introduced to

moisture at ambient conditions.[48, 49] Al-atoms that coordinate with NH_4^+ cations during ion-exchange procedures, but do not have associated Brønsted acid sites during catalysis are consistent with the larger quantities of NH_3 than protons titrated with 2,6-di-*tert*-butylpyridine on CD-FAU, FAU and BEA samples (Table 1). We conclude that accurate Brønsted acid site counts require titrations during catalysis.

3.2 CH_3OH dehydration turnover rates and mechanistic interpretations of rate constants on zeolites

CH_3OH dehydration turnover rates for CD-FAU, SFH, MFI-7, BEA, and MTW are shown in Figure 3 as a function of CH_3OH pressure, with trace contributions from Lewis acid sites removed (as described in Section 3.1). These data are consistent with a rate equation derived from a sequence of elementary steps proposed previously on polyoxometalates and zeolites (Scheme 2):[11, 16]

$$\frac{r_{DME}}{\left[H^+\right]} = \frac{k_{DME} K_D \left[CH_3OH\right]}{1 + K_D \left[CH_3OH\right]} = \frac{k_{first} \left[CH_3OH\right]}{1 + \frac{k_{first}}{k_{zero}} \left[CH_3OH\right]} \quad (5)$$

Here, k_{DME} is the rate constant for the formation of DME from protonated CH_3OH dimers, and K_D is the equilibrium constant for the formation of these dimers from H-bonded CH_3OH species. The terms in the denominator of Eq. 5 represent the relative concentrations of H-bonded CH_3OH monomers and CH_3OH dimers; infrared spectra during reaction have shown that these two species are the most abundant adsorbates at low and high CH_3OH pressures, respectively, on MFI, FAU, and MOR.[50] H-bonded CH_3OH monomers predominant at low CH_3OH pressures where turnover rates increased linearly with CH_3OH pressure (Figure 3) preclude dehydration turnovers that proceed through methoxide-mediated routes, because these routes would lead to turnover rates that are independent of CH_3OH pressure.[11]

Eq. (5) contains two rate constants (k_{first} and k_{zero}). One rate constant (k_{first}) is given by the slope of the plots in Figure 3 at low CH_3OH pressures and reflects the free energy difference between the confined DME formation transition state and a confined H-bonded CH_3OH and a gaseous CH_3OH (Scheme 1). The other rate constant (k_{zero}) reflects the asymptotic turnover rates at high pressures in Figure 3 and the free energy difference between the same confined transition state and a confined protonated dimer (Scheme 1). The values of k_{first} and k_{zero} decreased exponentially with increasing DPE values (as acid sites weakened) on W-based polyoxometalate clusters (POM) with different central atoms[16] and MFI zeolites with Al, Ga, Fe and B heteroatoms,[11] because weaker acids require more energy to separate charge and form the required ion-pair transition states than stronger acids.[14]

The stability of ion-pair transition states and reactive intermediates depend on acid strength in manner that reflects their extent of charge separation, but also on the shape and size of voids, which solvate species with van der Waals interactions that depend on interaction distances ($\sim r^6$) and the identity of the atoms involved. First-order rate constants on BEA[16] and MFI[11] zeolites are larger than those expected for a (hypothetical) POM structure with similar DPE (by extrapolation of POM rate data[16]). Such reactivity enhancements by confinement reflect the

preferential solvation of DME transition states over H-bonded CH_3OH monomers within these confining voids (Scheme 1). Zero-order rate constants, in contrast, are similar on zeolites with different void sizes (Section 3.3), because protonated CH_3OH dimers and DME transition states are similar in size and thus in their number of van der Waals contacts with the confining framework. As a result, they are stabilized to similar extents by confinement (the approximate size of molecules and effects of confinement on activation barriers are illustrated in Scheme 1). The individual contributions of acid strength and confinement to reactivity can be interpreted from the relative values of k_{first} and k_{zero} because their values depend differently on acid strength and confinement. Next, we compare CH_3OH dehydration rate constants on a series of crystalline aluminosilicates with different framework structures to assess how differences in van der Waals stabilization influence the reactivity of solid Brønsted acids.

3.3 Consequences of van der Waals interactions on CH_3OH dehydration rate constants and the acid strength of zeolites

Here, we probe how zeolite structure influences acid strength and solvation by comparing CH_3OH dehydration activation free energies (from k_{first} and k_{zero}) with enthalpies for the physical adsorption of alkanes in these zeolites. Alkane adsorption enthalpies on zeolites depend predominantly on van der Waals interactions; the additional stabilization of an alkane by a proton is much smaller than that by van der Waals contacts with an all silica framework and is similar on various zeolite frameworks (~6-10 kJ mol^{-1} on FAU and MFI frameworks).[40] Thus, alkane adsorption enthalpies serve as a convenient proxy for van der Waals interactions caused by confinement of such molecules within zeolite voids. In particular, n-C_6H_{14} molecules are of an appropriate size to probe van der Waals interactions that influence DME transition states (Figure 5) and their adsorption enthalpies have been measured on a number of zeolite samples.[51]

Figure 4 shows first-order and zero-order CH_3OH dehydration rate constants as a function of n-C_6H_{14} adsorption enthalpies (-Q_{ads}(n-C_6H_{14}), microcalorimetry at 423 K[51]) on CD-FAU, BEA, MOR and MFI zeolites. First-order rate constants increased exponentially with increasing Q_{ads}(n-C_6H_{14}) (25-fold for Q_{ads} from 38 to 56 kJ mol^{-1}; Figure 4). Zero-order rate constants, in contrast, were quite similar and were much less sensitive to Q_{ads}(n-C_6H_{14}) values (Figure 4), indicating that acid strength is similar in these zeolites, given the exponential dependence of k_{zero} values on DPE.[11, 16] These similar zero-order rate constants also show that van der Waals interactions stabilize DME formation transition states and protonated CH_3OH dimer species comparably, because the shape, size and number of van der Waals contacts are similar for these two species (Scheme 1).

First-order rate constants differed by a factor of ~25 among these zeolites (Figure 4) and increased exponentially (except for MFI(I) and FAU, as discussed below) with increasing values of Q_{ads}(n-C_6H_{14}). We conclude from this trend that smaller voids, which solvate n-C_6H_{14} more effectively than larger voids, also solvate DME transition states more effectively than smaller H-bonded CH_3OH species, because of the larger size and number of van der Waals contacts for these transition states than H-bonded CH_3OH (Scheme 1). The effects of Q_{ads}(n-C_6H_{14}) on k_{first} (Figure 4) indicate that (i) these Al-zeolites are similar in acid strength, because DPE affects k_{first} exponentially,[11, 16] but Q_{ads}(n-C_6H_{14}) values predominantly reflect van der Waals interactions;

or, (ii) that DPE values increase monotonically with increasing void size, because increasing DPE values decrease k_{first}.[11] DFT-derived DPE values for FAU, CHA, MOR and MFI do not change in any monotonic manner with T-O-T bond angles and do not increase with increasing void size.[13, 52] A 66 kJ mol^{-1} increase in DPE from the substitution of Al heteroatoms with B in MFI resulted in a ~1000-fold decrease in the value k_{first},[11] indicating that small DPE differences would change k_{first} appreciably and affect the trends in Figure 4. We conclude that zeolites with different frameworks and structural building blocks exhibit similar acid strengths and that their catalytic diversity predominantly reflects their non-uniform voids and the confinement of transition states within them.

The conclusion that acid strength in zeolites is similar among different frameworks is also consistent with the similar k_{zero} values between zeolites (discussed above, Figure 4) and with the similar intrinsic activation barriers for monomolecular propane cracking on several zeolites (199 ± 11 kJ mol^{-1}, on FAU, BEA, MOR, MFI, MWW, and FER).[2, 6] Barriers for monomolecular propane cracking reflect differences in enthalpy between transition states and alkanes that are similar in size and which are both confined within the zeolite voids. DFT-derived DPE estimates for different zeolite frameworks, however, differ by as much as 30 kJ mol^{-1} (QM-Pot).[13] These DPE values are inconsistent with the larger k_{first} values measured on MFI (1200 kJ mol^{-1}) than on CD-FAU (1171 kJ mol^{-1}), because larger DPE values lead to smaller values of k_{first}.[11, 16] DFT-derive DPE values, however, are calculated on single crystallographically unique Al-O(H)-Si sites and do not reflect the locations and distributions of protons in zeolite samples. Rate constants, in contrast, reflect the exponential average of free energy differences of transition states with reactive intermediates at all accessible proton locations allowed from Al-atom distributions (Section 2.6). The difference in DPE values calculated with DFT methods, not reflected in k_{first} trends, may also reflect errors in the approximations of DFT methods, which require models for periodic zeolite structures.

First-order rate constants reflect the average van der Waals stabilizations of transition states and reactive intermediates at each proton; thus k_{first} values are an indicator of the locations of acid sites in zeolite voids of different size and shape. The rate constants labeled MFI(S) and MFI(I) in Figure 4 refer to the MFI sample with the highest Al content (Si/Al = 16.6, MFI-1) and to another five MFI samples with lower Al content (Si/Al = 22-118, MFI-2 to MFI-6), respectively.[11] MFI(S) shows larger k_{first} values than MFI(I) samples, but similar k_{zero} values. MFI(S) also shows an infrared band (at 3656 cm^{-1}) in addition to that corresponding to the acidic OH groups present in all MFI(I) samples (at 3604 cm^{-1}). These data, taken together, indicate that some protons in MFI(S) are located in a different and more confined space than in MFI(I), because larger k_{first} are consistent with increased confinement. These results led to the previous conclusion that some protons reside within straight and sinusoidal channels, instead of larger intersections, only at the highest Al contents.[11] This is consistent with k_{first} values on MFI(I) that lie below the trend line that related such constants to n-C_6H_{14} adsorption enthalpies for the other zeolites (Figure 4), because n-C_6H_{14} adsorbs preferentially within the smaller voids, where van der Waals interactions are stronger,[40] but reactions occur and transition states are stabilized only at the intersection locations where protons reside in MFI(I) samples. The predominant siting of protons at intersections (0.63 nm largest included sphere diameter[7]) in MFI(I) is also consistent with similar k_{first} values (Figure 4) for MFI(I) and BEA (0.61-0.66 nm largest free and included sphere diameters[7]), because of the similar sizes of these voids.

The larger values of k_{first} (but not of k_{zero}) on FAU (8-fold higher) relative to CD-FAU are also indicative of the tighter confinement of transition states in FAU, in spite of the identical framework structure of these two samples. CD-FAU was prepared by treating FAU with $(NH_4)_2SiF_6$ to remove any extra-framework Al debris formed during steam treatment (Section 2.1). FAU contains only one crystallographically unique Al-atom position and protons that are accessible to DME transition states are contained in the supercage void (1.1 nm[7]). The smaller k_{first} on CD-FAU than on other zeolites (Figure 4) reflects the weak van der Waals stabilization of DME formation transition states within the large debris-free FAU supercages. The larger k_{first} values for FAU than for CD-FAU are due to detrital Al species (absent in CD-FAU), which occlude some of the volume of the supercages, making them more effective in confining precursors and transition states, as proposed earlier to account for higher isobutane cracking turnover rates on FAU than on CD-FAU.[17]

The comparable k_{first} values for BEA (intersecting 12-MR straight channels), MOR (1D 12-MR channel) and MFI(I) (intersecting straight and sinusoidal 10-MR channels, with H^+ at intersections) reflect the similar size of these voids and their confinement of transition states and relevant precursors. The exact location of protons at distinct O-atoms in these samples, however, is unclear from these trends, in part, because n-C_6H_{14} adsorption enthalpies reflect an average of van der Waals interactions at many O-atoms. The assessment of van der Waals interactions relevant to measured rate constants, therefore, requires theoretical treatments of transition states, or appropriate surrogates, at each proton. DFT calculations of van der Waals interactions of DME in zeolites are discussed next and compared with measured rate constants.

3.4 DFT-derived DME binding as a probe for van der Waals stabilization of DME formation transition states

van der Waals stabilization of molecular structures reflects the location of the proton involved. Experiments cannot probe such interactions at specific locations because adsorption measurements average over all accessible locations, but such location-specific properties can be probed by theory for known structures. Here, we estimate such interactions at different O-atom locations using DFT-derived DME van der Waals interaction energies and compare these with the 25-fold differences in CH_3OH dehydration rate constants in zeolites (FAU, BEA, MOR, MFI, and MTT) that reflect free energy differences of DME transition states and relevant precursors.

DFT methods have shown that CH_3OH dehydration is mediated by late and loose transition states that resemble a protonated DME molecule interacting with a nearly neutral -OH_2 molecule (Figure 5).[16] Bond distances and angles in DME molecules and these transition states (Figure 5) suggest that the former would capture the essential van der Waals interactions in confined transition state structures. The use of DME as a surrogate for these transition states avoids the computational intensity of transition state search algorithms at each location and allows representative samples of all accessible locations in a given framework. DME interaction energies, however, do not accurately reflect the charged nature of the transition state, its precise location within a void, or any stabilization by the -OH_2 moiety, all of which may influence these

van der Waals interactions. Yet, the relation between DME formation rate constants and van der Waals stabilization of DME verify the value of the latter as a descriptor of reactivity.

Figure 6 shows measured CH_3OH dehydration rate constants (FAU, BEA, MOR, MFI, and MTT) as a function of DFT-derived van der Waals interaction energies for DME (Q_{vdw}(DME)) at individual acid sites determined from the dispersive component of DME binding enthalpies from periodic-DFT methods with vdW-DF2 functionals (Section 2.5). These functionals accurately reflect van der Waals interactions and bonding interactions over large distances, indicated by potential-energy curves calculated for a range of molecule-molecule interactions that agree with quantum chemical calculations at the coupled-cluster level of theory.[30] The rate constants labeled MFI(S) and MFI(I) in Figure 6 refer to high Al content MFI (Si/Al = 16.6, MFI-1) and the average of five MFI samples with lower Al content (Si/Al = 22-118, MFI-2 to MFI-6), respectively; Q_{vdw}(DME) values were calculated for DME adsorbed in the sinusoidal channel and the intersection void of MFI structures (Sections 2.5 and 3.3). Measured k_{first} values increased exponentially with increasing Q_{vdw}(DME) values (Figure 6), except for MTT (discussed below), consistent with van der Waals interactions as the predominant descriptor of reactivity differences among zeolites (Section 3.3). DME binding enthalpies with van der Waals interaction contributions removed (Q_{nd}(DME) = Q(DME) – Q_{vdw}(DME)), in contrast, do not trend monotonically with k_{first} (Table 2) because non-dispersive interactions depend on the orientation and overlap of molecular orbitals and do not reflect the non-specific nature of van der Waals interactions that dominate reactivity differences.

DFT-derived DME interaction energies were calculated from the energy of DME interaction at a single proton (proton locations are discussed in Section 2.5); therefore, they do not reflect the diversity of confining environments of protons in each structure, all of which contribute to measured rate constants. FAU contains one crystallographically-distinct tetrahedral sites (T-sites) and four crystallographically-distinct O-atoms;[36] three of those O-atoms would lead to protons within the uniform solvating environment of the FAU supercage voids, and one in the sodalite cage which is inaccessible to DME molecules. As a result, the van der Waals component of DME interaction energies at Al1-O1(H)-Si1 sites (using established nomenclature[36]) in the supercage is the smallest among all zeolites (37 kJ mol^{-1}; Table 2) because of the large size of supercage voids (1.1 nm[7]) and the correspondingly larger distances between framework atoms and the DME molecule than calculated in zeolites with smaller pores. BEA contains nine crystallographically-distinct T-sites and 17 unique O-atoms[53] with accessible binding sites (Section 2.6) located in the 12-MR channels (~0.60 nm[7]) and in their intersections (~0.66 nm[7]), which are similar in size. Adsorption of DME at the Al2-O7(H)-Si7 site[36] located at the intersection of the channels in BEA results in a factor of 1.7 larger Q_{vdw}(DME) (63 kJ mol^{-1}; Table 2) than for FAU, reflecting the tighter confinement within these 12-MR channels than in FAU supercages, consistent with the larger k_{first} values in BEA than in FAU (Figure 6).

MTT structures contain 10 distinct O-sites, but only 5 are in the one-dimensional 10-MR channels accessible to DME.[36] DME binding at Al3-O6(H)-Si7 sites[36] in these 10-MR MTT channels occurs with a larger Q_{vdw}(DME) (75 kJ mol^{-1}; Table 2) than in BEA or FAU, as a result of the smaller size of the confining environment. Yet, first-order rate constants in MTT resemble those in BEA (Table 2). As a result, k_{first} values do trend monotonically with Q_{vdw}(DME) (Figure 6). These discrepancies seem to reflect the distribution of Al-atoms in zeolite structures, which

lead, in turn, to differences in the van der Waals interactions of transition states and reactive intermediates. Q_{vdw}(DME) values calculated in MOR differ by as much as 70 kJ mol^{-1} depending on the orientation and locations of DME at 5 unique O-atoms (Supporting Information), indicating that the location and distribution of protons can affect the stabilization of transition states. More accurate representations of the solvation reflected in k_{first} require a consideration of the confinement present at catalytically relevant protons. In Section 3.5, force-field calculations of DME binding at all DME-accessible protons indicate that DME van der Waals interaction energies averaged over all proton sites (Section 2.6) in MTT are similar to those within the 12-MR channels of MOR, indicating that the reactive consequences of proton distributions are similar to that of random distributions of protons in these samples. These calculations are discussed next for a wide variety of zeolites to assess DME van der Waals interaction energies at all crystallographically unique and catalytically relevant protons.

3.5 The influence of van der Waals interactions and acid site location on rate constants of CH_3OH dehydration

The distribution of Al-atoms among T-sites in zeolites depends sensitively on synthetic procedures, but it is seldom accessible to experimental probes, except to materials, such as MOR, with very distinct intracrystalline void environments.[8, 9, 54] The assessment of Q_{vdw}(DME) values at all accessible O-atoms in the zeolites considered here in this paper (~100 O-atoms) remains computationally prohibitive using DFT methods and unnecessary because the van der Waals component of these adsorption energies can be estimated accurately using Lennard-Jones potentials to describe interactions between confined molecules and the O-atoms of the zeolite framework.[40]

Here, we employ Lennard-Jones potentials[39,40] to assess the van der Waals interactions of DME at all accessible crystallographically unique O-atoms in zeolite structures (CD-FAU, BEA, SFH, MTW, MTT, MFI(S) and MOR; Section 2.6). The most stable DME interaction energies at each O-site were averaged ($<Q_{LJ}$(DME>) at 433 K from the sum of Arrhenius-type exponentials containing interaction energies to reflect the averaging of transition state free energies at all Brønsted acid sites in rate constants (Section 2.6). Rate constants, however, reflect the average of free energy differences of transition states only at O-sites where protons exist.

Figure 7 shows CH_3OH dehydration rate constants on CD-FAU, BEA, SFH, MTW, MTT, MFI(S) and MOR samples as a function of $<Q_{LJ}$(DME)> values. The MFI(I) entry averages Waals interaction energies only for protons at intersections, whereas the MFI(S) entry averages those interactions at all accessible O-sites; the monotonic trends of rate constants with these energies (Figure 7) support the preferential siting of protons in the intersections of MFI at low Al densities (discussed also in Sections 3.3 and 3.4).

First-order (but not zero-order) rate constants increased exponentially with $<Q_{LJ}$(DME)> values. This supports our previous conclusions that dispersive interactions dominate the reactivity differences of zeolites because $<Q_{LJ}$(DME)> values depend only on these non-specific interactions. Zero-order rate constants are similar and independent of $<Q_{LJ}$(DME)> values because of the similar shape, size and number of van der Waals contacts of transition states and CH_3OH dimers (Scheme 1). The fixed values of k_{zero} and the monotonic trends of k_{first} with

$<Q_{LJ}(DME)>$ also support the unchanging acid strength of zeolites with different structure, provenance, Al-density and treatments, because these rate constants depend exponentially on acid strength.

$<Q_{LJ}(DME)>$ values reflect the DME van der Waals interaction energies at all protons accessible to DME (0.325 nm diameter spherical probe; Section 2.6) and makes no assumptions about the locations of protons. The monotonic trends of k_{first} versus $<Q_{LJ}(DME)>$ in Figure 7 indicate that the reaction-averaged (Section 2.6) solvation differences of transition states due to confinement are similar to those differences of $<Q_{LJ}(DME)>$ calculated at all protons. Deviations from these trends can be explained by the preferential siting of protons due to Al-atom locations fixed during synthesis, or subtle differences in the way transition states structures are influenced by confinement differently than DME.

Next, we assess DME interaction energies at specific O-atom locations to understand the variability of solvation environments in a given zeolites. Figure 8 shows $Q_{LJ}(DME)$ values calculated at all accessible protons and their ensemble average $<Q_{LJ}(DME)>$ as a function of largest free sphere diameters (d_f).[7] $Q_{LJ}(DME)$ values vary up to 9 kJ mol^{-1} (SFH) in a single zeolite and depend sensitively on the locations of protons in their voids. Thus, the distribution and location of protons can affect the solvation of transition states and precursors. $<Q_{LJ}(DME)>$ values loosely correlate with d_f values in accordance with the r^{-6} dependence of van der Waals stabilizations. Zeolite size metrics, therefore, provide qualitative indicators of the confinement of transition states but do not necessarily reflect the distribution and variety of voids that are relevant to catalysis.

van der Waals interactions between DME and zeolite voids depend on atom identity and atom-to-atom distances, but the variance in $Q_{LJ}(DME)$ values in a given zeolite are sometimes surprising. For example, $Q_{LJ}(DME)$ values range from 12 to 21 kJ mol^{-1} ($<Q_{LJ}(DME)>$ = 18 kJ mol^{-1}) at various proton-binding sites, yet DME structures are all contained within the one-dimensional 14-MR channels of SFH. The variety of $Q_{LJ}(DME)$ values is caused by the asymmetric shape of these channels, which resemble a teardrop shape rather than a circle (Figure 9), and not binding locations in radically different environments. DME located at the wider section of these channels have higher van der Waals interaction energies because DME molecules can rotate perpendicular to channel directions to increase solvation. First-order rate constants of SFH are similar to those for MOR and MTW (Figure 7), consistent with protons located preferentially in wider sections of the 14-MR channels and the $Q_{LJ}(DME)$ values there. We conclude that the shape and size of zeolite voids and the specific locations of protons among those voids are important for determining van der Waals interactions that accurately reflect those relevant to catalysis.

The exponential increases in first-order, but not zero-order CH_3OH dehydration rate constants with measured $Q_{ads}(n\text{-}C_6H_{14})$ (Section 3.3, Figure 4), calculated $Q_{vdw}(DME)$ (Section 3.4, Figure 6), and calculated $<Q_{LJ}(DME)>$ (Section 3.5, Figure 7) provide compelling evidence that confinement and not acid strength differences influence the differences in stability of transition states in aluminosilicates. These results also demonstrate that van der Waals interactions influence rate constant values only when transition states and reactive intermediates differ in shape, size and number of van der Waals contacts, as is the case for first-order, but not

zero-order, rate constants. Efficient force-field calculations of transition state proxies accurately reflect the differences in van der Waals interactions due to confinement and relevant for catalysis and permit the screening of large databases of zeolite structures[55] to narrow the discovery of catalytically relevant materials with enhanced reactivity and selectivity. The success of these methods will ultimately depend on knowledge or design of the location of Al within these structures, which governs the local environment, and thus the confinement of transition states and relevant reactive intermediates.

4. Conclusions

CH_3OH dehydration rate constants, normalized rigorously by the number of protons present during reaction, reflect differences in the electrostatic and dispersive stabilization of DME formation transition states and relevant precursors. First-order CH_3OH dehydration rate constants increased exponentially with n-C_6H_{14} adsorption enthalpies, which depend only on differences in van der Waals interactions, consistent with reactivity differences that are dominated by differences in confinement, but not acid strength. These trends and zero-order rate constants that are independent of aluminosilicate structure indicate that aluminosilicate Brønsted acid sites are sensibly equivalent in acid strength.

DME van der Waals interaction energies, calculated from periodic density functional theory and Lennard-Jones potentials, accurately reflect the van der Waals interactions of DME formation transition states, indicated by the monotonic increase in first-order rate constants with their values, consistent with the late DME-like structures of these transition states. DME interaction energies appropriately averaged over all accessible and crystallographically unique O-atoms in zeolites also reflect the systematic 25-fold increase in first-order rate constants with tighter confinement in FAU, SFH, BEA, MOR, MTW, MFI, and MTT; these trends imply that the average solvation of transition states in zeolites reflected in rate constant values is similar to the average solvation of transition states at all O-atoms for these zeolites. Deviations from these trends provide supporting evidence for the occlusion of supercage voids by detrital Al in FAU and the preferential location of protons in the channel intersections of MFI samples with Si/Al $\geq$ 22, consistent with infrared signatures of their Brønsted acid sites and similar first-order rate constant values for these MFI samples compared to BEA.

These findings reflect the magnitude of van der Waals interactions on the relative stability of transition states at different acid sites in zeolites. Acid strength differences of aluminosilicates are found to be insensitive to changes in structure, depending only on changes in the composition of framework heteroatoms. We find that non-specific dispersive interactions, previously described as transition state shape selectivity or nest-effects, are ubiquitous in microporous solid acid catalysis, and, in fact, are the dominant forces determining differences in their reactivity. The force-field methods described herein provide a novel method for the prediction of zeolites with enhanced reactivity and selectivity; more accurate predictions will ultimately rely on knowledge or selection of the locations and distribution of Al-atoms.

These results demonstrate that the remarkable diversity in reactivity of aluminosilicate catalysts is the result of subtle changes in the size and shape of zeolite voids, which lead, in turn, to differences in the solvation of transition states and reactive intermediates. The solvation of

transition states through van der Waals interactions parallels the interactions in enzyme catalysis and the solvation sphere of molecules around transition states in liquid media.

Acknowledgments

I acknowledge Dr. Stacey Zones (Chevron), Dr. Rob Carr (UC Berkeley) and Dr. Rajamani Gounder (UC Berkeley) for helpful technical discussions. Financial support from Chevron Energy Technology Company and supercomputing resources provided by the XSEDE Science Gateways program (CTS130011) are gratefully acknowledged. AJ acknowledges a graduate research fellowship from the National Science Foundation.

Figures, Tables and Schemes

Scheme 1. Schematic reaction coordinate diagram depicting transition state and reactive intermediates involved in CH_3OH dehydration and their relation to measured first-order ($E_{first}^{\ddagger}$) and zero-order ($E_{zero}^{\ddagger}$) CH_3OH dehydration rate constants. H-bonded CH_3OH monomers (left) are influenced less by tighter confinement (orange) than protonated CH_3OH dimers (middle) and cationic DME formation transition states (right) because of the smaller size and number of van der Waals contacts of monomers.

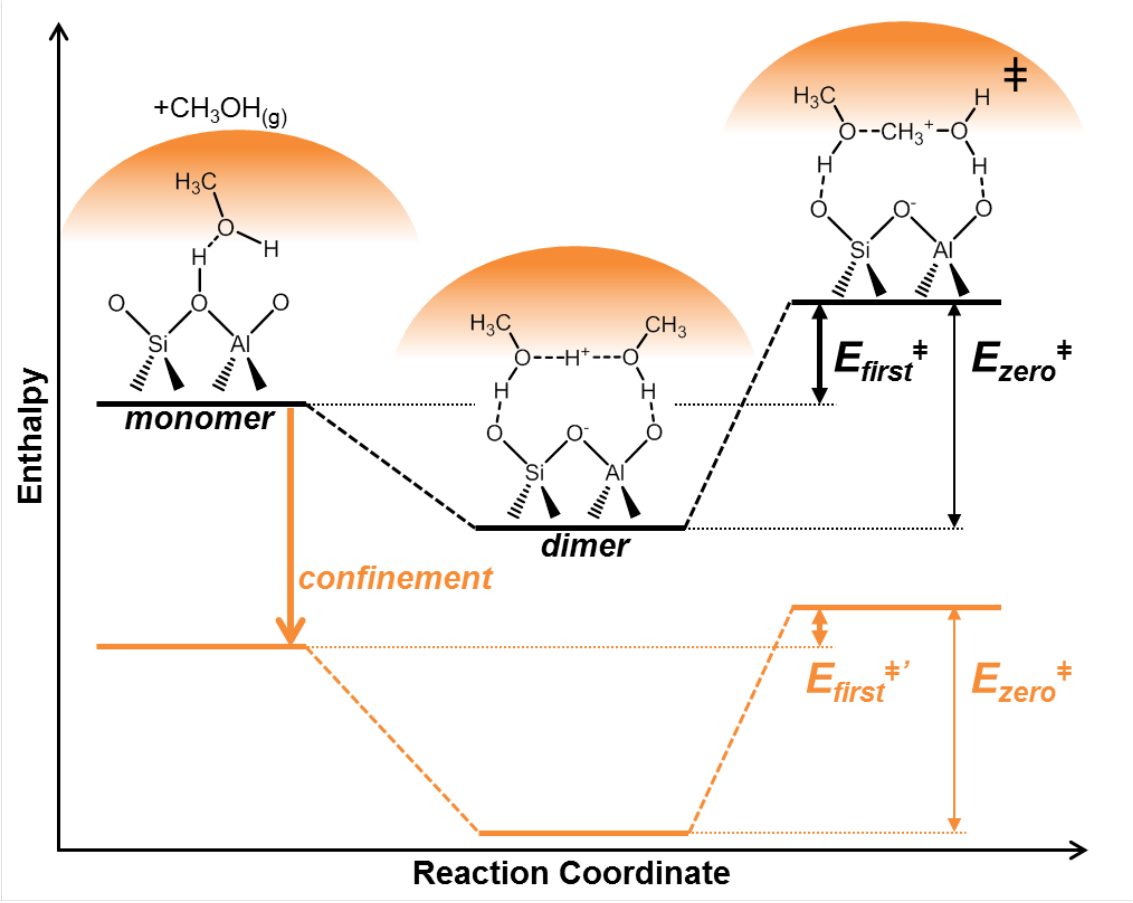

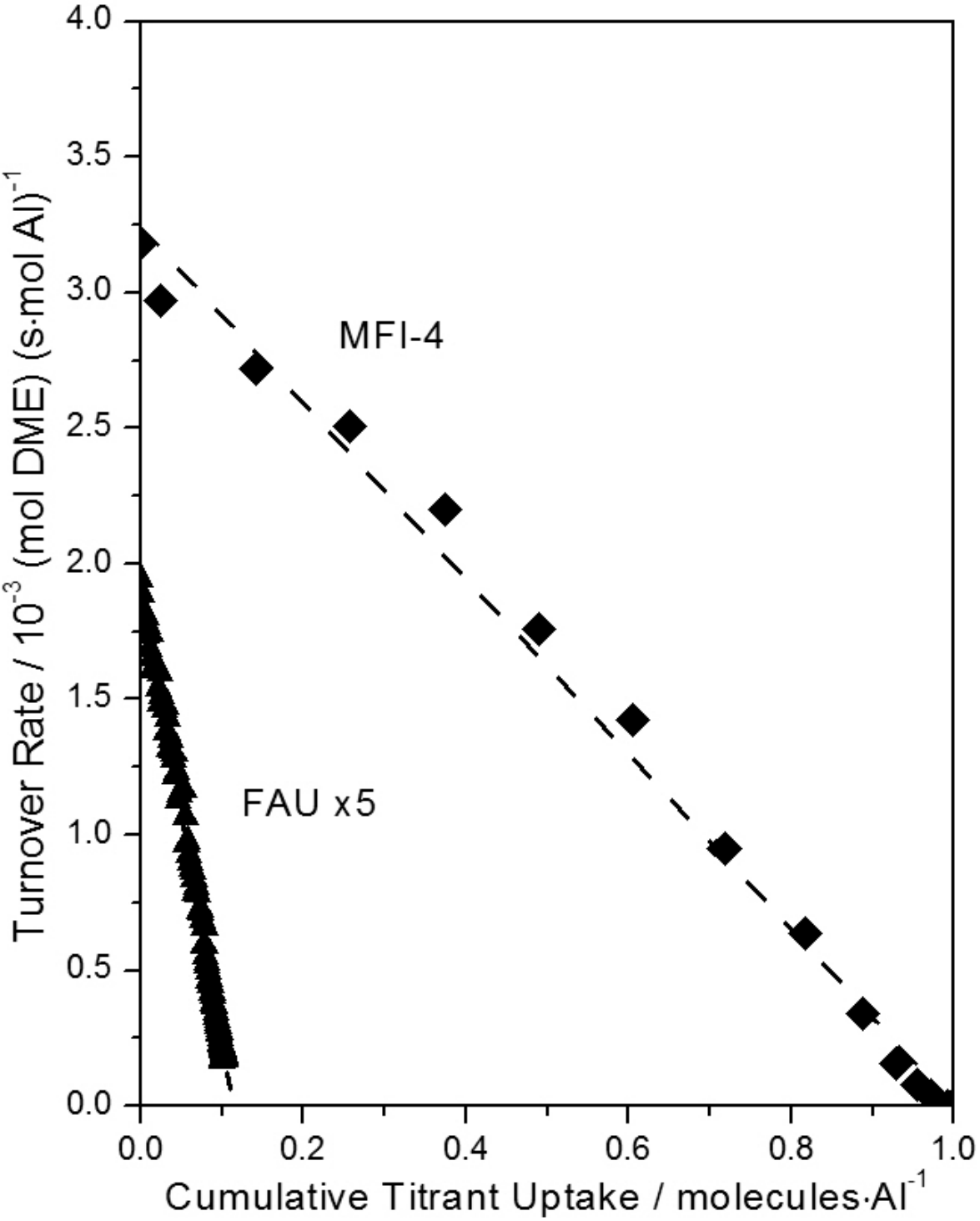

Fig. 1. CH_3OH dehydration turnover rates at 433 K as a function of cumulative titrant uptake on FAU (▲; 0.5 kPa CH_3OH and 0.1 Pa 2,6-di-*tert*-butylpyridine in the feed) and MFI-4 (♦; 1.1 kPa CH_3OH and 0.4 Pa pyridine in the feed). Dashed curves are linear regressions of the data.

Table 1. Al and H+ densities, void size descriptors and origins of zeolite samples

Zeolite	Source	Si/Al Ratio[a]	H^+/Al	H^+/Al[e]	Pore Env.	D_i / Å [f]	d_f / Å [g]
CD-FAU	Ref.17	7.5	0.37[b]	0.64	Supercage	11.18	7.29
FAU	Engelhard	2.8	0.10[b]	0.15	Supercage	11.18	7.29
SFH	This work	33.6	0.53[c]	0.40	14-MR	7.57	6.73
BEA	Zeolyst	11.8	0.24[b]	0.39	12-MR	6.62	6.07
MTW	This work	31.9	0.87[c]	0.63	12-MR	6.02	5.62
MOR-1	Zeolyst	10.0	0.46[c]	-	12-MR	6.64	6.39
MOR-2	Tosoh	9.1	0.38[c]	-	12-MR	6.64	6.39
MTT	This work	16.6	0.51[d]	0.46	10-MR	6.13	5.01
MFI-1	Zeolyst	16.6	0.65[c]	0.52	10-MR	6.30	4.64
MFI-2	Ref. 11	22.8	0.27[c]	0.33	10-MR	6.30	4.64
MFI-3	Zeolyst	29.2	0.77[c]	0.72	10-MR	6.30	4.64
MFI-4	Zeolyst	43.8	1.03[c]	0.89	10-MR	6.30	4.64
MFI-5	Ref. 11	51.9	0.59[c]	-	10-MR	6.30	4.64
MFI-6	Ref. 11	117.6	0.86[c]	-	10-MR	6.30	4.64

[a] Elemental analysis (ICP-OES; Galbraith Laboratories); [b] Titration by2,6-di-*tert*-butyl pyridine; [c] Titration by pyridine; [d] Titration by CH_3NH_2; [e] NH_3 evolution from NH_4^+-exchanged samples; [f] Largest included sphere diameter;[7] [g] Largest free sphere diameter.[7]

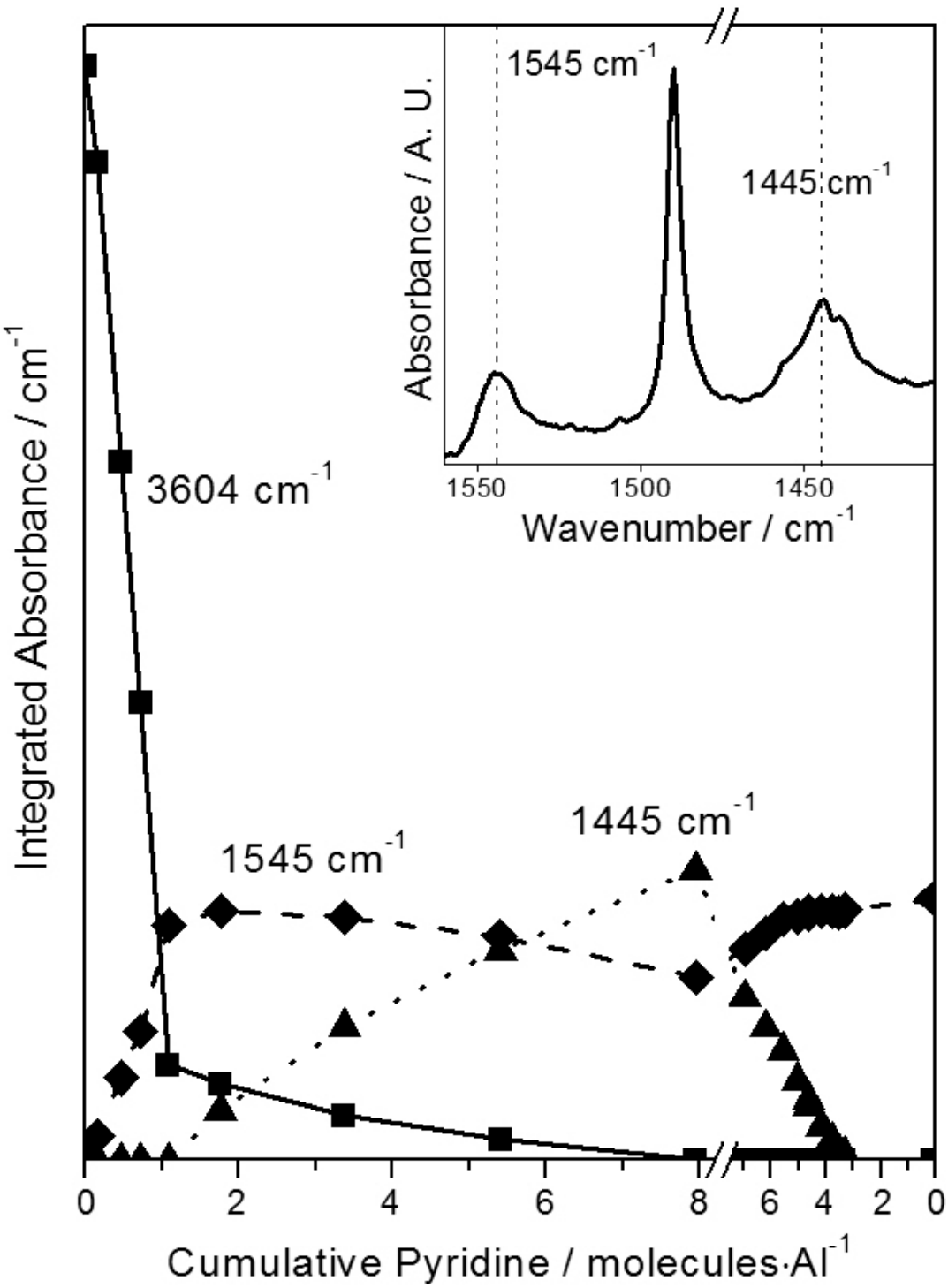

Fig. 2. Integrated infrared absorbance of absorption bands characteristic of Brønsted ν(OH) (■; 3604 cm^{-1}), pyridinium ions (♦; 1545 cm^{-1} [25]), and pyridine-Lewis interactions (▲; 1445 cm^{-1} [25]) as a function of pyridine dosed (and removed) per Al on MFI-4 at 433 K. Curves are provided as a guide. Inset: infrared spectra of MFI-4 dosed with 8 pyridine/Al.

Scheme 2. Elementary steps for CH_3OH dehydration over Brønsted acids.

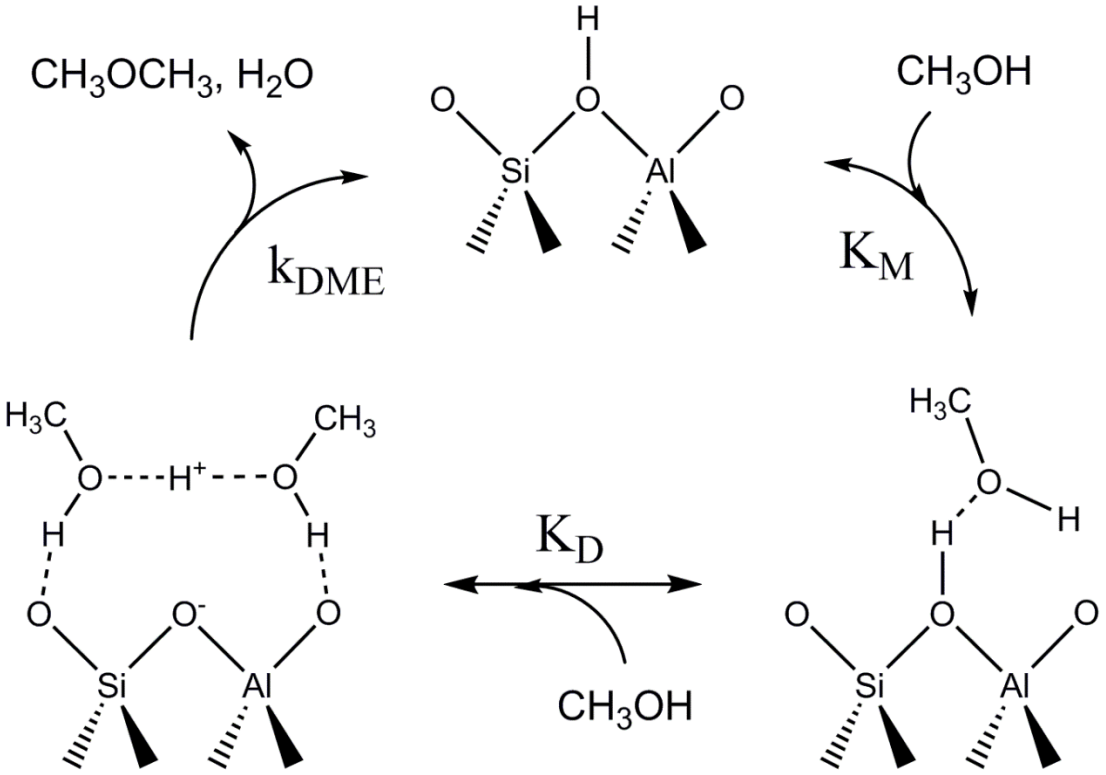

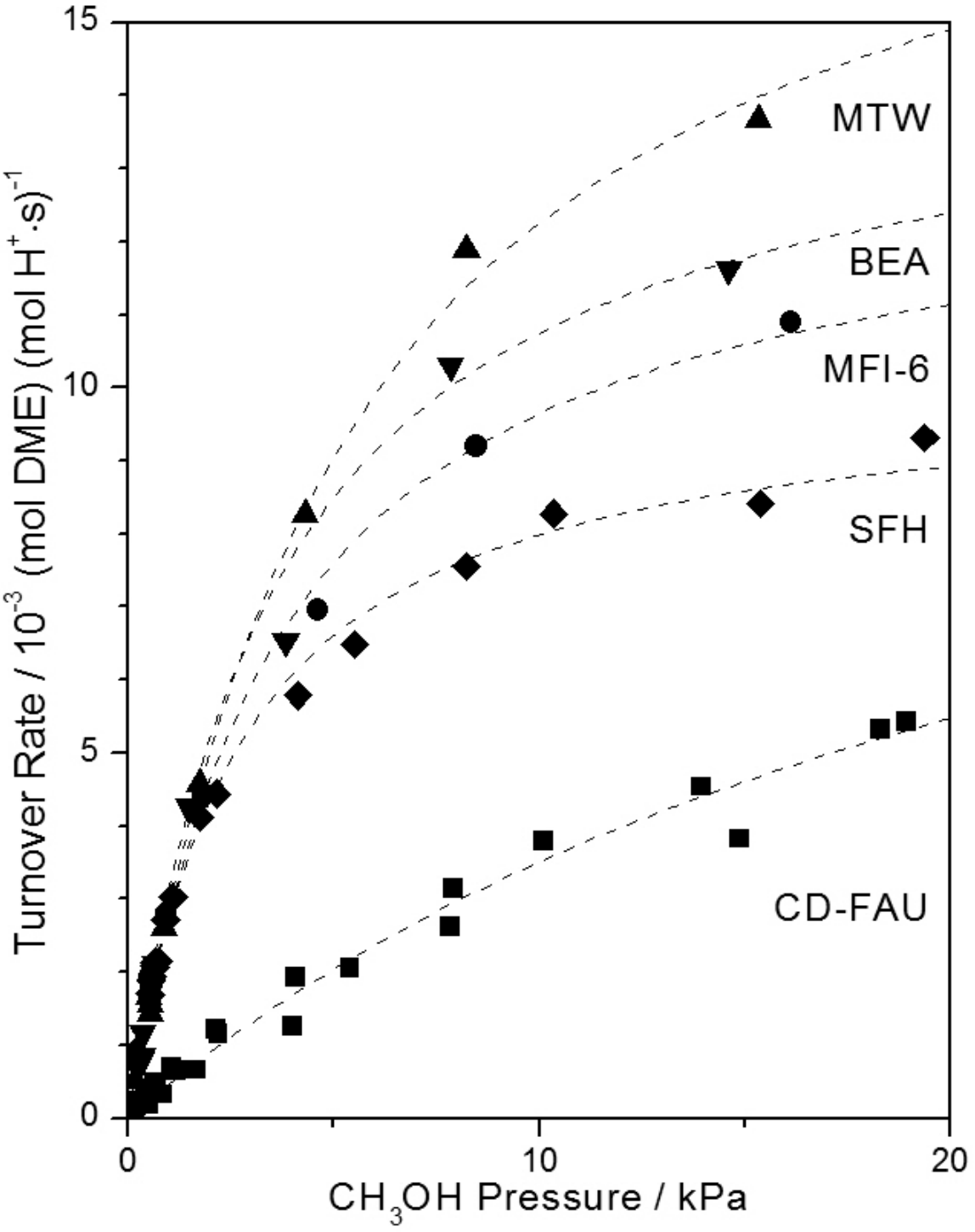

Fig. 3. CH_3OH dehydration turnover rates (per H^+ determined from base titrations as indicated in Table 1; 433 K) as a function of CH_3OH pressure on CD-FAU (■), SFH (♦), MFI-6 (●), BEA (▼), and MTW (▲). Dashed curves represent regression of the data to the functional form of Eq. (5).

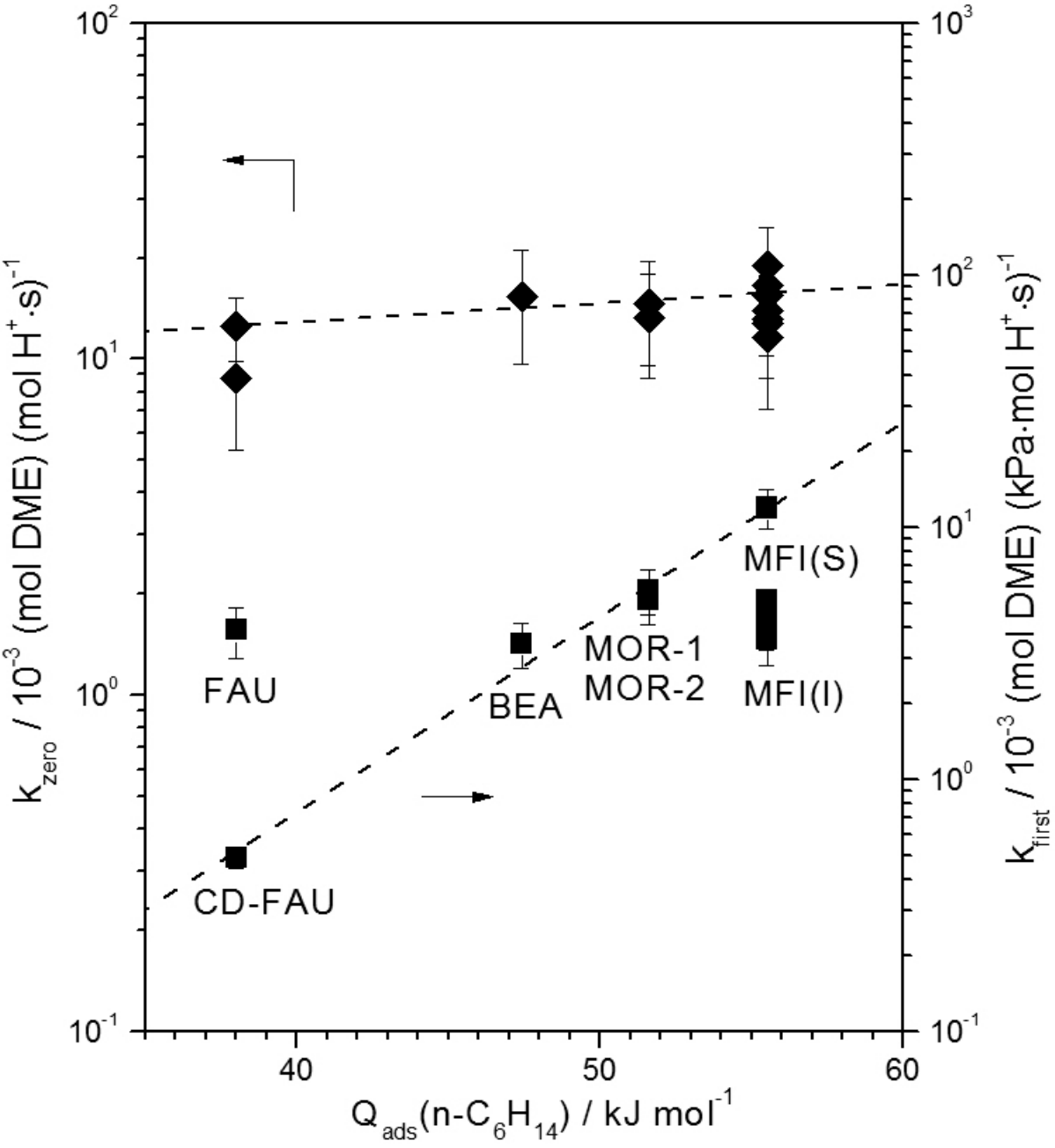

Fig. 4. CH_3OH dehydration rate constants (433 K) plotted versus n-C_6H_{14} adsorption heats[51] on protons in CD-FAU, FAU, BEA, MOR and MFI. Two rate constants are given for MFI corresponding to those samples where H^+ are located in the channel intersection void (I; average of rate constants of MFI-2 to MFI-6) or the sinusoidal channel (S; MFI-1) as indicated in our previous work[11] and discussed herein. Dotted lines are provided to guide the eye.

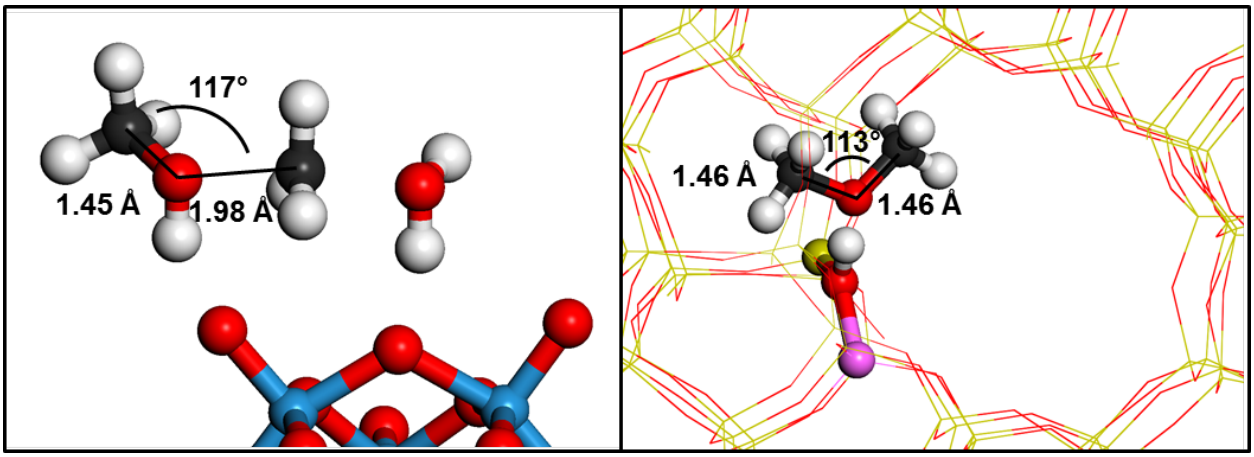

Fig. 5. DME formation transition state (left), reproduced from Carr et al.[16] on HAlW, compared with DME adsorbed in MFI at Al12-O20(H)-Si3 (right) calculated at the vdW-DF2/PAW level of DFT. Atom colorings are red (O), yellow (Si), purple (Al), white (H), blue (W) and charcoal (C).

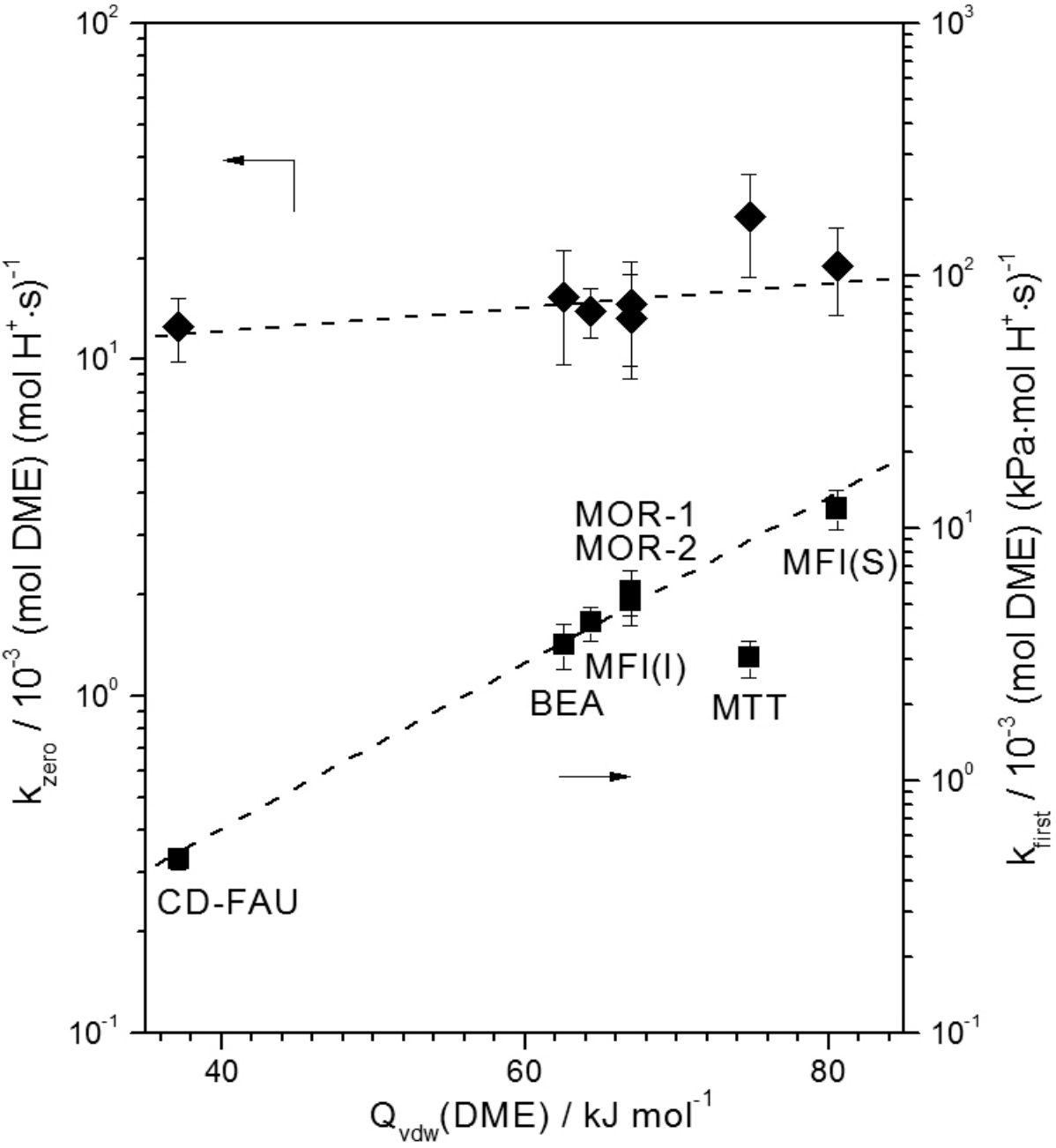

Fig. 6. CH_3OH dehydration rate constants at 433 K as a function of DFT-derived DME van der Waals adsorption energies calculated at H^+ in FAU (CD-FAU), BEA, MTT, and MOR, and at H^+ located in the channel intersection void (I) and the sinusoidal channel (S) of MFI. Dotted lines are provided to guide the eye.

Table 2. Non-dispersive (Q_{nd}(DME)) and dispersive (Q_{vdw}(DME)) portions of DFT-derived DME adsorption energies (Q(DME) = Q_{nd}(DME) + Q_{vdw}(DME)) compared with first-order CH_3OH dehydration rate constants at 433 K.

Zeolite	k_{first} **/ 10^{-3} (mol DME) (kPa·mol H^+·s)$^{-1}$**	**Q_{nd}(DME)[a] / kJ mol^{-1}**	**Q_{vdw}(DME)[a] / kJ mol^{-1}**	**Q(DME)[a] / kJ mol^{-1}**
CD-FAU	0.49 ± 0.04	47	37	84
BEA	3.5 ± 0.7	53	63	116
MOR-1	5 ± 1	11	67	78
MOR-2	6 ± 1	11	67	78
MFI-I	4.2 ± 0.6	78	64	143
MFI-S	12 ± 2	39	81	120
MTT	3.1 ± 0.5	113	75	188

[a] Calculated with the vdW-DF2 functional.[30]

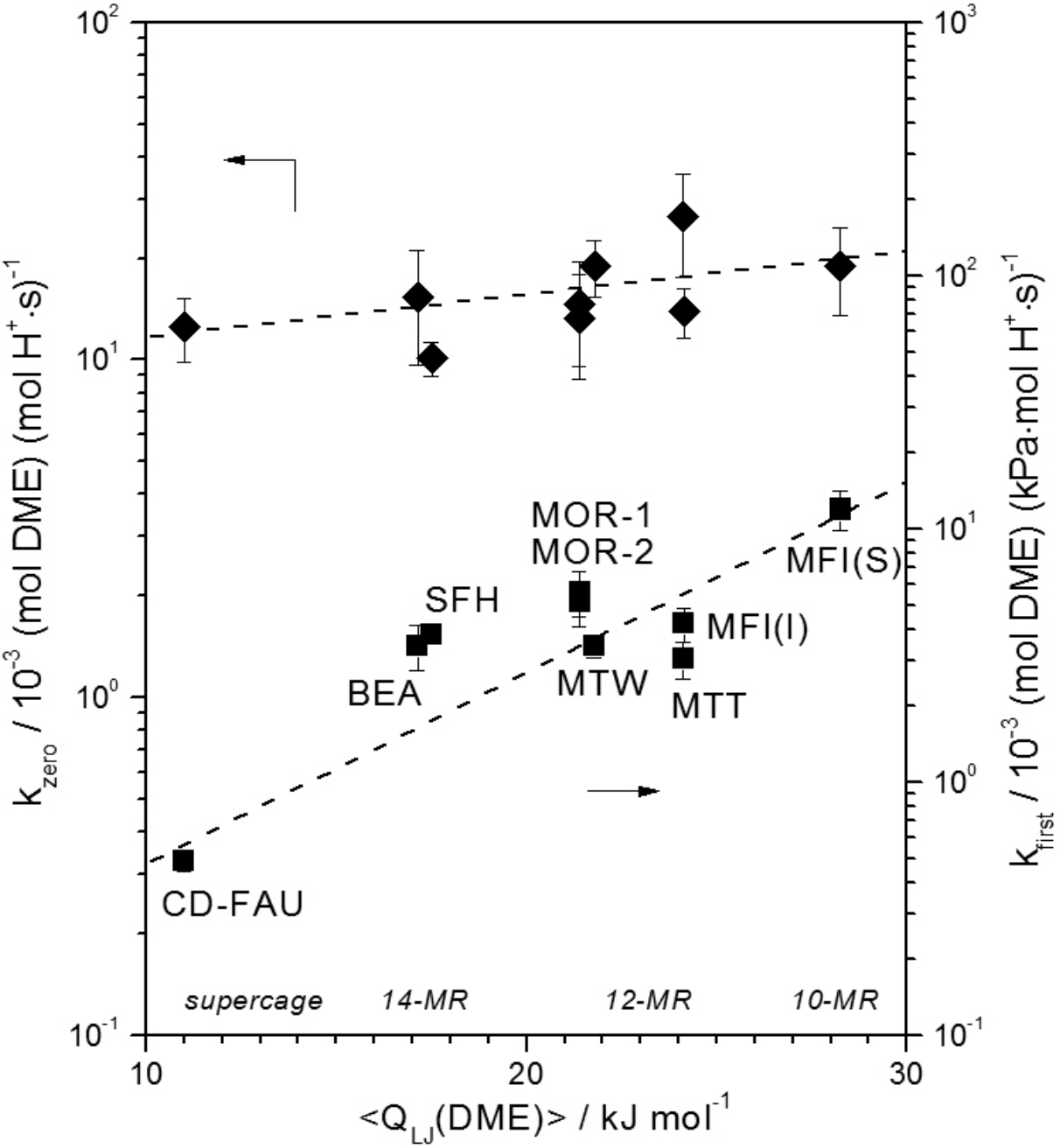

Fig. 7. CH_3OH dehydration rate constants at 433 K as a function of reaction averaged (Eq. (1)) DME van der Waals interaction energies (433 K) calculated with Lennard-Jones potentials[41] at all accessible H^+ in FAU, BEA, SFH, MTW, MTT, MOR, and MFI (MFI(S)), and for DME located in H^+ in the channel intersection void of MFI (MFI(I)). Dotted lines are provided to guide the eye.

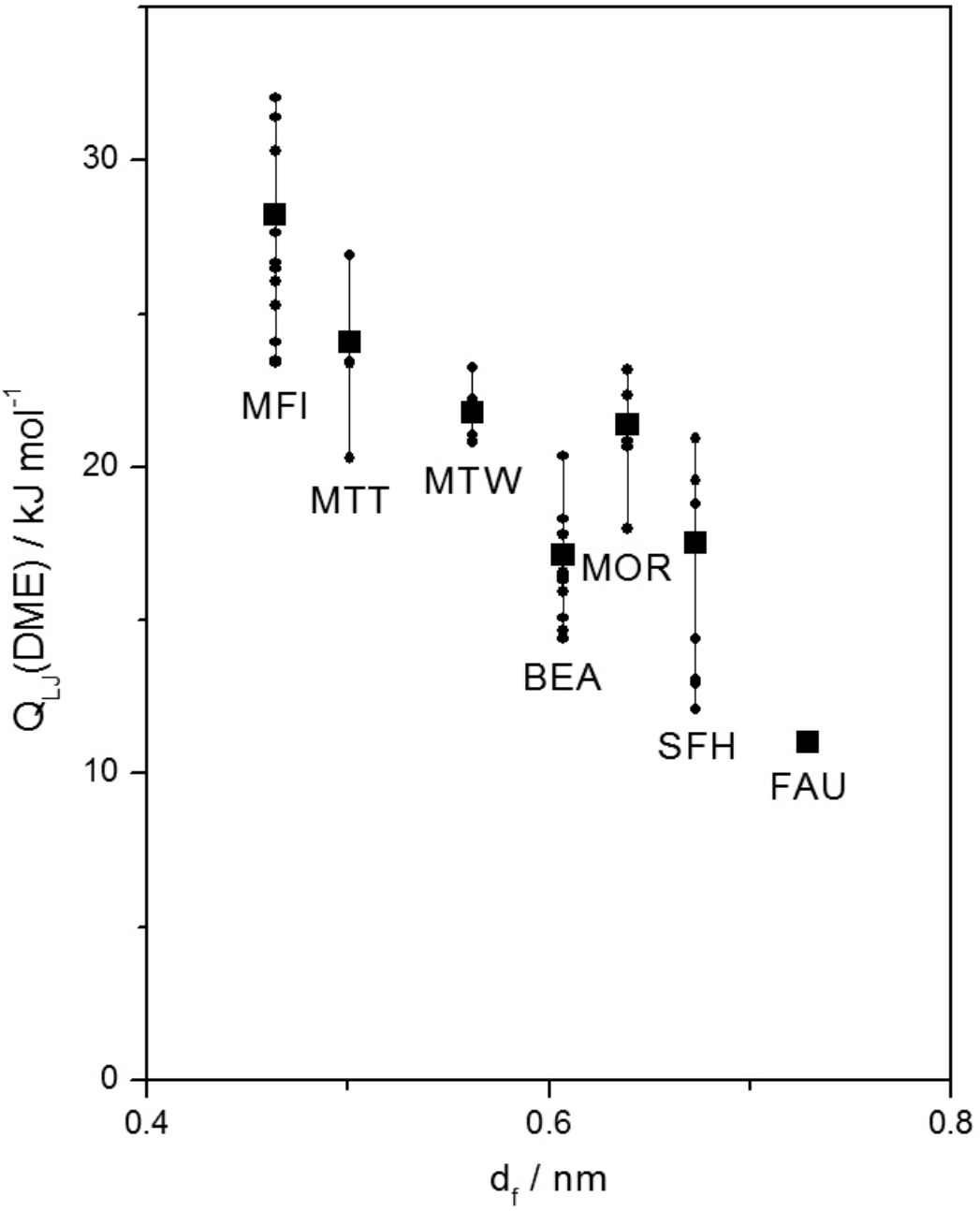

Fig. 8. DME van der Waals adsorption energies calculated at all accessible protons (●) and their reaction average (433 K; Eq. (1); ■) plotted against largest free sphere diameters (d_f).[7]

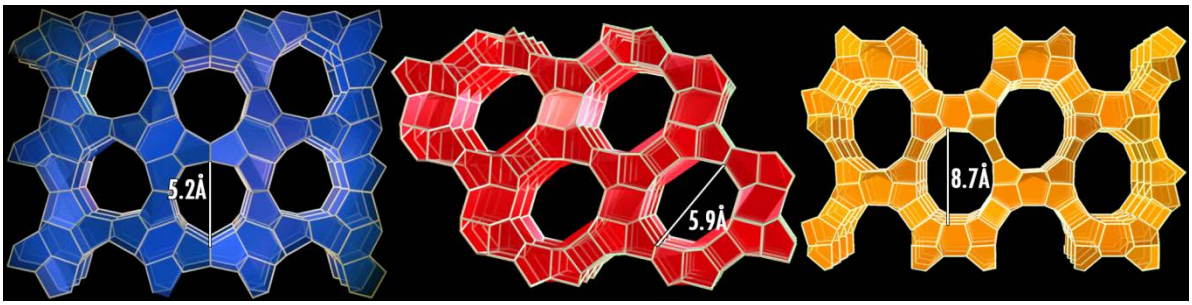

Fig. 9. Depiction of one-dimensional channels in MTT, MTW and SFH zeolites (left to right).

References

[1] E.G. Derouane, J. Catal. 100 (1986) 541-544.
[2] R. Gounder, and E. Iglesia, Chem. Commun. 49 (2013) 3491-3509.
[3] A. Bhan, R. Gounder, J. Macht, and E. Iglesia, J. Catal. 253 (2008) 221-224.
[4] R. Gounder, and E. Iglesia, Angew. Chem. Int. Ed. 49 (2010) 808-811.
[5] R. Gounder, and E. Iglesia, Acc. Chem. Res. 45 (2012) 229-238.
[6] B. Xu, C. Sievers, S.B. Hong, R. Prins, and J.A. van Bokhoven, J. Catal. 244 (2006) 163-168.
[7] M.D. Foster, I. Rivin, M.M.J. Treacy, and O.D. Friedrichs, Micropor. Mesopor. Mater. 90 (2006) 32-38.
[8] G. Sastre, V. Fornes, and A. Corma, J. Phys. Chem. B 106 (2002) 701-708.
[9] J. Dědeček, Z. Sobalík, and B. Wichterlová, Catalysis Reviews 54 (2012) 135-223.
[10] R.J. Gorte, Catal. Lett. 62 (1999) 1-13.
[11] A.J. Jones, R.T. Carr, S.I. Zones, and E. Iglesia, J. Catal. 312 (2014) 58-68.
[12] D.J. Parrillo, C. Lee, R.J. Gorte, D. White, and W.E. Farneth, The Journal of Physical Chemistry 99 (1995) 8745-8749.
[13] M. Brandle, and J. Sauer, J. Am. Chem. Soc. 120 (1998) 1556-1570.
[14] A.M. Rigby, G.J. Kramer, and R.A. vanSanten, J. Catal. 170 (1997) 1-10.
[15] E.G. Derouane, Micropor. Mesopor. Mater. 104 (2007) 46-51.
[16] R.T. Carr, M. Neurock, and E. Iglesia, J. Catal. 278 (2011) 78-93.
[17] R. Gounder, A.J. Jones, R.T. Carr, and E. Iglesia, J. Catal. 286 (2012) 214-223.
[18] G.W. Skeels, and D.W. Breck. 1987. Silicon substituted Y zeolite composition LZ-210. U.S. Patent Number 4,711,770.
[19] A. Corma, V. Fornes, and F. Rey, Appl. Catal. 59 (1990) 267-274.
[20] S. Elomari. 2005. Hydrocarbon conversion using zeolite SSZ-53. USPTO, editor. Chevron U.S.A. Inc., United States. 26.
[21] S.I. Zones, A. Benin, S.-J. Hwang, D. Xie, S. Elomari, and M.-F. Hsieh, J. Am. Chem. Soc. 136 (2014) 1462-1471.
[22] R.F. Lobo, S.I. Zones, and R.C. Medrud, Chem. Mater. 8 (1996) 2409-2411.
[23] S.I. Zones, G. Zhang, K.R. Krishna, J.A. Biscardi, P. Marcantonio, and E. Vittoratos. 2008. Preparing small crystal SSZ-32 and its use in a hydrocarbon conversion process. Chevron U.S.A. Inc.
[24] S.I. Zones, Zeolites 9 (1989) 458-467.
[25] C.A. Emeis, J. Catal. 141 (1993) 347-354.
[26] G. Kresse, and J. Hafner, Physical Review B 47 (1993) 558-561.
[27] G. Kresse, and J. Furthmüller, Comput. Mater. Sci. 6 (1996) 15-50.
[28] G. Kresse, and J. Furthmüller, Physical Review B 54 (1996) 11169-11186.
[29] G. Kresse, and J. Hafner, Physical Review B 49 (1994) 14251-14269.
[30] K. Lee, É.D. Murray, L. Kong, B.I. Lundqvist, and D.C. Langreth, Physical Review B 82 (2010) 081101.
[31] E.a.D. Murray, K. Lee, and D.C. Langreth, J. Chem. Theory Comput. 5 (2009) 2754-2762.
[32] P.E. Blöchl, Physical Review B 50 (1994) 17953-17979.
[33] G. Kresse, and D. Joubert, Physical Review B 59 (1999) 1758-1775.
[34] H. Van Koningsveld, H. Van Bekkum, and J.C. Jansen, Acta Crystallographica Section B 43 (1987) 127-132.
[35] D.H. Olson, G.T. Kokotailo, S.L. Lawton, and W.M. Meier, J. Phys. Chem. 85 (1981) 2238-2243.
[36] C. Baerlocher, and L.B. McCusker. Database of Zeolite Structures.
[37] J.M. Newsam, M.M.J. Treacy, W.T. Koetsier, and C.B.D. Gruyter, Proceedings of the Royal Society of London. A. Mathematical and Physical Sciences 420 (1988) 375-405.
[38] Materials Studio, v. 6.0, (2011).

[39] B. Marler, C. Deroche, H. Gies, C.A. Fyfe, H. Grondey, G.T. Kokotailo, Y. Feng, S. Ernst, J. Weitkamp, and D.E. Cox, J. Appl. Crystallogr. 26 (1993) 636-644.
[40] B.A. De Moor, M.F. Reyniers, O.C. Gobin, J.A. Lercher, and G.B. Marin, J. Phys. Chem. C 115 (2011) 1204-1219.
[41] B.A. De Moor, M.-F.o. Reyniers, M. Sierka, J. Sauer, and G.B. Marin, The Journal of Physical Chemistry C 112 (2008) 11796-11812.
[42] T.F. Willems, C.H. Rycroft, M. Kazi, J.C. Meza, and M. Haranczyk, Micropor. Mesopor. Mater. 149 (2012) 134-141.
[43] M. Haranczyk. Zeo++.
[44] R.J. Madon, and E. Iglesia, J. Mol. Catal. A: Chem. 163 (2000) 189-204.
[45] C.D. Baertsch, K.T. Komala, Y.H. Chua, and E. Iglesia, J. Catal. 205 (2002) 44-57.
[46] E.P.L. Hunter, and S.G. Lias, J. Phys. Chem. Ref. Data 27 (1998) 413-656.
[47] R.M. Ravenelle, F. Schüβler, A. D'Amico, N. Danilina, J.A. van Bokhoven, J.A. Lercher, C.W. Jones, and C. Sievers, The Journal of Physical Chemistry C 114 (2010) 19582-19595.
[48] B. Xu, F. Rotunno, S. Bordiga, R. Prins, and J.A. van Bokhoven, J. Catal. 241 (2006) 66-73.
[49] E. Bourgeat-Lami, P. Massiani, F. Di Renzo, P. Espiau, F. Fajula, and T. Des Courières, Appl. Catal. 72 (1991) 139-152.
[50] A. Zecchina, S. Bordiga, G. Spoto, D. Scarano, G. Spano, and F. Geobaldo, Journal of the Chemical Society-Faraday Transactions 92 (1996) 4863-4875.
[51] C.E. Ramachandran, B.A. Williams, J.A. van Bokhoven, and J.T. Miller, J. Catal. 233 (2005) 100-108.
[52] U. Eichler, M. Brandle, and J. Sauer, J. Phys. Chem. B 101 (1997) 10035-10050.
[53] J.B. Higgins, R.B. LaPierre, J.L. Schlenker, A.C. Rohrman, J.D. Wood, G.T. Kerr, and W.J. Rohrbaugh, Zeolites 8 (1988) 446-452.
[54] S. Sklenak, J. Dedecek, C. Li, B. Wichterlova, V. Gabova, M. Sierka, and J. Sauer, PCCP 11 (2009) 1237-1247.
[55] R. Pophale, P.A. Cheeseman, and M.W. Deem, PCCP 13 (2011) 12407-12412.

CHAPTER SIX

Representing and Characterizing the Diversity of Microporous Voids in Zeolite Frameworks

Abstract

Voids within crystalline microporous solids are represented here using stochastic distributions of rays placed and oriented randomly within the accessible void space, represented using Voronoi decompositions. This algorithm is provided in the Zeo++ software for open use. In this method, ray lengths are depicted as two-dimensional histograms that complement alternate descriptors, such as free and included sphere diameters. We illustrate the specific use of these methods as a tool to narrow the range of zeolites useful for a given catalytic application because of the shape and size of voids. DAC, AFS, AFY, SFO and EON zeolites contain void spaces similar, as suggested by Euclidean distance values between histograms, to those within MOR 8-MR side pockets, which stabilize the transition states that mediate dimethyl ether carbonylation to methyl acetate; these alternate structures offer different connecting void environments, which can enhance or restrict molecular access and influence the effectiveness of the 8-MR protons. NES, EON and USI zeolites exhibit histogram features similar to those of 12-MR MOR channels, where protons selectively catalyze alkylation of biphenyl and naphthalene to 4,4'-diisopropylbiphenyl and 2,6-diisopropylnaphthalene, respectively, with propene. SBT, FAU and SBS contain voids similar in topology to the 12-MR channels of LTL zeolites, within which Pt clusters remain active and stable during the dehydrocyclization of light alkanes, but without the one-dimensional nature of LTL channels. The approach and implementation of these methods are applicable to any microporous or mesoporous solids and to adsorption processes driven by van der Waals contacts between hosts and guest molecules.

1. Introduction

Zeolites have crystalline microporous frameworks with ordered channels, windows and cages 0.3-1.9 nm [1] in size. As catalytic materials, their narrow pore size distributions exclude molecules larger than their connecting channels and windows [2] and their small voids preferentially solvate certain transition states and reactants, giving rise to specific reactivity and shape selectivity [3-7]. Emerging protocols for the synthesis of solids with diverse pore topologies [1, 8] continue to increase the diversity of available frameworks, currently more than 190 [9], which represent, however, only a small fraction of the >500,000 thermodynamically feasible structures [10]. Such a breadth of distinct frameworks requires algorithms to describe and visualize their void spaces, so as to choose a specific zeolite structure for a given application in adsorption and catalysis [11].

The largest included sphere (D_i) and free sphere (d_f) diameters [12], determined using Delaunay triangulation of zeolite frameworks, provide single-valued descriptors of three-dimensional zeolite pores; they are currently provided in the web-based *International Zeolite Association Database (IZA)* [9]. These diameters define the largest spheres that can be contained in (D_i) or diffuse through (d_f) a given structure. More recently, the deconstruction of accessible pores into a collection of geometric shapes, such as spheres and cylinders [13], has proven useful

for inspecting pore environments; they yield a breadth of information, such as pore connectivities, volumes and surface areas. The corrugations and non-spherical void shapes, which may be important for solvation of non-spherical molecules, are not accurately represented by these methods. Hologram representations of zeolite voids based on Voronoi decompositions [14] provide another descriptor of zeolite voids, but it is unclear how the Voronoi node edge length, a measure of size, relates to the size scales relevant for the van der Waals interactions that matter for catalysis and adsorption processes. Methods that rely on the characterization or classification of frameworks [15, 16] focus on elementary building blocks of zeolites instead of the void spaces that they form and which carry significant consequences for adsorption and catalysis. More robust descriptors for the characterization and selection of zeolites as adsorbents and catalysts must include information about the void shape, size, corrugation and connectivity in a simpler and more interpretable and retrievable format.

Here, we present a new method to describe size and shape of voids and their non-uniform distributions in microporous solids. The emphasis is on zeolites and related inorganic solids, but the approach is generally applicable to porous solids. The algorithm determines the distribution of ray lengths in accessible void spaces resulting in a void space fingerprint that describes pore topologies in two-dimensions; it is similar but complementary to pore size distributions [17] and contains retrievable information about the surface texture, shape and size of void spaces. These ray-trace histograms are useful in visualizing and selecting microporous structures for specific catalytic and adsorption applications. Ray-trace calculations are implemented in the Zeo++ open-source suite of applications [18, 19]. We show here how histograms can be used to find zeolite structures with overall void spaces similar in shape, size and corrugation to those in MFI zeolites from IZA and Hypothetical zeolite databases using Euclidean distance metrics. The results of such a similarity search are used to examine the consequences of void environment on light alkane dehydrocyclization on Pt clusters in LTL, carbonylation of dimethyl ether by eight-member (8-MR) MOR pockets, and alkylation of naphthalene and biphenyl in 12-MR MOR channels, and in doing so to identify candidates with similar void spaces but different connectivity within the IZA zeolite structure databases.

2. Methods

2.1 Computation of ray lengths in zeolite voids

The ray trace algorithm utilizes Voronoi decomposition protocols implemented in the open-source program Zeo++ [18, 19] to provide the required void accessibility details based on spherical probes and framework atoms of user-specified size. The Voronoi decomposition is an efficient method to access detailed information about the void space geometry and topology, especially when compared with alternate grid-based approaches [20, 21]. In this study, the coordinates of framework atoms for 194 zeolite structures contained in the IZA database [9] and 139,396 hypothetical thermodynamically feasible zeolite structures (within +30 kJ mol^{-1} of Si α-quartz) [10] that are accessible to a free sphere of diameter 0.325 nm (e.g. CH_4) are used together with the van der Waals radii for O and Si atoms (0.152 and 0.210 nm, respectively, reported for zeolites [22]) to construct ray histograms for each microporous structure. Zeolite structures are imported into the Zeo++ program in crystallographic information file (CIF) formats. We refer to

all structures as zeolites in this work, although some are not currently available in their aluminosilicate form.

The Monte Carlo algorithm reported here places a point at a random position within a zeolite unit cell. Accessible volumes (V_a) and surface areas (SA_a) are determined as those that can be reached by the center of a spherical probe of diameter 0.1 nm. We consider such a probe to be large enough to exclude environments inaccessible to common molecules used as reactants, but small enough to accurately represent the relevant channel corrugations and texture. We examine two implementations that we denote as *constrained* and *unconstrained*. In the *constrained* approach, only ray origins that happen to be contained within V_a of the void structure are considered and rays are grown in a random direction until they intersect with the surface of a pore. This process is repeated in the opposite direction to define a ray that intersects the surface of a void at two points. Periodic boundary conditions are implemented with a defined cutoff length of 10 nm in order to terminate the infrequent rays that traverse through voids without encountering two intersections over 10 nm. In the *unconstrained* ray trace method, the starting point and direction of a ray within a unit cell are selected randomly without reference to the diameter of the probe. The intersection points of this ray with the surface of each pore that it crosses within a distance of 10 nm are recorded and are used to determine the lengths of rays contained within the entire internal volume. In both implementations, the length and number of rays are recorded and grouped in 1000 bins, each 0.01 nm wide, to create ray-trace histograms. Unless specified otherwise, histograms were created with 1,000,000 sample points for IZA zeolites and 100,000 sample points for hypothetical zeolites. The algorithm has been implemented within the Zeo++ software suite and is available online [19].

2.2 Algorithm for determining similarity among histograms

Similarities among ray histograms were determined using a Euclidean distance formula. This metric was selected because of its simplicity in logic and execution and of its sensitivity to the shape of histogram features, which contain details about the shape of the voids they represent, thus permitting pore topologies for different structures to be compared in detail. There are several other approaches to determine similarity and their comparison for various purposes is addressed elsewhere [17] and is beyond the scope of this study.

The Euclidean distance formula calculates the sum of the square of the differences between the probability density of rays of two samples in each bin i, for all bins:

$$S_{d,euc} = \sqrt{\sum_{i=1}^{n} \left(P_{1,i} - P_{2,i} \right)^2} \tag{1}$$

Here, $S_{d,euc}$ is the Euclidean distance defined for the two samples being compared (1 and 2), where $P_{j,i}$ is the probability density of rays in bin i for sample j, normalized so that the sum of the probability densities multiplied by the bin size, x, is unity.

$$1 = \sum_{i=1}^{n} P_{j,i} \cdot x \tag{2}$$

3. Results and discussion

3.1 Stochastic ray projections and their frequency in MFI

Figure 1 shows the density, location, and lengths of randomly placed and oriented rays in a MFI zeolite supercell using the *constrained* approach, in which ray origins are selected at random from the portion of the void structure accessible by a 0.1 nm sphere. Rays fill the sinusoidal and straight 10-MR channels of MFI, as well as the ellipsoidal voids created at their intersections (Figure 1), resulting in different ranges of ray lengths and distributions for each specific region within the void space. Higher densities of rays are present within larger pore volumes, because they have higher probabilities of containing ray origins and projections. Short rays (0-0.3 nm, Figure 1a) lie near the surface of the voids, where intersections of rays with the same pore surface are more frequent. The corrugations present in sinusoidal channels result in a higher density of short rays in their voids relative to straight channels. Rays with lengths between 0.3-0.6 nm (Figure 1b) intersect channels almost perpendicular to their direction and occur most frequently (Figure 2). Rays of 0.6-0.9 nm length (Figure 1c) are predominantly located within the voids formed by intersections of straight and sinusoidal channels. Rays longer than 1.2 nm (Figure 1d) traverse beyond channel intersections, but occur rarely (Figure 2). Thus, the collection of all rays describes the size of void environments because longer rays are present in larger volumes.

The ensemble of ray lengths can be converted into a histogram (Figure 2) to depict the unique pore topology of each zeolite in two-dimensions. In Figure 2, the frequencies of rays in MFI voids are shown as a function of their length such that the total area under the histogram is unity. In the case of MFI, rays with 0.40 nm length are most abundant, as shown by its prominent feature in the histogram. This feature is the result of a large number of rays that cross pores along their diameter (Figure 1b). We can compare this value to the channel diameters in MFI reported in the IZA database by increasing ray lengths by 0.134 nm to account for the differences between the van der Waals radii of the O-atoms (0.135 nm [12]) and the probe diameter used to determine accessible surface areas. The feature at 0.40 nm (adjusted to 0.53 nm) is consistent with the diameter of channels (0.51-0.56 nm; [9]); it appears at ray lengths slightly larger than the diameter of the largest sphere that can freely traverse MFI (0.446-0.470 nm; [9]). The breadth of this feature is affected by the shape of the pore, with more elliptical pores exhibiting somewhat more bimodal features (e.g., see MOR in Section 3.3) with the two radii of the ellipse given by the peak positions in the histogram. The shape is also affected by the presence of sinusoidal channels in MFI, which lead to a higher frequency of smaller rays and thus to another feature at shorter ray lengths.

The other feature in the ray-trace histogram of MFI (at 0.82 nm, Figure 2) arises from voids at channel intersections (Figure 1c). Weaker features are observed in the histogram for ray lengths beyond 0.82 nm and correspond to rays that extend beyond one unit cell (Figure 1d). Rays that extend beyond one unit cell traverse straight and sinusoidal channels with increasingly high probabilities of intersecting void surfaces reflected by the small area of these features in ray histograms.

The number, location and shape of peaks in a ray histogram are specific to each zeolite structure and correspond to specific void environments, such as channels and intersections in the

case of MFI. While ray histograms provide an easy method to represent, interpret and retrieve pore landscapes, the transformation of a three-dimensional ensemble of rays into a two-dimensional histogram results in a loss of information about the connectivity and asymmetry of voids. In addition, distinct void environments, when similar in size, can result in overlapping features in a ray histogram, such as the features from sinusoidal and straight channels in MFI. A natural extension of ray histograms would be to separate histograms for each distinct pore environment. For example, the ray histogram of MFI could be divided into contributions from rays contained within straight channels, sinusoidal channels and channel intersections. Yet, most zeolites contain a small number of unique void environments, which are either significantly different in size and would create unique histogram features or are similar enough in size that they would behave similarly in catalytic and adsorption processes.

Figure 2 compares the probability densities of rays found in MFI using the *unconstrained* and *constrained* methods. Both methods lead to histograms with peaks at 0.40 nm and 0.82 nm and thus represent channels and intersections with similar histogram features. The *unconstrained* method, however, has a larger fraction of rays shorter than 0.14 nm. These rays are predominantly located near the surfaces of voids and become less prominent in the *constrained* approach because the ray origins, which lie near the edges of accessible void spaces, occupy a smaller fraction of the void space and are therefore selected less frequently during sampling. Rays shorter than 0.14 nm do not describe features that are consequential for adsorption or catalysis because molecules of interest are typically larger than such volumes. This suggests that the *constrained* method is more appropriate for comparisons among samples and it is the method that we use in the rest of this study.

The average void environment for all zeolites in the IZA database [9] and the Hypothetical Zeolite Database [10] can be represented by the sum of the probability densities of rays for each zeolite. Figure 3a shows the results of this summation using the *constrained* method for MFI and for all zeolites in the two databases. The features in the IZA composite histogram contain three main differences from the MFI histogram: (1) a bimodal feature clustered ~0.1 nm around the MFI channel diameters (0.28-0.50 nm), (2) no distinguishable features above 0.40 nm, and (3) a slight feature at 0.06 nm. These differences suggest that IZA zeolites contain voids that are similar in size to MFI but with a bimodal distribution most likely corresponding to 8-MR and 10-MR channels. This is consistent with the scarcity of single structures larger than 0.8 nm and a nearly bimodal distribution of largest free sphere diameters [13]. Figures 3b and 3c show the position of the largest feature in ray histograms compared with the diameter of the largest included and free spheres calculated using similar parameters with the Zeo++ program for zeolites in the IZA and hypothetical databases, respectively. A large fraction of zeolite frameworks have a similar feature position and sphere diameter, as indicated by their proximity to the parity line, indicating that ray histogram peak positions are similar to sphere diameters as concluded previously for MFI. Sphere diameters and ray peaks cluster in two distinct regions around 0.40 nm for IZA zeolites (Figure 3b) consistent with the composite histogram in Figure 3a and the interpretation that 8-MR and 10-MR channels dominate voids in IZA zeolites. Zeolites far from the parity line (Figure 3b) result when the largest sphere diameter is not representative of the void space with the largest fraction of void volume, because the largest histogram feature contains, by definition, the largest frequency of rays, which are selected at random from the void space and thus occur more frequently in larger volumes.

The ray-average void size of zeolites contained in the Hypothetical Zeolite Database is 0.14 nm smaller than the channels in MFI (Figure 3a), even though these zeolites were screened for accessibility to a CH_4 probe. This is also apparent from the large density of hypothetical zeolites with largest features around 0.26 nm in Figure 3c. Smaller pores occur concurrently with larger atom densities in the unit cells (higher framework densities), which are thermodynamically more stable, consistent with the abundance of structures with ~0.26 nm size in stable zeolites. The small number of outliers from the parity line in Figure 3c suggest that for the majority of hypothetical zeolites, voids with the largest volume fraction (represented by the largest feature in ray histograms) represent the same voids as those probed with the largest free sphere diameter; this is probably due to a high prevalence of channels because cage-window structures would lead to smaller free sphere diameters than largest ray histogram features.

3.2 Finding zeolites with similar structural features as MFI

The previous section illustrates how ray histograms describe pore environments and resolve void features important for adsorption and catalysis. Next, we show how ray histograms can be compared to identify zeolites with pore and void characteristics similar to one another. As an example, structures in the IZA database [9] are compared with MFI by computing the Euclidean distance between their individual histograms and that for MFI. The Euclidean distance value allows relative similarity comparisons for various structures with a given structure (e.g. TER and STW each with respect to MFI) but its magnitude is arbitrary unless appropriately normalized by the difference between the maximum and minimum Euclidean distances amongst all zeolites in a search set. This normalization, however, is not required for the determination of similar voids that is the focus of this study; the comparison of absolute similarity is discussed in detail in another study [17].

Table 1 lists the Euclidean distance for the most and least similar zeolites to MFI, when all features smaller than 5.0 nm are included in ray histograms, along with largest sphere diameters, dimensionalities and largest ring sizes. TER (intersecting straight and sinusoidal 10-MR channels with cage-like intersections), STW (tortuous 10-MR channels with cage-like voids on the side of channels) and SVR (intersecting tortuous 10-MR channels) zeolites emerge as void structures most similar to MFI. The histograms and void structures of these three zeolites and MFI are shown in Figures 4 and 5, respectively. The structures all have 10-MR channels, but their similarity is not readily apparent from a visual inspection of their voids, as represented in Figure 5, because the voids do not have the same straight and sinusoidal channels and intersections present in MFI. A recent study showed that the isosteric heats of adsorption of CO_2 are similar for Na^+-MFI and Na^+-SVR zeolites [23] suggesting that their pore environments may indeed be similar for this specific practical purpose, consistent with their similar ray histograms.

The histogram for TER (Figure 4) resembles that for MFI both visually and in its Euclidean distance ($S_{d,euc}$ = 0.129), which is the smallest among IZA zeolites. Features at 0.81 and 1.17 nm are present in both MFI and TER histograms (Figure 4), suggesting that the distances between larger voids (those represented by a peak at 0.81 nm) are similar in these two structures; indeed the distances between channel intersections in both MFI and TER are separated by ~1.0 nm.

STW and SVR do not contain intersecting straight and sinusoidal channels, while MFI and TER do; yet, all four samples give similar histograms, suggesting that their voids are similar in shape and size. STW and SVR contain tortuous channels and cage-like voids of similar size to the channel intersections in MFI, based on the ray histograms. This is not evident by visual inspection of the tortuous channels in STW and SVR (Figure 5) or from their included or free sphere diameters (Table 1), which would predict that channels and intersection sizes differ by as much as 0.1 nm between STW and MFI (largest included sphere diameters of 0.543 and 0.636 nm, respectively). Included and free sphere diameters are not suitable for this comparison because spherical models do not accurately represent the shape of channels and intersections in STW and SVR. In contrast, details of any arbitrary shape are present within the ray-trace histogram features, for example the ellipsoidal channel intersections in MFI show a broad feature at 0.81 nm and the ellipsoidal side-pockets in MOR show a bimodal feature (see Section 3.3.1).

The similar void sizes and shapes of MFI, TER, STW and SVR voids and channels suggest that reactants and transition states will be stabilized similarly by van der Waals interactions in these voids, which can have large consequences on catalytic reactivity [5]; but, their different pore connectivities, orientations and tortuosities would have significant consequences for diffusional access. Thus, the similarity of structures from ray histogram metrics can narrow the selection of potential candidate structures for catalytic or adsorption evaluation.

Next, we examine the differences between ray histograms and the range of Euclidean distances between MFI and other structures. Euclidean distance values of MFI with respect to IZA zeolites extend from 0.129 to 0.439 (see Supporting Information) and differ in magnitude for each zeolite, except for BEC and ISV, which give a Euclidean distance of 0.262. A similarity test between BEC and ISV shows that the histograms are indeed similar ($S_{d,euc}$ = 0.098), but not identical, which would result in a distance value of zero. We infer that histograms for each zeolite in the IZA database contain a unique distribution of features and thus histograms provide a fingerprint of the void environment of each zeolite. The least similar zeolites to MFI include BCT, LIT and VSV with Euclidean distance values of 0.377, 0.411 and 0.439, respectively. These samples contain small 8-MR channel structures that are very different from 10-MR channels in shape and size, consistent with their large Euclidean distances.

The abbreviated results of a similarity search between MFI and ~140,000 hypothetical zeolites are included in the Supporting Information. The frameworks identified in the search are inaccessible to current synthetic protocols, however, they demonstrate how zeolite framework selection could be accomplished with ray histograms when synthetic hurdles are overcome.

3.3 The use of ray-trace histograms and similarity metrics to select void structures for specific purposes

This section demonstrates, using three illustrative examples, how ray histograms can be used to find candidate catalytic solids that can stabilize specific transition states with high selectivity via similarity searches. The concept that voids and channels can solvate reactants and transition states through van der Waals interactions and that, in doing so, can influence reactivity or selectivity is widely accepted and exploited in the practice of zeolite catalysis [1, 24]. For example, n-pentane cracking turnover rates vary over a range of 10^3 with pore size for zeolites

with pores that vary by 0.2 nm [5]. Many studies have reported the ubiquitous stabilization of transition states and reactants via van der Waals stabilization [2, 25-29].

3.3.1 Selective Carbonylation of Dimethyl Ether to Methyl Acetate

The carbonylation of dimethyl ether (DME) to methyl acetate occurs selectively at bound methyl groups located within 8-MR side pockets in MOR or 8-MR channels of FER; turnover rates are not detectable at sites within 10-MR or 12-MR channels or in cages or channel intersections of MFI, BEA or FAU [30]. Theoretical treatments have recently suggested that the shape of 8-MR side pockets in MOR and the relative orientation of the methyl are responsible for the increase in selectivity to carbonylation [31]. Alternate and possibly better carbonylation catalysts would contain 8-MR pockets or channels similar in size *and* shape to 8-MR side pockets in MOR, but connected via multi-dimensional larger channels to allow molecular flow. The shape and size of 8-MR side pockets in MOR are represented by a histogram feature between 0.12 and 0.46 nm in Figure 6, which can be used in a ray histogram similarity search to find other zeolites with similar voids. A selection of zeolite frameworks determined from a similarity search for ray histograms with features similar to those in MOR in the region between 0.12 and 0.46 nm are summarized in the top portion of Table 2 with their ray histograms compared in Figure 6. DAC (10-MR straight channels with 8-MR void windows that connect these channels) emerges as the IZA zeolite with the most similar side pockets to those in MOR, but its 10-MR connecting channels are smaller than channels in MOR and may impose diffusional constraints. These possible transport restrictions can be avoided by probing the most similar zeolites to choose those with free sphere diameters larger than 0.55 nm [12]; the four resulting zeolites within the ten most similar are AFS, AFY, SFO and EON (Table 2). The shape and size of the 8-MR voids in these samples should cause any H^+ (and the CH_3 groups that replace them) to exhibit the transition state stabilization that confers high DME carbonylation reactivity to 8-MR side pockets in MOR. We note that AFS, AFY, and SFO are not currently available as aluminosilicates and therefore H^+, when present in their voids, may differ in acid strength and reactivity from H^+ species in MOR. The EON structure (Table 2) is of particular interest because its 8-MR channels connect parallel 12-MR channels, in contrast with the dead-end nature of the MOR side pockets; this feature may allow faster diffusion within the micropore structure. As this example indicates, these similarity metrics based on ray histograms can focus the synthesis and catalytic evaluation efforts on the most promising structures in both IZA and hypothetical databases of zeolites and also allow the testing of competing hypotheses to account for the reactivity of specific structures.

3.3.2 Isopropylation of Biphenyl and Naphthalene by Large-Pore Zeolites

Next, we search for zeolites with voids similar to the 12-MR channels of MOR, which are selective for isopropylation of biphenyl and naphthalene to 4,4'-diisopropylbiphenyl and 2,6-diisopropylnaphthalene, respectively [32-34]. Rays between 0.47-2.0 nm in ray histograms are contained within 12-MR channels of MOR; thus, a similarity search using this histogram feature may identify zeolites with similar void shape and size to these channels. Table 2 shows the resulting three zeolite frameworks from this similarity search (NES, EON, USI) and compares their Euclidean distances from 12-MR MOR, as well as their largest sphere diameters, dimensionalities, and largest ring sizes.

NES (intersecting 10-MR straight and sinusoidal channels) shows the smallest Euclidean distance ($S_{d,euc}$ = 0.124) from 12-MR MOR channels, in spite of the exclusive presence of 10-MR windows; this reflects the sinusoidal shape of these NES channels, which create local voids larger than expected from its cylindrical 10-MR structure. In this case, the window size and largest sphere descriptors would have led to an incorrect conclusion of dissimilarity with MOR channels (e.g., the largest included sphere diameters of MOR and NES are 1.0 and 0.70 nm, respectively). EON emerges as a zeolite with similar 12-MR channels as MOR and, as discussed in Section 3.3.1, also contains voids similar to the side pockets in MOR. The similarity of shape and size of both void environments in EON and MOR make EON a particularly interesting case also for comparisons of DME carbonylation reactivity.

We consider last USI zeolites (intersecting 10-MR and 12-MR channels) with 12-MR channels similar in shape and size to MFI, but also containing intersecting 10-MR channels that create a void that is slightly larger than in 12-MR MOR channels and which are likely to increase the rate of formation of the less desirable di-isopropyl bulkier isomers [32]. This illustrates how similarity searches based on ray histograms can identify similar voids but often require further interrogation when the connectivity of voids becomes important. These examples demonstrate that ray histograms often lead to frameworks that are non-obviously similar from largest sphere diameters metrics (Table 2). Similarity searches with ray histograms can greatly reduce the analysis time and increase the accuracy of structure comparisons compared with searches based on sphere diameter descriptors or visual inspections of frameworks. In this case, the method is able to identify a handful of structures as promising candidates for the selective isopropylation of biphenyl and naphthalene to their least bulky products.

3.3.3 Determining the Mechanism for Stabilization of Pt in LTL

Next, we examine how ray histograms can be used to discriminate among structures based on long range void shapes, such as the undulating channel constrictions present in LTL. Pt clusters within LTL (one-dimensional 12-MR channels) zeolites have been used for dehydrocyclization of C_6-C_9 alkanes to form arenes [35-39]; the unique reactivity of these clusters has been ascribed to inhibition of oligomerization reactions, which lead to unreactive carbon residues, by the one-dimensional nature of LTL channels [35, 40, 41]. It is unclear whether the one-dimensional nature or the size and shape of the channels are responsible for the protection of the encapsulated Pt clusters. Structures with channels of similar size and shape but interconnected in two or three dimensions would allow us to discern the relative contributions of connectivity and local structure to inhibited deactivation.

We have calculated Euclidean distance statistics between ray histograms for LTL and other frameworks in the IZA database for rays 0.5-1.2 nm long, which represent the portion of the histograms describing the channel structure of LTL. SBT (intersecting 12-MR channels with large cages), FAU (large cages connected by 12-MR windows), and SBS (intersection 12-MR sinusoidal and straight channels with large cages) are identified as structures with voids most similar to the undulating channels in LTL (Table 3). Figure 7 displays the ray histograms for LTL, SBT, FAU and SBS, and demonstrates the similarity in feature shape and position between these zeolites. The pore systems in SBT, FAU and SBS also constrict and open to cage-like voids

with included sphere diameters of 1.00-1.15 nm, but with three-dimensional networks absent in LTL. This void three-dimensionality can shed light on the structural basis for the stabilization of Pt clusters within LTL channels. Dealuminated FAU zeolites have been shown to mitigate deactivation of confined Pt clusters more than clusters of equivalent size on mesoporous SiO_2, but not to the same extent as LTL [40]. These results support the hypothesis that the connectivity differences between FAU and LTL are responsible for their stability differences, because local "containers" for Pt clusters are similar in the two samples based on their similar ray histograms.

A search for structures similar to LTL based on the closest free or included sphere diameters identifies structures (ETR, UFI, LTN, MAZ, AFI, and AET) with a wide variety of largest pore openings (8-18 MR) and void networks with entirely straight channels or cages connected by 8-MR windows (Table 3). Structures with 8-MR windows (UFI and LTN) are impractical because such windows prevent access and egress of reactants and products. Structures with larger windows (ETR, MAZ, AFI, and AET) lack the shape of pores found in LTL which may be important for the stabilization of Pt and could explain why Pt contained in 12-MR channels of MOR are not stable [42]. Thus, included and free sphere diameters are useful for describing pore size for spherical cages or straight channels but they neglect the shape that many zeolite voids exhibit, which ray histograms capture and which are likely to be consequential for catalysis.

The identification of zeolites with voids similar to the 10-MR channels and intersections in MFI, the 8-MR side pockets and 12-MR channels in MOR, and the 12-MR channels in LTL demonstrate the ability of ray histograms to distinguish and select void environments with catalytic consequences because of their shape and size, but with potentially different void connections. Euclidean distance metrics provide a straightforward method for the comparison of histogram features and, therefore, the voids that they represent, providing a narrow selection of zeolites with potential catalytic applications. These tools complement existing void descriptors, such as inscribed and free sphere diameters, by describing void shape instead of just size and allow for the evaluation of specific void features from large databases of structures.

4. Conclusions

A method is presented for the characterization and comparison of zeolite voids through the Monte Carlo sampling of rays in accessible volumes of microporous structures. Ensembles of rays are represented by two-dimensional ray histograms, which encode the details of pore shapes, sizes and distributions in complex void networks. Ray histograms complement previous descriptors of void space such as largest free and included sphere diameters, largest ring openings and accessible surface areas and volumes, by describing void shape instead of just size and by describing the distribution of void environments within a zeolite. We demonstrate with illustrative examples how ray histograms describe the unique pore environments of MFI, MOR and LTL, and utilize the features present in their histograms to find structures in IZA and Hypothetical Zeolites Databases with similar catalytically relevant voids using a simple Euclidean distance similarity metric. The algorithm determines void similarities amongst large databases of nearly 140,000 hypothetical and existing zeolite frameworks on the order of minutes with specificity to void sizes and shapes which matter for the van der Waals stabilization of reactants and transition states in microporous solid catalysts. Zeolite frameworks that contain voids similar to the 8-MR pockets in MOR (DAC, AFS, AFY, SFO and EON), which are

selective for the carbonylation of DME to methyl acetate, and the 12-MR channels in MOR (NES, EON, and USI), which are selective for the isopropylation of biphenyl and naphthalene to their least bulky products, are presented as potential catalytic materials.

Ray histograms and the Euclidean distances outlined here provide a tool to narrow the discovery of catalytically relevant materials with enhanced reactivity, which will ultimately depend on the connectivity of voids and the location of H^+ within them. The ray-trace code is applicable to a wide variety of porous materials and is included in the Zeo++ software for open use [18]. Histograms for zeolites from the IZA and Hypothetical Databases are also available publicly on the web [19].

Acknowledgements

I acknowledge Maciej Haranczyk (LBNL) and Christopher Oustrouchov (LBNL) for their technical expertise and Dr. Stacey I. Zones (Chevron) for helpful technical discussions. Financial support from the Chevron Energy Technology Company and the National Science Foundation are also gratefully acknowledged. The technical editing of Dr. George D. Meitzner is gratefully acknowledged.

Figures, Tables and Schemes

Table 1. Summary of structures most (dis)similar to MFI determined from ray histograms.

Structure	$S_{d,euc}$[a]	D_i (nm)[b]	d_f (nm)[b]	Dimensionality	Largest ring size
MFI	*0.000*	*0.636*	*0.470*	*3*	*10*
TER	0.129	0.694	0.516	2	10
STW	0.135	0.543	0.488	3	10
SVR	0.137	0.585	0.465	3	10
BCT	0.377	0.380	0.291	1	8
LIT	0.411	0.324	0.181	0	8
VSV	0.439	0.294	0.197	3	9
Average[c]	0.243	0.680	0.451	N/A	N/A

[a] Euclidean distance from MFI determined for rays between 0-5 nm
[b] Maximum included (D_i) and free sphere diameters (d_f) [9]
[c] Average values from zeolite structures in IZA database from [12]

Table 2. Summary of structures similar to 8-MR side pockets (DAC, AFS, AFY, SFO and EON) and 12-MR channels (NES, EON and USI) in MOR determined from ray histograms with ray lengths between 0.12-0.46 nm and 0.47-2.0 nm, respectively.

Structure	**$S_{d,euc}$[a]**	**D_i (nm)[b]**	**d_f (nm)[b]**	**Dimensionality**	**Largest ring size**
MOR	*0.000*	*1.001*	*0.750*	*1*	*12*
DAC	0.118	0.528	0.419	2	10
AFS	0.141	0.951	0.601	3	12
AFY	0.148	0.782	0.590	3	12
SFO	0.156	0.792	0.695	2	12
EON	0.157	0.783	0.679	2	12
NES	0.124	0.704	0.507	2	10
EON	0.139	0.783	0.679	2	12
USI	0.145	0.676	0.628	2	12
Average[c]	0.236	0.680	0.452	N/A	N/A

[a] Euclidean distance from MOR

[b] Maximum included (D_i) and free sphere diameters (d_f) [9]

[c] Average values from zeolite structures in IZA database from [12] for 8-MR side pocket similarity

Table 3. Summary of structures similar to LTL determined from ray histograms between 0.5-1.2 nm (SBT, FAU and SBS) and largest included sphere diameters (ETR, UFI and LTN).

Structure	$S_{d,euc}$[a]	D_i (nm)[b]	d_f (nm)[b]	Dimensionality	Largest ring size
LTL	*0.000*	*1.001*	*0.750*	*1*	*12*
SBT	0.129	1.117	0.734	3	12
FAU	0.139	1.124	0.735	3	12
SBS	0.147	1.145	0.727	3	12
ETR	0.206	1.005	0.933	3	18
UFI	0.209	1.009	0.389	2	8
LTN	0.315	1.013	0.208	0	8
Average[c]	0.329	0.680	0.452	N/A	N/A

[a] Euclidean distance from LTL

[b] Maximum included (D_i) and free sphere diameters (d_f) [9]

[c] Average values from zeolite structures in IZA database from [12] for 8-MR side pocket similarity

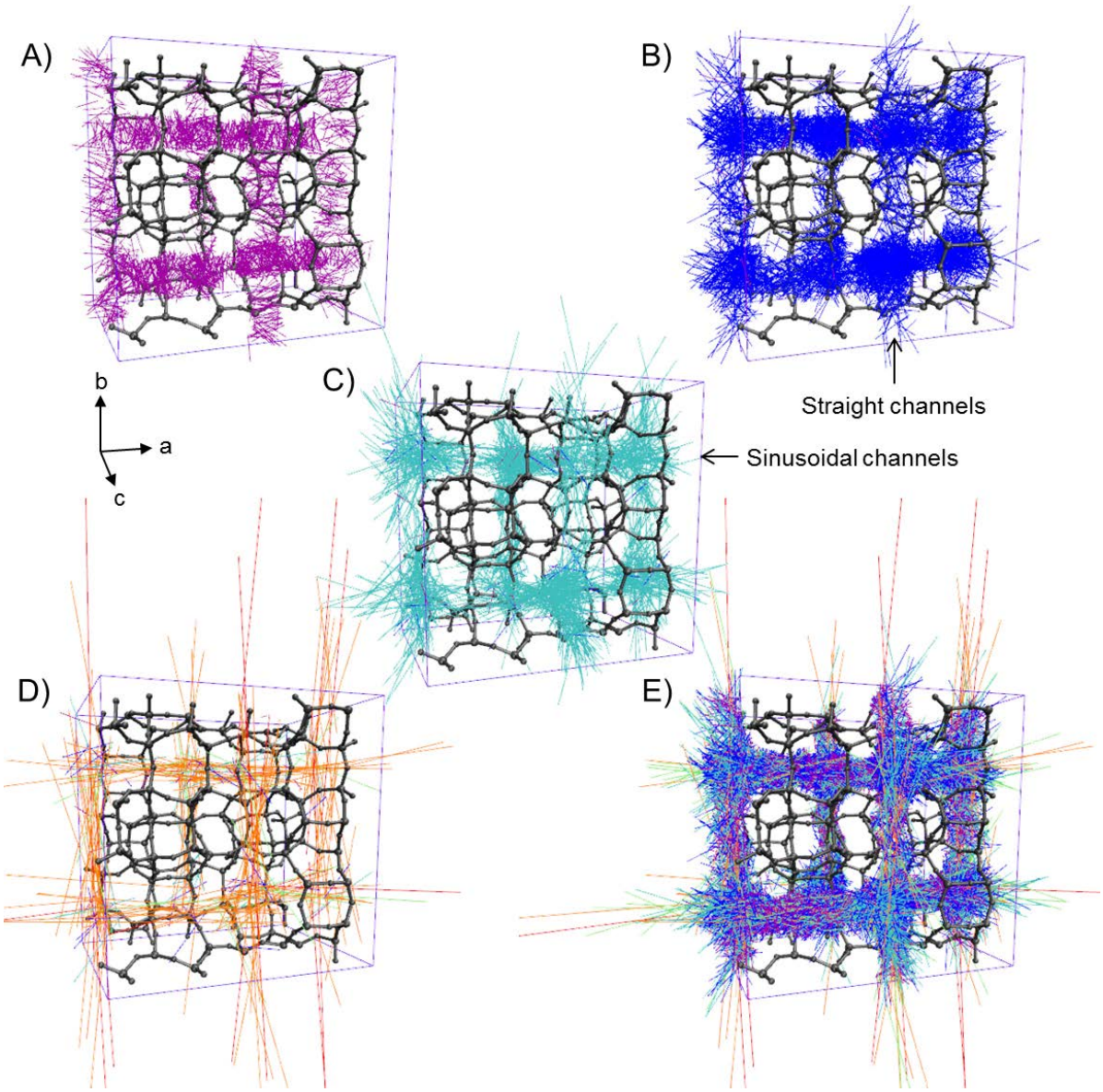

Fig. 1. Illustration of randomly placed and oriented rays using the *constrained* method in MFI with framework Si and O atoms added for clarity. Rays are displayed according to their length:, (a) 0-0.3 nm, (b) 0.3-0.6 nm, (c) 0.6-0.9 nm, (d) larger than 1.2 nm, and (e) 0-10 nm.

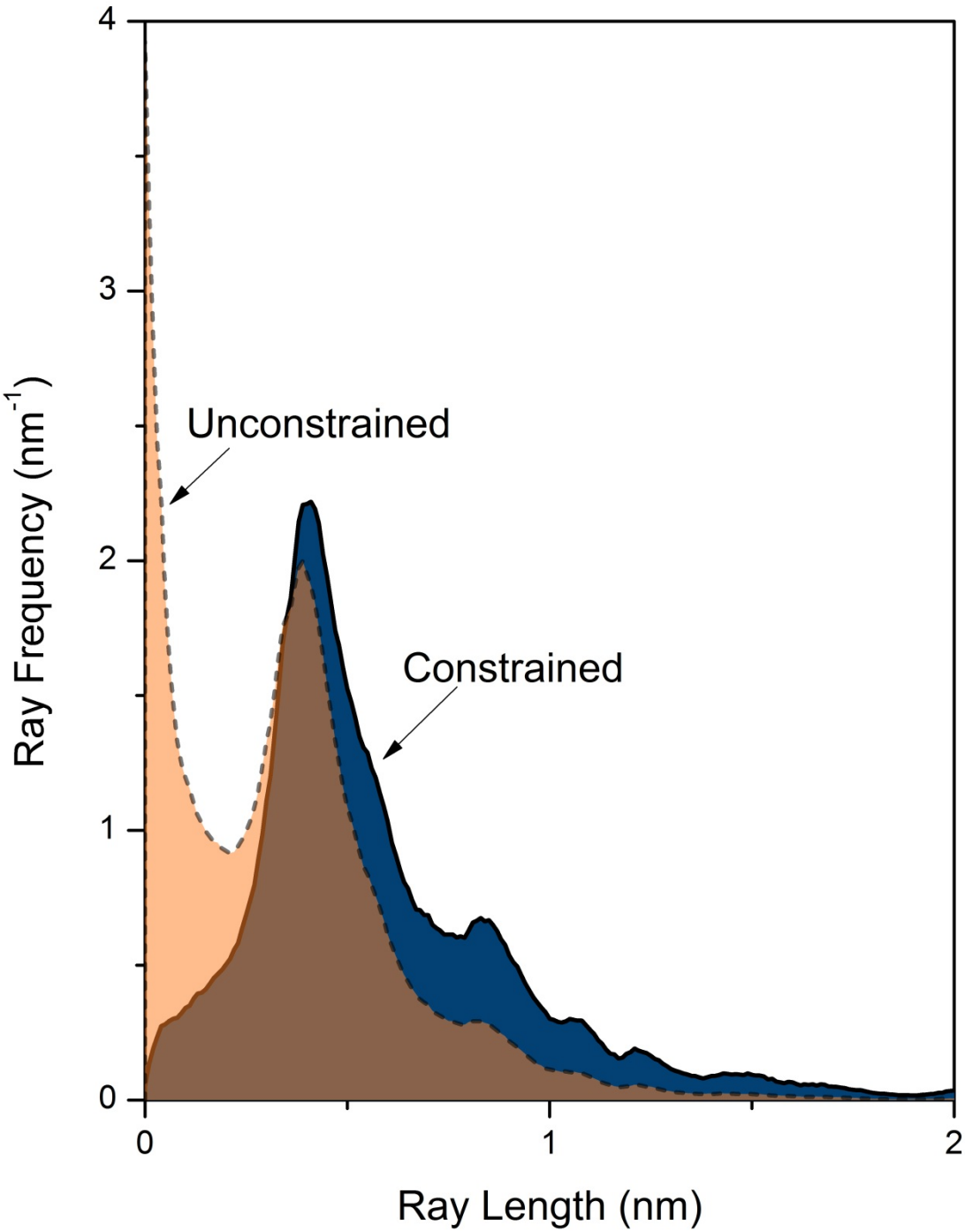

Fig. 2. Ray trace histograms normalized so that area under each curve is unity for MFI with 6.1 million rays placed randomly within the void structure using the *unconstrained* approach normalized (dotted line) and 2.1 million rays with the *constrained* approach (solid line).

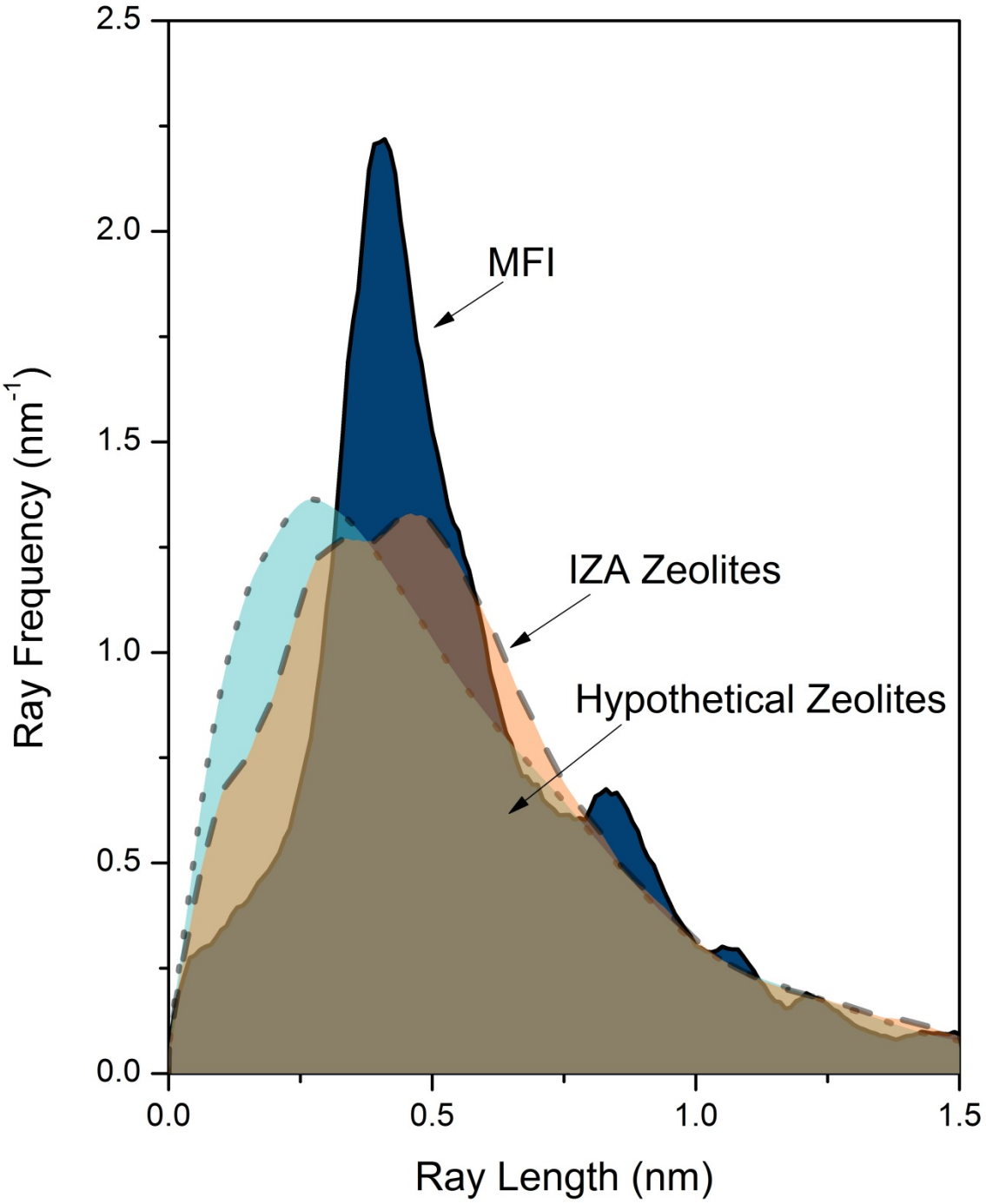

Fig. 3a. Ray trace histogram of MFI (blue; solid line), and the average of ray frequencies for IZA zeolites (red; dashed line) and hypothetical zeolites accessible to a spherical probe of 0.325 nm diameter (green; dotted line) using the *constrained* approach.

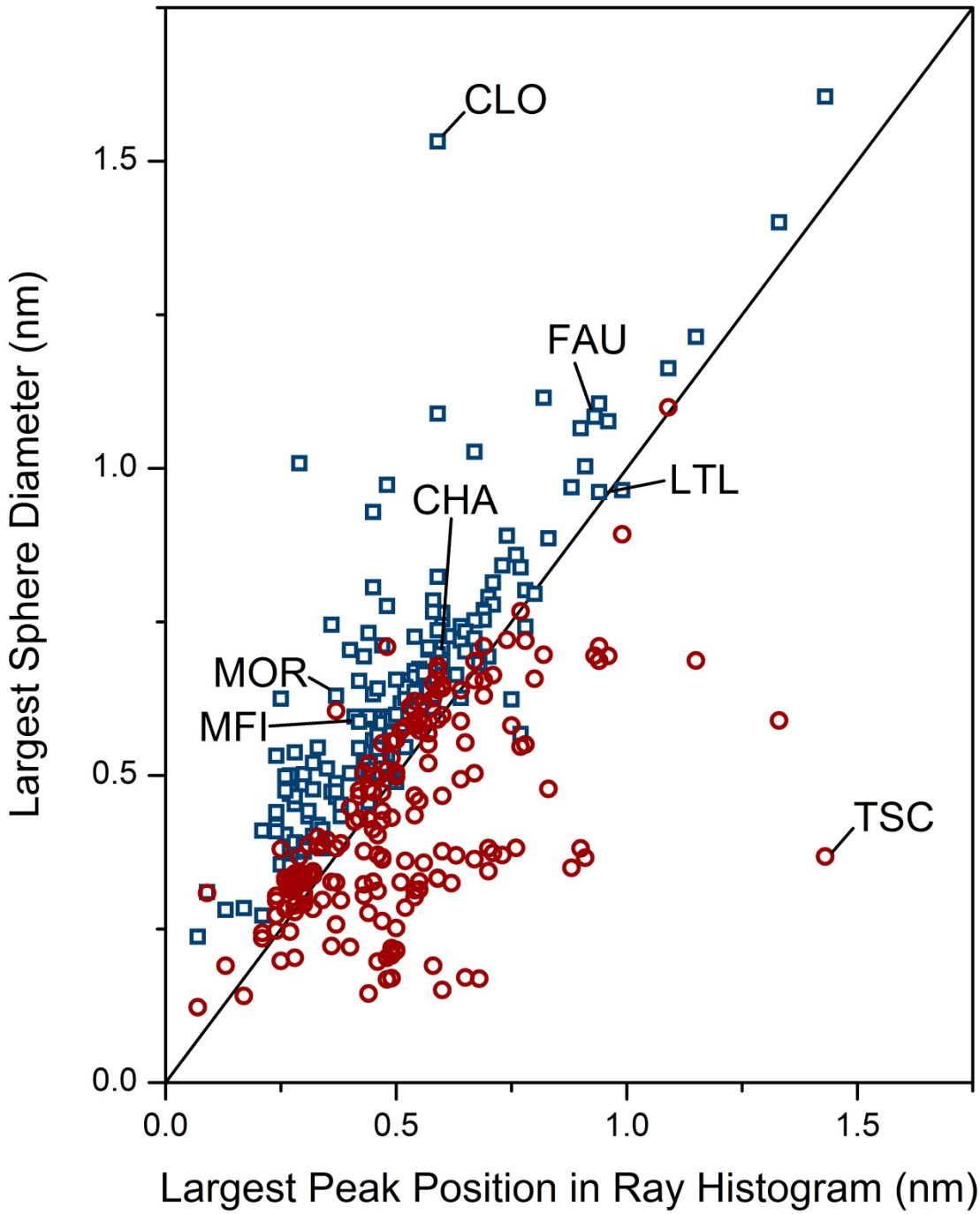

Fig. 3b. Comparison of largest free (red circle) and included (blue square) sphere diameters with the position of the largest feature in ray trace histograms for zeolites in the IZA database using the *constrained* approach calculated with Zeo++ using equivalent probe and van der Waals parameters. Outliers and some common zeolites are identified. Solid parity line is drawn to guide the eye.

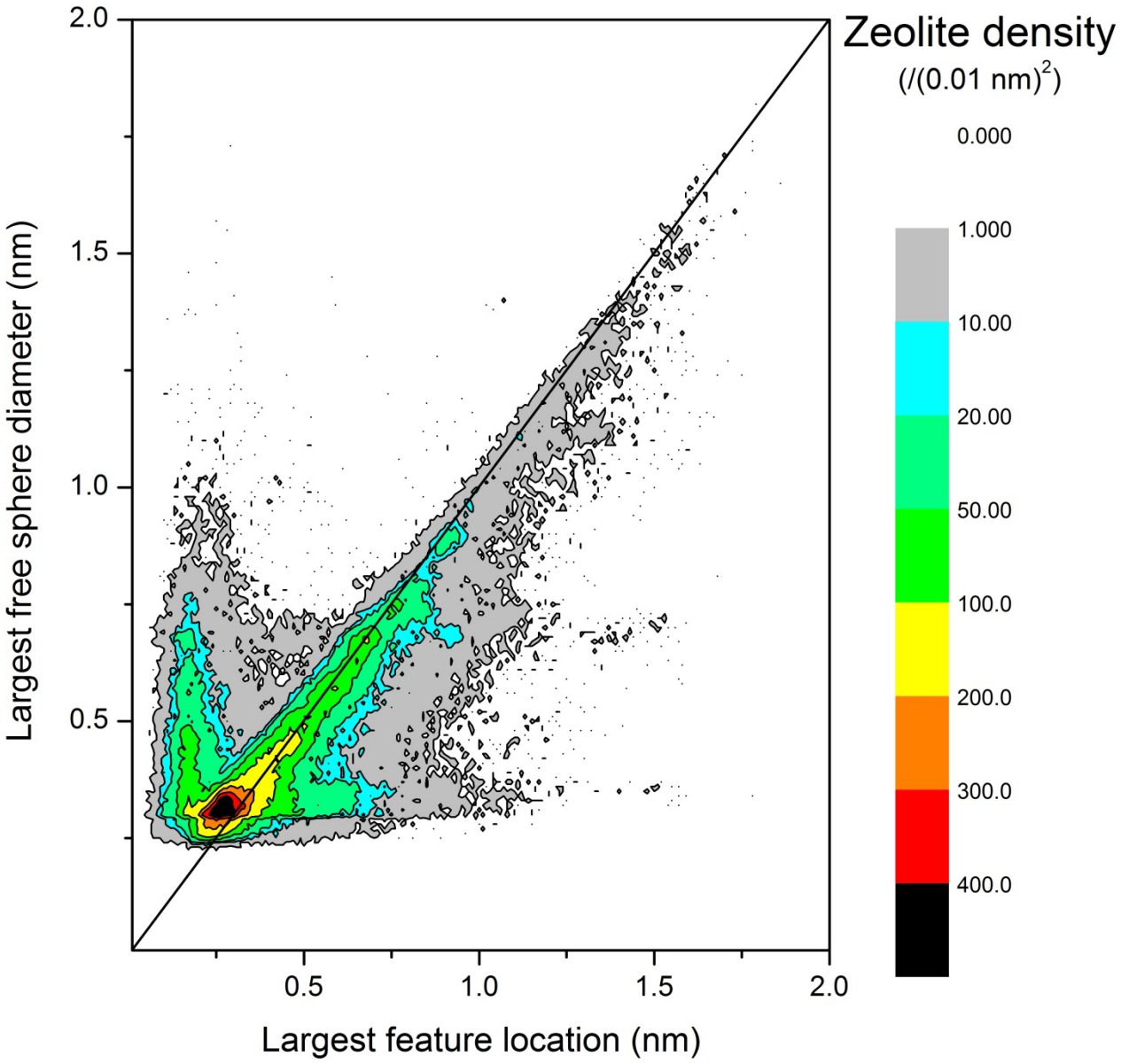

Fig. 3c. Density contour plot comparing zeolite descriptors for ~140,000 zeolites in the Hypothetical Zeolite Database. Largest free sphere diameters and the largest feature in ray trace histograms are calculated using the *constrained* approach with Zeo++ using equivalent probe and van der Waals parameters. Solid parity line is drawn to guide the eye.

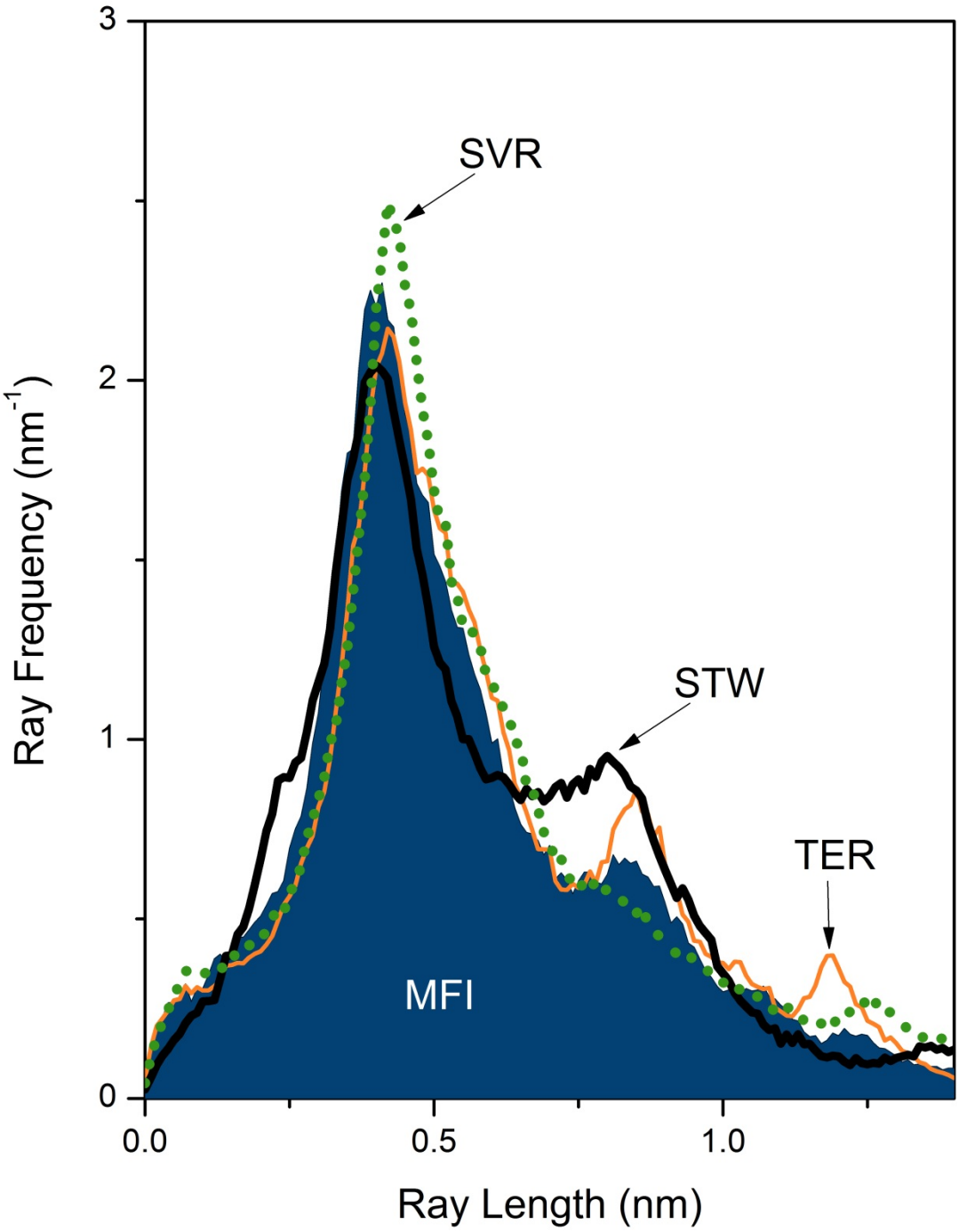

Fig. 4. Ray histograms of MFI (solid blue) and IZA zeolites with minimum Euclidean distances from MFI calculated for rays with lengths between 0-5 nm: TER (thin orange line), STW (thick black line), and SVR (green dotted line).

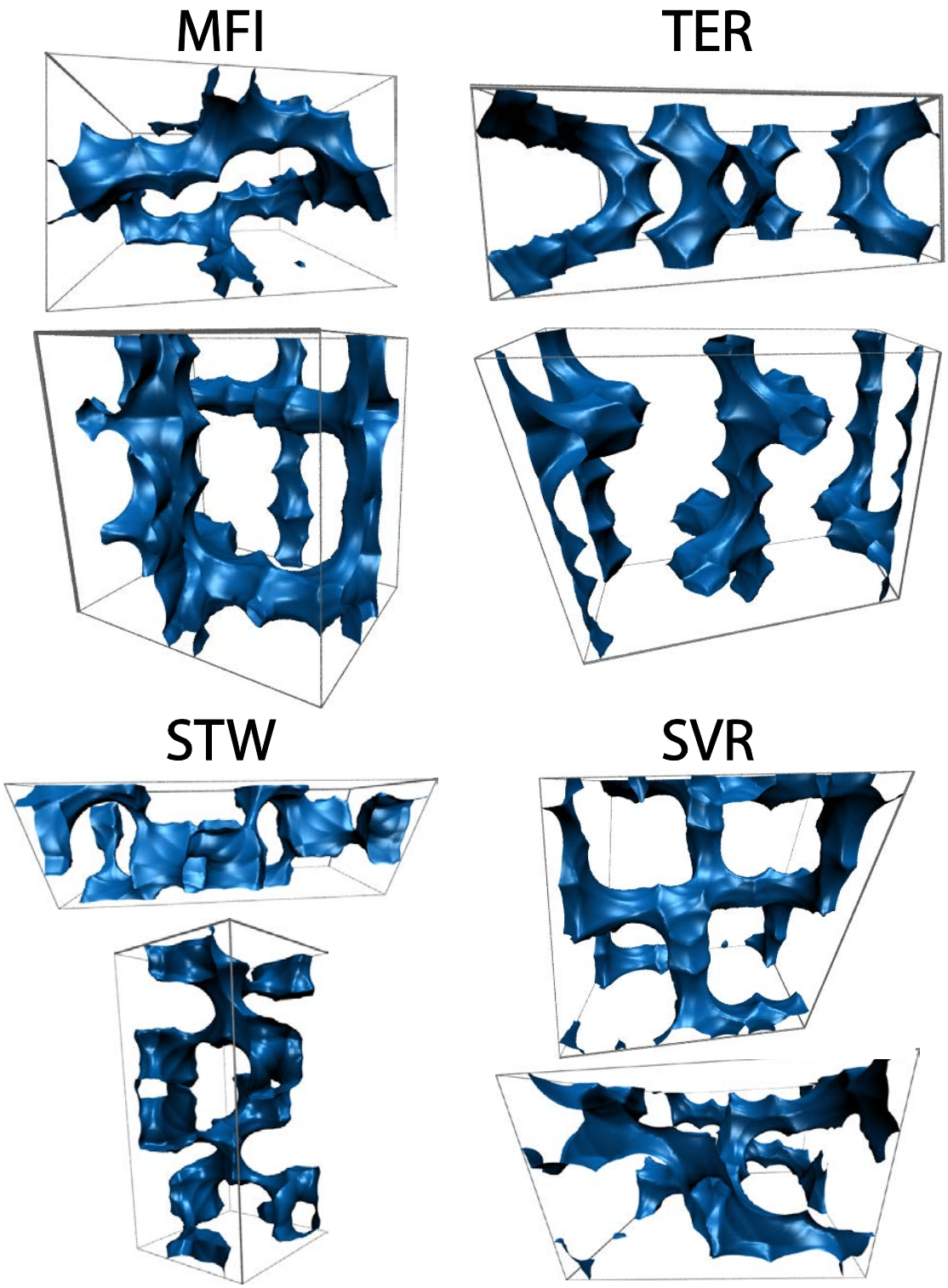

Fig. 5. Pore landscapes for MFI, TER, STW and SVR zeolites determined from the surface area accessible to the center of a spherical probe with a 0.1 nm diameter and O and Si van der Waals radii of 0.152 nm and 0.210 nm, respectively.

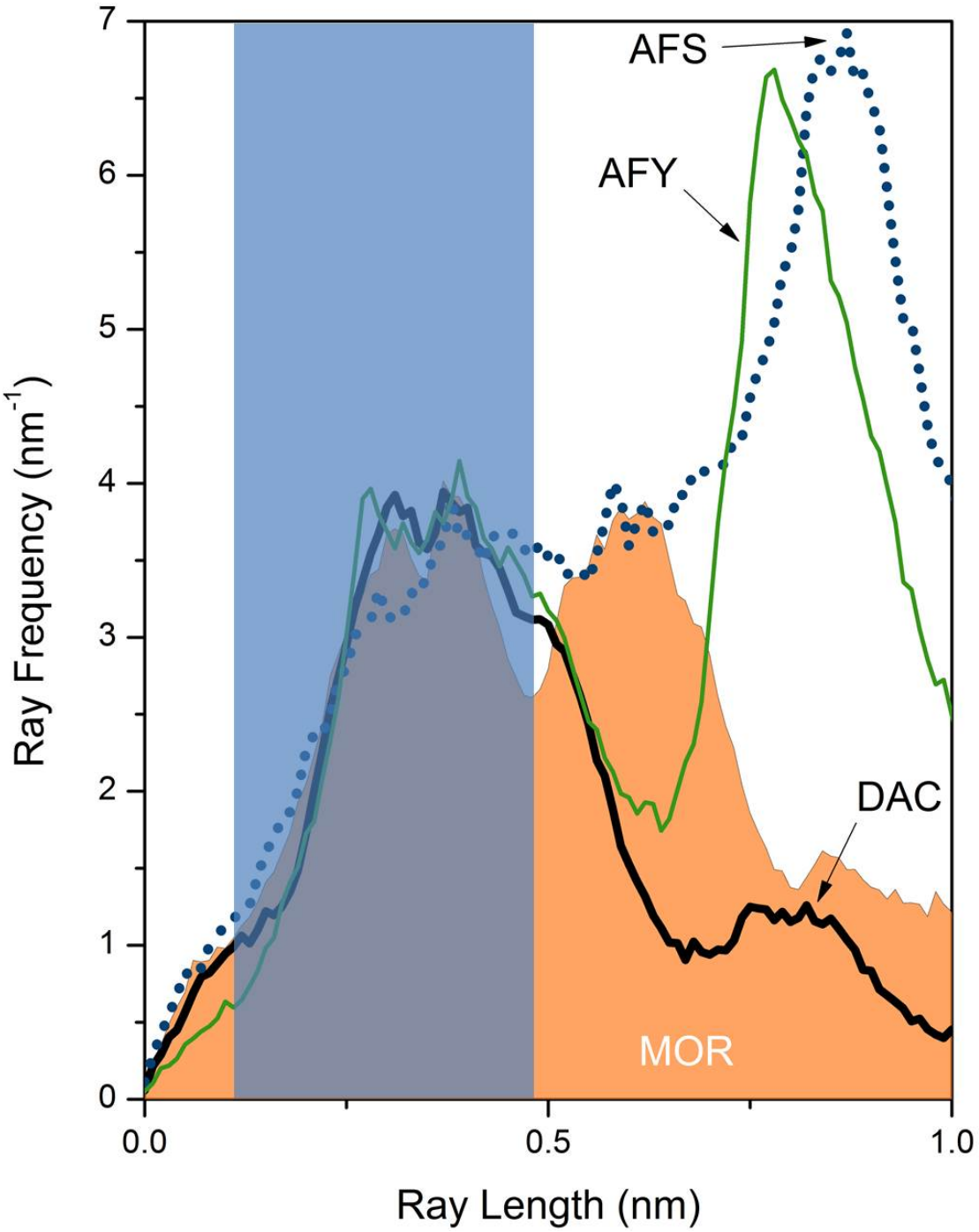

Fig. 6. Ray histograms of MOR (solid orange) and IZA zeolites with minimum Euclidean distances from MOR calculated for rays with lengths between 0.12-0.46 nm (area highlighted by blue box), which are contained mostly in the 8-MR side pockets in MOR: DAC (thick black line), AFS (blue dotted line).and AFY (thin green line). Ray histograms are normalized to compare the feature at 0.12-0.46 nm by dividing ray frequencies by the total number of rays in this range for each zeolite.

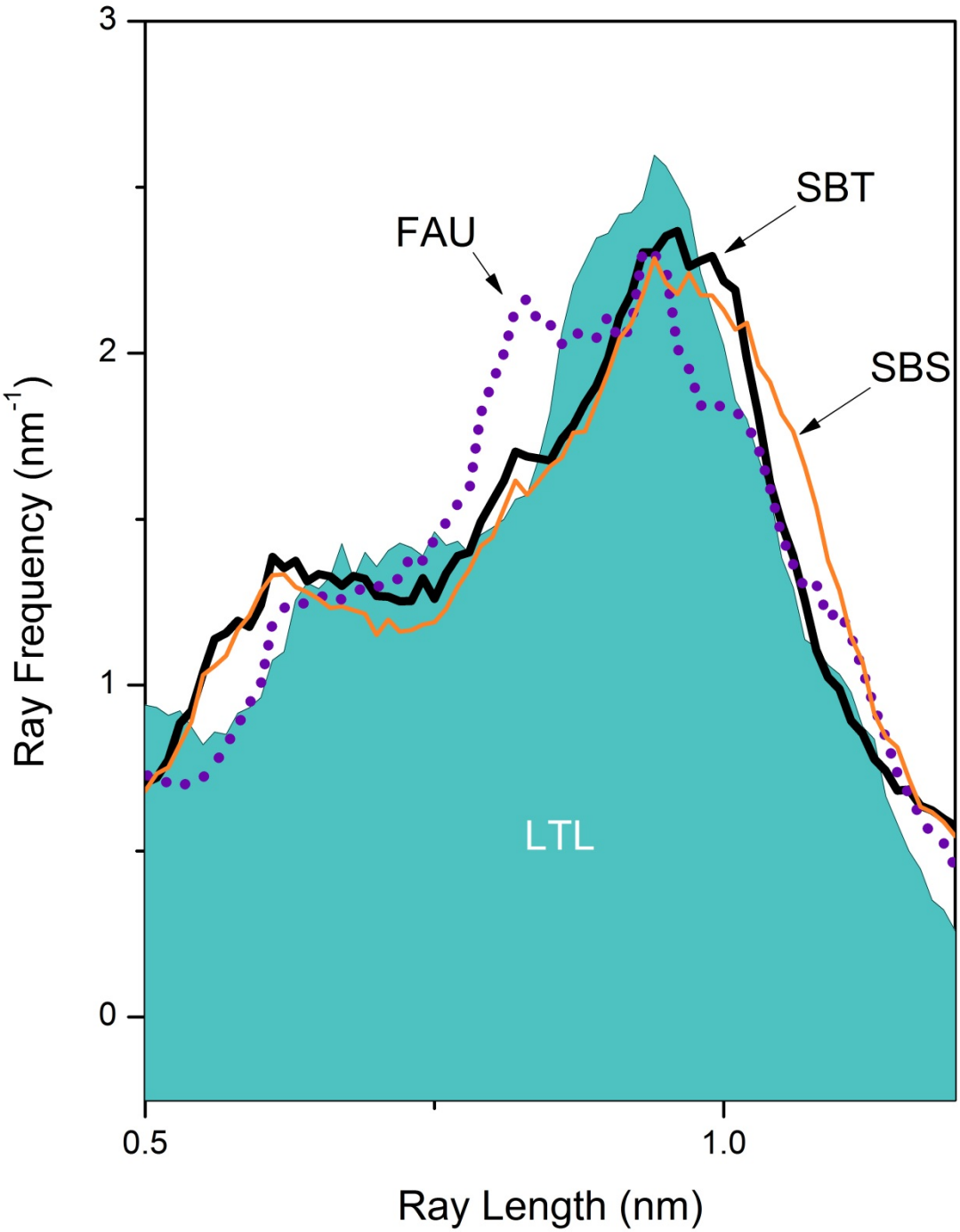

Fig. 7. Ray histograms of LTL (solid blue) and IZA zeolites with minimum Euclidean distances from LTL calculated for rays with lengths between 0.5-1.2 nm, which are contained in the 12-MR channels of LTL: SBT (thick black line), FAU (purple dotted line).and SBS (thin orange line). Ray histograms are normalized to compare the feature at 0.5-1.2 nm by dividing ray frequencies by the total number of rays in this range for each zeolite.

References

[1] J. Čejka, A. Corma, and S. Zones, Zeolites and Catalysis: Synthesis, Reactions and Applications. John Wiley & Sons, 2010.
[2] T.F. Degnan, J. Catal. 216 (2003) 32-46.
[3] A. Corma, Chem. Rev. 95 (1995) 559-614.
[4] E.G. Derouane, P. Dejaifve, and J.B. Nagy, J. Mol. Catal. 3 (1978) 453-457.
[5] E.G. Derouane, J. Catal. 100 (1986) 541-544.
[6] R.T. Carr, M. Neurock, and E. Iglesia, J. Catal. 278 (2011) 78-93.
[7] R. Gounder, A.J. Jones, R.T. Carr, and E. Iglesia, J. Catal. 286 (2012) 214-223.
[8] J. Čejka, G. Centi, J. Perez-Pariente, and W.J. Roth, Catal. Today 179 (2012) 2-15.
[9] C. Baerlocher, and L.B. McCusker. Database of Zeolite Structures.
[10] R. Pophale, P.A. Cheeseman, and M.W. Deem, PCCP 13 (2011) 12407-12412.
[11] R.L. Martin, T.F. Willems, L.C. Lin, J. Kim, J.A. Swisher, B. Smit, and M. Haranczyk, ChemPhysChem 13 (2012) 3595-3597.
[12] M.D. Foster, I. Rivin, M.M.J. Treacy, and O.D. Friedrichs, Micropor. Mesopor. Mater. 90 (2006) 32-38.
[13] E.L. First, C.E. Gounaris, J. Wei, and C.A. Floudas, PCCP 13 (2011) 17339-17358.
[14] R.L. Martin, B. Smit, and M. Haranczyk, J. Chem. Inf. Model. 52 (2012) 308-318.
[15] D.A. Carr, M. Lach-Hab, S.J. Yang, Vaisman, II, and E. Blaisten-Barojas, Micropor. Mesopor. Mater. 117 (2009) 339-349.
[16] N.A. Anurova, V.A. Blatov, G.D. Ilyushin, and D.M. Proserpio, J. Phys. Chem. C 114 (2010) 10160-10170.
[17] M.M. Pinheiro, R. L.; Rycroft, C. H.; Jones, A. J.; Iglesia, E.; Haranczyk, M., J. Mol. Graphics Modell. (2013).
[18] T.F. Willems, C.H. Rycroft, M. Kazi, J.C. Meza, and M. Haranczyk, Micropor. Mesopor. Mater. 149 (2012) 134-141.
[19] M. Haranczyk. Zeo++.
[20] M. Haranczyk, and J.A. Sethian, J. Chem. Theory Comput. 6 (2010) 3472-3480.
[21] E. Haldoupis, S. Nair, and D.S. Sholl, J. Am. Chem. Soc. 132 (2010) 7528-7539.
[22] M.M.J. Treacy, and M.D. Foster, Micropor. Mesopor. Mater. 118 (2009) 106-114.
[23] L. Grajciar, J. Cejka, A. Zukal, C.O. Arean, G.T. Palomino, and P. Nachtigall, ChemSusChem 5 (2012) 2011-2022.
[24] H.V. Bekkum, Introduction to Zeolite Science and Practice. Elsevier, 2001.
[25] E.G. Derouane, Micropor. Mesopor. Mater. 104 (2007) 46-51.
[26] R. Gounder, and E. Iglesia, Acc. Chem. Res. 45 (2012) 229-238.
[27] M. Schenk, B. Smit, T.J.H. Vlugt, and T.L.M. Maesen, Angew. Chem. Int. Ed. 40 (2001) 736-739.
[28] B. Smit, and T.L.M. Maesen, Nature 451 (2008) 671-678.
[29] W.O. Haag, R.M. Lago, and P.B. Weisz, Faraday Discuss. 72 (1981) 317-330.
[30] A. Bhan, A.D. Allian, G.J. Sunley, D.J. Law, and E. Iglesia, J. Am. Chem. Soc. 129 (2007) 4919-4924.
[31] M. Boronat, C. Martinez-Sanchez, D. Law, and A. Corma, J. Am. Chem. Soc. 130 (2008) 16316-16323.
[32] Y. Sugi, H. Maekawa, Y. Hasegawa, H. Naiki, K. Komura, and Y. Kubota, Catal. Today 132 (2008) 27-37.
[33] Y. Sugi, S. Tawada, T. Sugimura, Y. Kubota, T. Hanaoka, T. Matsuzaki, K. Nakajima, and K. Kunimori, Appl. Catal., A 189 (1999) 251-261.
[34] Y. Sugi, and M. Toba, Catal. Today 19 (1994) 187-212.
[35] R.J. Davis, Heterogen. Chem. Rev. 1 (1994) 41-53.
[36] J.T. Miller, N.G.B. Agrawal, G.S. Lane, and F.S. Modica, J. Catal. 163 (1996) 106-116.

[37] J.R.N. Bernard, J. 1976. Method of dehydrocyclizing aliphatic hydrocarbons. Elf-Union, editor, USA.
[38] T.M. Wortel. 1986. Dehydrocyclization of non-aromatic hydrocarbons over zeolite L E.R.E. Co., editor, USA.
[39] T.R.B. Hughes, W.C. 1984. Method of dehydrocyclizing alkanes C.R. Company, editor, USA.
[40] E. Iglesia, and J.E. Baumgartner, in: L. Guczi, F. Solymosi, and P. Tetenyi, (Eds.), Stud. Surf. Sci. Catal., Elsevier, Amsterdam. 993-1006.
[41] R.E. Jentoft, M. Tsapatsis, M.E. Davis, and B.C. Gates, J. Catal. 179 (1998) 565-580.
[42] P. Meriaudeau, and C. Naccache, Cat. Rev. - Sci. Eng. 39 (1997) 5-48.